

**Seismic Emissions  
from  
Solar Flares**

**Diana Ionescu**

Student ID: XXXXXXXXXX

**Doctor of Philosophy**

CSPA, School of Mathematical Sciences  
Monash University

Supervisors:

**Dr. Alina C. Donea & Prof. Paul S. Cally**

June 2010

Diana Ionescu started publishing as Diana Beşliu  
and continues to publish now as Diana Beşliu-Ionescu.

# Contents

<b>1</b>	<b>Introduction</b>	<b>1</b>
1.1	Solar Flares . . . . .	1
1.2	Oscillations . . . . .	4
1.3	Sun quakes . . . . .	7
<b>2</b>	<b>Local Helioseismology Techniques</b>	<b>11</b>
2.1	Helioseismic Holography . . . . .	11
2.2	T-D Diagrams . . . . .	14
2.3	Temporal Variations . . . . .	15
2.3.1	Intensity Continuum . . . . .	16
2.3.2	Doppler Velocities . . . . .	16
2.3.3	Magnetic Variations . . . . .	17
2.4	Spectral Hardness . . . . .	19
<b>3</b>	<b>Data</b>	<b>21</b>
3.1	Sun Quakes . . . . .	21
3.2	WEB Database . . . . .	62
3.3	Conclusions . . . . .	63
<b>4</b>	<b>Multiwavelength Analysis</b>	<b>67</b>
4.1	Intensity Continuum . . . . .	68
4.2	Doppler Data . . . . .	79
4.2.1	Temporal Profiles . . . . .	81
4.2.2	Seismic Ripples . . . . .	86
4.3	Magnetic Transients . . . . .	91
4.4	UV . . . . .	97
4.5	H $\alpha$ . . . . .	101
4.6	EUV . . . . .	107

4.7	Conclusions . . . . .	112
<b>5</b>	<b>Spectral Hardness</b>	<b>119</b>
5.1	Spectra Comparisons . . . . .	129
5.2	Conclusions . . . . .	132
<b>6</b>	<b>RADYN: Clues for Sun Quakes</b>	<b>135</b>
6.1	Numerical Method . . . . .	137
6.1.1	Boundary and Initial Conditions . . . . .	139
6.1.2	Non-thermal Electron Population Beams . . . . .	141
6.2	Results . . . . .	141
6.2.1	Mechanical energy flux . . . . .	143
6.2.2	Temperature Profiles . . . . .	149
6.2.3	Intensity Continuum Differences . . . . .	149
6.3	Discussion and Conclusions . . . . .	152
<b>7</b>	<b>Discussion &amp; Conclusions</b>	<b>155</b>
	<b>Bibliography</b>	<b>161</b>

# Summary

The Sun is the centre and the master of our solar system. Its power gives us light and warmth and life, but its moods can be fearsome. Sunspots, solar flares, coronal mass ejections (CME) and the plethora of other complex magnetic activities that follow the 11-year rhythm of the solar cycle can mean devastation for our technologies, from satellites, to power grids, to telecommunications. Pity the unfortunate astronaut caught unprotected in space during a solar storm!

Flares are the most powerful and most dangerous events on the Sun, spewing huge quantities of radiation and particles into space, often accompanied by a CME, sometimes to pummel the Earth. Only our magnetic shield, the magnetosphere, protects us. All means must be brought to bear when studying the Sun's activity, including observations in many wavelengths from terrestrial and space-borne observatories, and the relatively new science of local helioseismology for peering beneath the surface, the photosphere. Especially during the last decade, that of Solar Cycle 23, advances in theory and technology have opened the Sun's magnetic active regions to our deeper seismic gaze.

Cycle 23 was closely mapped by the Solar and Heliospheric Observatory (*SOHO*) orbiting between the Earth and the Sun. A fascinating discovery made with *SOHO* is that flares high in the Sun's corona not only project their power outwards into space, but also downwards to the photosphere, where they can cause powerful sun quakes. This thesis is devoted to sun quakes: their discovery, their characteristics, and their physics. How and why are they formed, and why do many flares not excite them? How much energy is required to produce them? And how can this unique resource of a sudden localized seismic source be used to better probe the Sun's interior? In so-doing, I present the most detailed survey yet of sun quakes and their physics.

Specifically, we have used the local helioseismic technique known as helioseismic holography to detect sun quakes by imaging their acoustic sources, rather than their harder-to-see expanding ripples. Nearly all known sun quakes, more than a dozen, have been discovered by us in this way. This is sufficient to begin a survey to discover which types of flares excite quakes and which do not. Using a wide range of observations over several wavelengths, we explore the effects of such features as flare area, energy, height, and spectral hardness.

We have also applied a 1D radiation hydrodynamics simulation code RADYN to synthesizing the mechanisms which might create quakes. Both our survey and our simulations favour “back-warming”, whereby the low chromosphere is suddenly heated by the flare. This energy is then quickly transferred to the adjacent photosphere producing a quake.

Because seismic emission from solar flares presents by far the most localized seismic sources in the solar environment, both spatially and temporally, and flares being the only seismic generators whose operation is open to direct view, this phenomenon offers an especially opportune control facility for 21st-century helioseismology.

# Statement

The thesis, except with the committees approval, contains no material which has been accepted for the award of any other degree or diploma in any university or other institution and affirms that to the best of the candidates knowledge the thesis contains no material previously published or written by another person, except where due reference is made in the text of the thesis.

## Notice 1

Under the Copyright Act 1968, this thesis must be used only under the normal conditions of scholarly fair dealing. In particular no results or conclusions should be extracted from it, nor should it be copied or closely paraphrased in whole or in part without the written consent of the author. Proper written acknowledgement should be made for any assistance obtained from this thesis.

## Notice 2

I certify that I have made all reasonable efforts to secure copyright permissions for third-party content included in this thesis and have not knowingly added copyright content to my work without the owner's permission.

# Acknowledgments

I would like to thank Dr. **Alina Donea** for her unlimited and unconditioned (scientific, moral, financial, etc.) support especially during my many difficult times; for her belief that I can rise up to meet Monash standards and expectations; for her faith in my research abilities.

I would like to thank Prof. **Paul Cally** who managed bear my never-ending line of questions, for exceptional scientific (solar, physics, latex, simulations, and the list can go on and on...) and moral support when things seemed unbearable; for reminding me that there are things worse than... doing a PhD and having a baby at the same time.

Dr. **Charles Lindsey** for helping me understand so many aspects and physical interpretations of various phenomena related to my research, and also for being so patient when asking for more scripts and, perhaps most importantly, providing most of the required software. Prof. **Mats Carlsson** for his patience and understanding with regards to my first simulations, and for replying to so many emails and questions.

I would also like to thank the two examiners, Dr. **Doug Braun** and Prof. **Ian Craig**, whose comments and suggestions improved the final manuscript.

I would like to thank my family, who have supported me in every imaginable way. My parents, for their belief that I can do anything; for their continuous encouragement to always do better; for their substantial financial support; and for making me the person I am today. My husband, for being supportive and understanding in my pursuit of my dreams. My parents-in-law for their unlimited help with housing and baby-sitting. And most importantly: **my daughter** (“yet another PhD baby”) for her smiles, and for putting life into perspective for me.

My dear friends Dr. Hamed Moradi, Dr. Juan Carlos Martinez-Oliveros for endless hours of lingering ... The Clique, for making Monash an incredible place to be. Ms. Houri Jahanshahrad for being a true friend through emotional times, Ms. Marie Newington for being the best office mate.

The “fourth floor ladies” (Sonia Francis, Doris Herft, Linda Mayer, Gertrude Nayak, Melissa Swindle, Amanda Teo.) who were extremely helpful with various forms, teaching me a lot of stuff about the administrative work behind the research, and for their friendship.

Mrs. Georgeta Mariş for the time she spent on endless emails to keep me comfort as my “adoptive mum”; for the enormous amount of time spent reading and replying to my complaints about everything; for her support during the difficult times while returning to the Astronomical Institute; and for the extraordinary “zacusca” and “dulceața”.

My gratitude also extends to the Romanian community in Australia, giving me a feeling of “little Romania” each Sunday Especially Dr. Floreana Coman and Pr. Dumitru Coman who thought of me as a daughter and made me feel very welcome every time. Mrs. Emilia Gavrilescu for her prayers and Romanian food, for which she never truly knew how much they were appreciated Mrs. Silvia Alexandrescu for interesting trips to shopping malls and her kindness.

My thanks should also to: Dr. Marilena Mierla for unlimited IDL support; Mr. Adrian Catu for unlimited linux-related problems support; Dr. Razvan Roescu for unlimited answers related to latex problems; and Mr. Jon Holdsworth for an exceptionally good IT-related support at Monash.

And finally, Dr. Gillian Singleton for taking care of my physical and mental health throughout the PhD.

# Chapter 1

## Introduction

With the advent of the Michelson Doppler Imager (*MDI*) on board the Solar & Heliospheric Observatory (*SOHO*) satellite, helioseismology has proven to be one of the most exact sciences, where theory and observations agree very well, and an exceptional tool for precisely studying the Sun's interior. A major discovery, reported by [Kosovichev and Zharkova \(1998\)](#), was the detection of solar quakes. This discovery produced a sensation at the time. What were the possible seismic sources triggering such powerful events? However, further quakes were not observed until 2004, when two other powerful seismic events were detected by [Donea and Lindsey \(2005\)](#). This work reopened the field of the seismology of flares, which is also the topic of my thesis. In 2005 I was introduced to this new field and since then have had the great opportunity to make my contribution to it, by participating in a survey of the solar flares detected thus far by *MDI-SOHO*. Ever since then I have been simply hooked to it. This thesis will describe my contribution to the knowledge about sun quakes.

Chapter 1 presents a short introduction to solar flares, basic concepts about solar oscillations and the discovery of sun quakes.

### 1.1 Solar Flares

Solar flares are the most energetic phenomenon produced by the Sun. According to the Oxford English Dictionary a solar flare is defined as: “a brief eruption of intense high-energy radiation from the Sun's surface.” It is, also, one of the most puzzling solar phenomena and is still not fully

comprehended.

Before presenting the latest status of understanding of the physics of the seismology of flares, we will make a short historic digression on the detection of solar flares and some of their relevant properties.

The first solar flare to be observed was in 1859 as a localized brightening in a sunspot group by two independent observers, Carrington (1859) and Hodgson (1859). It was a white light event, the only visible by eye event at the time, considering the current stage of technology. The September 1, 1859 solar flare was followed by a magnetic storm at the Earth, characterised by fires, started because telegraph wires shorted out in the USA and Europe, and extraordinary auroras around the globe, visible even in the Carribean! The time delay between the solar flare detection and the consequences registered on Earth, as stated by Carrington in his paper (Carrington, 1859), was 17 hours and 40 minutes. Although Carrington carefully noted this relationship between solar flares and terrestrial consequences, he was cautious in his appraisal: “and that towards four hours after midnight there commenced a great magnetic storm, which subsequent accounts established to have been as considerable in the southern as in the northern hemisphere”. That was the first time that scientists glimpsed the relation between solar flares and geomagnetic storms.

In 1936 flares began to be studied in the emission line of  $H\alpha$ . These observations improved our knowledge about solar flares and they are intensively used today for comparisons against other satellite observations or for testing various measurements. Starting 1962, the Sun began to be studied in ultraviolet and soft X-ray radiation from outer space with the “Orbiting Solar Observatory” (*OSO*) launched by NASA (Bonnet, 1975).

Since 1975 (with the launch of the first Geostationary Operational Environmental Satellite *GOES-1* owned and operated by the National Oceanic and Atmospheric Administration (NOAA)) flares are continuously monitored in soft X-ray emission. The end of the last century brought an explosion of solar missions with various instruments, such as *Helios*, *Ulysses*, *Soho*, *ACE* and *STEREO*, that have greatly improved our knowledge and understanding of solar flares and continue to provide us with astonishing data.

Flares occur when the magnetic energy that has built up in the solar atmosphere is suddenly released. Radiation is emitted across virtually the entire electro-magnetic spectrum, from radio waves at the long wavelength end, through optical emission to X-rays and gamma rays at the short wavelength end. The flare energy is carried away by flows of plasma too, such as

Coronal Mass Ejections (CME) and by non-thermal particles.

There are two widely used classification systems that address flare “size” or “importance”. Historically, the first of these is the H classification scheme that was developed during the 1930s. It consists of a character (S = subflare, or 1, 2, 3 and 4 for successively larger flares) that denotes the flare size, and a letter (f = faint, n = normal, b = bright) corresponding to a subjective estimate of the emission intensity. Thus, the most outstanding flares are classified as 4b and the smallest and faintest as Sf.

A second classification, that has come into common usage since about 1970, is based on soft X-ray observations of the Sun, the integrated flux in the 1–8 Å band (I) by Earth-orbiting satellites. The size of the flare is given by the peak intensity (on a logarithmic scale) of the emission. Flares are classified with a letter (A, B, C, M or X-class) and a number (1–9) that acts as a multiplier. The weakest class is A. An A-class solar flare has a characteristic  $I < 10^{-7}$  W/m<sup>2</sup> ( $10^{-4}$  erg/cm<sup>2</sup>/s); B-class solar flares has  $10^{-7} \leq I < 10^{-6}$  W/m<sup>2</sup>; for a C-class I  $10^{-6} \leq I < 10^{-5}$  W/m<sup>2</sup>; for an M-class I  $10^{-5} \leq I < 10^{-4}$  W/m<sup>2</sup> and X-class solar flares are all the flares characterised by a flux of  $I \geq 10^{-4}$  W/m<sup>2</sup> ( $10^{-1}$  erg/cm<sup>2</sup>/s). X-class flares are major events that can trigger planet-wide radio blackouts and long-lasting radiation storms. M-class flares are medium-sized; they can cause brief radio blackouts that affect Earth’s polar regions. Minor radiation storms sometimes follow an M-class flare. Compared to X- and M-class events, C, B and A-class flares are small with few noticeable, if any, consequences here on Earth.

Solar flares vary profoundly with respect to the solar cycle. The solar cycle represents the quasi-periodic waxing and waning of the Sun’s activity and is measured by the sunspot number. In 1919, G. E. Hale noted that the magnetic polarity of the preceding and the following spots of the bipolar regions reverse from one 11-year cycle to the next, in each solar hemisphere. Moreover, the Sun’s magnetic polarity reverses around sunspot maximum (Babcock and Babcock, 1955). This magnetic cycle, composed of two (oppositely polarized) 11-year part, represents, in fact, the Sun’s Hale cycle (HC). When the solar cycle is at its maximum, it produces as many as several X and M-type flares per day, as opposed to the minimum of activity, when there can be months with no flaring activity.

The Sun has now finished its cycle numbered 23, in 2007, and we are at the beginning of Solar Cycle 24 (SC24). We have a very good coverage of solar flares provided by *SOHO-MDI* during 1996 to 2005, including the

maximum of SC23, but excluding the ascending phase.

SC23 was the object of very detailed studies related to global and local solar oscillations. SC23 was, therefore, very distinct from all other cycles because of the many new discoveries, one of which, the solar quakes is the object of my studies. Sun quakes turned out to be one of the most exciting new tools for solar interior insights through information refracted waves carry to the surface.

In the next section I will describe the main properties of the oscillations in the sun, starting first with global oscillations and then moving to smaller areas where local helioseismology can tell us more about the impact of flares on the solar surface.

## 1.2 Oscillations

As stated by [Christensen-Dalsgaard \(2002\)](#), it is possible that the first indications of solar oscillations were detected by [Plaskett \(1916\)](#), who observed fluctuations in the solar surface Doppler velocity in measurements of the solar rotation rate. At that time it did not seem clear whether the fluctuations were truly solar or just induced by some effects in the Earth's atmosphere. [Hart \(1954, 1956\)](#) established the origin of these fluctuations to be caused by the Sun.

Precise observations of oscillations of the solar surface were made by [Leighton et al. \(1962\)](#). They detected periodic oscillations in the local Doppler velocities with periods of around 300 seconds and a lifetime of at most a few periods. A confirmation of the initial detection of the oscillations was made by [Evans and Michard \(1962\)](#).

The next major observational step was the identification by [Claverie et al. \(1979\)](#) of modal structure of five-minute oscillations in Doppler-velocity observations in light integrated over the solar disk. These were the first confirmed detections of truly global modes of oscillations. By providing a full range of modes the observations opened the possibilities for detailed inferences of properties of the solar interior.

Later, [Claverie et al. \(1979\)](#) identified lower wavenumber oscillations with the same period providing conclusive evidence of global modes of oscillation within the Sun. With a full range of modes, properties of the solar interior can be inferred by comparing theoretically calculated solar oscillation spectra, observationally obtained power spectra and diagnostic diagrams of pressure

modes.

At present, solar oscillations are detected by the Global Oscillation Network Group (*GONG+* <http://gong.nso.edu/>), *SOHO-MDI* (Scherrer et al., 1995) and *Hinode (Solar-B)* (Kosugi et al., 2007). As I write, the first data is arriving from the Helioseismic Michelson Imager on board the Solar Dynamic Observatory (*HMI-SDO*) with vastly improved signal-to-noise ratio, and promising a near complete coverage of the solar cycle 24. My work is based on using the data provided by *SOHO-MDI*.

Scherrer et al. (1995) states that *MDI* is based on a modification of the Fourier Tachometer technique (Brown, 1980; Evans, 1980). Two tunable Michelson interferometers (Title and Ramsey, 1980) define a 94mÅ band-pass that can be tuned across the Ni I 6768Å solar absorption line. Velocity continuum intensity and other observables are computed on board from combinations of filtergrams. This line is formed near the middle of the photosphere.

The normal modes of oscillation of the Sun can be categorized as either p-modes, f-modes, or g-modes. Each mode is characterized by its spherical harmonic degree, (which is approximately the number of wavelengths around the solar circumference), and the radial order,  $n$  (the number of nodes in the radial direction). The g- (or “gravity”) modes are internal gravity waves for which the primary restoring force is buoyancy, and are almost totally confined to the deep solar interior. The f- (or “fundamental”) mode ( $n = 0$ ) is an incompressible, surface gravity wave with amplitude that decays roughly exponentially with depth away from the solar surface. The dispersion relation is similar to that for deep water waves,  $\omega^2 = gkh$ , where  $\omega$  is the angular temporal frequency of the wave,  $g = 274 \text{ m s}^{-2}$  is the gravitational acceleration at the Sun’s surface,  $k_h = \sqrt{l(l+1)}/R_\odot$  is the horizontal wave-number and  $R_\odot = 696 \text{ Mm}$  is the solar radius. The p- (or “pressure”) modes are gravity-modified acoustic waves, with the pressure being the primary restoring force.

The discrete mode pattern is a consequence of the existence of a resonant cavity with reflecting boundaries. As illustrated in Figure 1.1, the photosphere essentially acts like a mirror, with the change in physical parameters providing such an abrupt change in conditions that it represents a fixed node for oscillations, at least below the photospheric acoustic cutoff frequency of around 5.2 mHz.

The global modes do not distinguish between the Northern and Southern hemispheres. Unless one considers the perturbations to the eigenfunctions

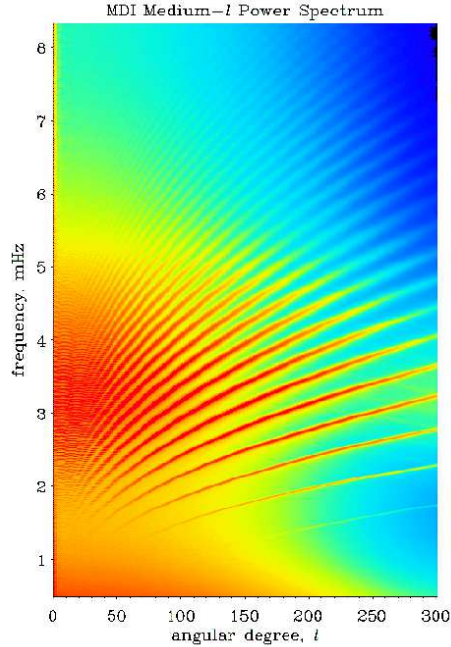


Figure 1.1: The  $\ell - \nu$  (frequency versus angular degree) diagram obtained by the Michelson Doppler Imager (*MDI*). Image from the [soi.stanford.edu](http://soi.stanford.edu) website.

themselves, the detailed spatial distribution of a parameter cannot be better determined. As a result, it is not possible to detect longitudinal variations or flows in meridional planes and other fine structures using global-mode helioseismology.

Local helioseismology was developed to complement global helioseismology with the goal to interpret the full wave field observed at the surface, not just the eigen frequencies.

In the 1980's local helioseismology began to be an important tool for studying the Sun. In 1981 the filter property of the sunspot was discovered ([Zhugzhda and Locans, 1981](#)): sunspot atmospheres work as multichannel filters for waves. Six years later [Bogdan \(1987\)](#) discovered the sunspot was also a scatterer of acoustic waves. In 1987, [Braun et al. \(1987\)](#), using Hankel analysis, proved that sunspots absorb as much as 50% of the incoming acoustic waves. Hankel Analysis was the first method of the local techniques. Later, [Braun et al. \(1992\)](#) and subsequent papers, using Fourier-Hankel de-

composition, further studied the properties of scattering and absorption.

Using phase-sensitive holography [Lindsey and Braun \(2005a,b\)](#) discovered the showerglass effect, a direct dependence of control-correlation phase signatures on the line-of-sight angle in the plane defined by the vertical and magnetic field vectors. [Schunker et al. \(2005\)](#) demonstrated that there is a clear cyclic variation of the ingress phase with azimuthal angle within a sunspot penumbra, and the line-of-sight direction. The magnetic field of the sunspots affects the acoustic waves passing through.

A frequency dependency of waves in sunspots is supported by the theory of [Schunker and Cally \(2006\)](#). [Schunker et al. \(2007\)](#) describe how a wave of lower frequency will experience the upper turning point at a lower depth than a higher frequency wave. In regions of stronger field strengths, corresponding to the inner penumbrae, acoustic waves at 5 mHz are affected more by the magnetic field as seen in the observations presented here.

Another influence on acoustic waves is the presence of strong magnetic field in active regions. [Schunker et al. \(2008\)](#) say that the inclined magnetic field in sunspot penumbrae may convert primarily vertically-propagating acoustic waves into elliptical motion.

The subsequent years were marked by the development of special techniques such as: ring-diagrams, antipodal imaging and helioseismic holography, time-distance helioseismology and the holography formalism.

## 1.3 Sun quakes

The path to understand solar flares and their effects upon the terrestrial atmosphere was, and still is, complicated.

As briefly mentioned in Section 1.1, one of the most exciting new discoveries related to solar oscillations and effects of solar flares are sun quakes.

Early indications of possible stimulation of “high-order modes of solar oscillation to interesting amplitudes” were suggested by [Wolff \(1972\)](#). [Haber et al. \(1988a\)](#) considered possible excitation of acoustic modes within the Sun, but found that power bridges may be influenced. by the poor data quality of the time.

The first attempt at computing radial propagating waves using Doppler velocities interpolated onto a cylindrical coordinate system. ([Haber et al., 1988b](#)) and suggested that the flare may have excited outgoing waves.

[Braun and Duvall \(1990\)](#) presented their results as “unable to detect an

excess of oscillatory power in the vicinity of the active region following a large flare”, but did not rule out the existence of sun quakes.

The first known sun quake was discovered by [Kosovichev and Zharkova \(1998\)](#) in helioseismic observations from the *MDI* on the Solar and Heliospheric Observatory (*SOHO*) spacecraft. The term “sun quake” characterised a roughly circular surface ripple seen accelerating outwards from the site of an impulsive flare 20–60 minutes after the impulsive phase. [Kosovichev and Zharkova \(1998\)](#) recognized this in *MDI* Doppler map movies of NOAA AR7978 following the X2-class flare of July 9, 1996.

According to [Beşliu et al. \(2005a\)](#), identifying surface ripples from flares is very difficult. The 5-minute oscillations will swamp most of the sun quake ripples. [Donea et al. \(1999\)](#) subsequently applied computational seismic holography to the *MDI* observations and the photospheric acoustic source directly rather than the expanding ripples which result from it. The resulting “egression power maps” ([Lindsey and Braun, 2000](#)) showed a relatively compact seismic source centred on a delta-configuration sunspot in the middle of the active region, where [Kosovichev and Zharkova \(1998\)](#) had noted a local transient disturbance in the *MDI* Doppler maps at the onset of the flare. The seismic source approximately covered the two oppositely polarized umbrae that formed the heart of the sunspot, roughly extending 15 Mm in the east-west direction and 18 Mm in the north-south direction.

The next sun quake discovery was made by [Donea and Lindsey \(2005\)](#) when they imaged the seismic emission generated by X17.2 and X10.0 class solar flares above AR 10486 in October 28 and 29, 2003, respectively.

Follow-up examinations of a selection of other large flares showed no sign of seismic emission, establishing that most flares are acoustically inactive. These included the X5.0-class “Bastille Day” flare of July 14, 2000 and the three X-class flares of November 24, 2000. However, [Donea and Lindsey \(2004\)](#); [Donea et al. \(2004\)](#); [Donea and Lindsey \(2005\)](#) measured strong seismic signatures in *MDI* observations of the X17.0-class flare of October 28, 2003 and the X10.0-class flare of October 29, 2003. Seismic holography applied to helioseismic observations by *SOHO-MDI* showed seismic emission from both, including two widely separated compact signatures in the case of the October 28 flare ([Donea and Lindsey, 2005](#)).

Images from the Reuven Ramaty High Energy Solar Spectroscopic Imager (*RHESSI*) and the Transition Region and Coronal Explorer (*TRACE*), showed that the footpoints of coronal loops connect the two sites of conspicuous seismic emission.

These results suggested acoustic emission driven by explosive heating and evaporation of the chromosphere by high-energy particles travelling down coronal magnetic field lines. Therefore, the acoustically active flares are the most compact, most impulsive, and highest-frequency solar acoustic sources discovered to date. Moreover, they are the only known sources of acoustic waves that operate in plain view in the outer solar atmosphere. This makes the transients they release into an active region subphotosphere understandable in a way that wave generation by subphotospheric convection cannot be.

Since 2005 we have detected more than a dozen sun quakes generated by X-type solar flares and several generated by M-type (as weak as M6.7) solar flares (Martinez-Oliveros et al., 2008b). The purpose of our survey was to improve the statistical database on acoustic emission from flares and our understanding of the variety of dynamical factors that can determine the significance of flare emission into the solar interior. From our survey work we conclude that, there has been little correlation between the *GOES* X-ray energy of the flare and the energy of the seismic transient. While the proportion of M-class flares that are acoustically active is substantially smaller than of X-class flares, the increasing number of weaker flares suggests that a continuation of the survey will further improve our understanding of the physics of acoustic flares.

Since the *MDI* database covers only a fraction of the flares that occurred during SC23, it would appear that the Helioseismic Magnetic Imager (*HMI*), launched in 2010 on the Solar Dynamics Observatory (*SDO*), will observe scores of sun quakes over the full term of SC24. This expectation opens major new prospects for *HMI*, not only for understanding the dynamics of flares but for addressing important outstanding questions that bear on the use of helioseismic observations to probe the subphotosphere of active regions.

All the above work has motivated me to study the properties of solar flares that generate seismic transients. I have studied not only the seismic event at the photospheric surface, but I also looked at the responses throughout the entire solar atmosphere to the acoustic flare. In the next chapters I will present this response of the atmosphere to these types of flares starting with the photospheric level, through analysing wavelength emissions such as intensity continuum, Doppler LOS velocities, magnetic transients,  $H\alpha$ , UV, EUV.

I will also present a detailed analysis of the comprehensive survey we have performed in 2005 and extended during my PhD studies in Chapter 3.

I will show that intensity continuum and  $H\alpha$  flare signature spatially and temporally correlate with the egression signal, as well as with other excess emissions (such as UV, EUV, Doppler and magnetic signatures) in Chapter 4.

Chapter 5 presents results related to spectral hardness, from acoustic and intensity continuum emissions.

Chapter 6 will present results from simulations of solar flares and comparisons to our observational results.

Chapter 7 will conclude all of our observations and theoretical interpretations.

# Chapter 2

## Local Helioseismology Techniques Used to Analyse Seismic Transients from Flares

This chapter will present the techniques used to analyse the seismic transients and their associated emissions. I will begin with an overview of computational helioseismic holography, continue with a short presentation of so called “time-distance” representation of wave front movement in time and finish with our two other techniques of spectral analysis and magnetic field temporal profile.

This will provide the necessary background for understanding the techniques we use and the means to compare them with other known data analysing tools. This chapter also contains the detailed presentation of all other techniques used to analyse data in this work.

### 2.1 Helioseismic Holography

For imaging acoustic sources generated by solar flares we have used a technique named computational helioseismic holography. This technique is used to image acoustic sources. It reconstructs phase-coherent acoustic waves observed at the solar surface into the solar interior to render stigmatic images of subsurface sources that have given rise to the surface disturbance. Because the solar interior refracts down-going waves back to the surface, helioseismic holography can use observations in one surface region, to image another

surface region. For this purpose holography uses a pupil defined as an annulus with radius 15–45 Mm, to image the focus a considerable distance away from the pupil.

The idea was first introduced by [Roddier \(1975\)](#) as a principle of generating an acoustic hologram of the solar surface. The method presented by Lallemand is based on registering on a photographic plate the complex amplitudes of the photospheric oscillations in each point of the Sun, such as in coherent light the hologram could visualize the subjacent sources ([Roddier, 1975](#)).

The main computations in holography are of the “ingression” and “egression”. These two quantities are estimates of the wave-field in the solar interior; the ingression is an assessment of the observed wave-field converging upon the focal point while the egression is an assessment of waves diverging from that point. The ingression,  $H_-$ , and the egression,  $H_+$ , are obtained from the wave-field at the surface,  $\psi$ , through theoretical Green’s functions.

When the surface acoustic field at any point  $\mathbf{r}'$  in the pupil is expressed as a complex amplitude  $\hat{\psi}$  (which may for example be a velocity or an intensity) for any given frequency  $\omega$ , the acoustic egression can be expressed as

$$\hat{H}_+(\mathbf{r}, \omega) = \int_{pupil} \hat{G}_+(\mathbf{r}, \mathbf{r}', \omega) \hat{\psi}(\mathbf{r}', \omega) d^2\mathbf{r}'. \quad (2.1)$$

In equation 2.1  $\hat{G}_+(\mathbf{r}, \mathbf{r}', \omega)$  is a Green’s function that expresses the disturbance at the focus,  $\mathbf{r}$ , due to a measured point source at surface point  $\mathbf{r}'$  from which the acoustic wave is supposed to propagate backwards in time to the focus.

The relation between the complex amplitude,  $\hat{\psi}(\mathbf{r}, \omega)$ , of frequency appearing in equation 2.1 and the real acoustic field,  $\psi(\mathbf{r}, t)$ , representing the surface acoustic field in the *MDI* observations as a function of time is expressed by the Fourier transform:

$$\psi(\mathbf{r}, t) = \frac{1}{\sqrt{2\pi}} \int_{-\infty}^{\infty} e^{i\omega t} \hat{\psi}(\mathbf{r}, \omega) d\omega. \quad (2.2)$$

The same applies to the acoustic egression:

$$H_+(\mathbf{r}, t) = \frac{1}{\sqrt{2\pi}} \int_{-\infty}^{\infty} \hat{H}_+(\mathbf{r}, \omega) e^{i\omega t} d\omega. \quad (2.3)$$

The “egression power,”

$$P(\mathbf{r}, t) = |H_+(\mathbf{r}, t)|^2 \quad (2.4)$$

is extensively used in studying/detecting acoustic sources and absorbers. Equation 2.4 is used when calculating the egression power for each pixel in the image. Therefore, we create maps of egression power around active regions with the main aim of detecting seismic sources if flares were acoustically active. This translates into visualizing compact signatures in the spatial and temporal neighbourhoods of localized seismic transient emitters. The signature of a localized absorber illuminated by ambient acoustic noise is a similarly sharp deficit in egression power, appearing as a silhouette against a generally positive background, when rendered graphically.

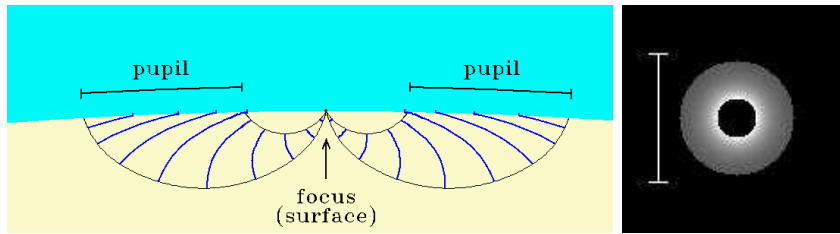


Figure 2.1: Schematic view of the waves refracted to the solar surface that are being analysed in the pupil. On the right, the pupil.

The expanding ripples characteristic of sun quakes are thought to result from the refraction back to the surface of acoustic waves emanating from the compact source generated by the flare at the photosphere. Because the waves producing ripples of greater radii have refracted from deeper in the Sun, where the sound speed is greater, there is a natural acceleration as the ripples propagate outwards. This has been detected by [Kosovichev and Zharkova \(1998\)](#).

The helioseismic holography technique is applied to (*SOHO-MDI*) 1 minute cadence Dopplegrams ([Scherrer et al., 1995](#)). They usually have a resolution of 2 arcsec/px. The high resolution data, produced on some occasions, has an 0.6 arcsec/px resolution. The difference is that the high resolution data has a narrow field of view of 614 arcsecs  $\times$  360/420/450 or 614 arcsecs, centred on the solar disk, the normal resolution data being full disk images. These can be used to produce egression power maps centred at frequencies ranging from 3 to 6.5 mHz with a 2 mHz band.

In my research work presented in this thesis, I have used mainly  $256 \times 256$  pixel Postel projected images of the raw Dopplegrams centred on the flaring AR, in a sequence of, at least two, usually four, consecutive hours of continuous data. These are used to compute egression power maps which are  $256 \times 256$  pixels images showing the egression power at each point in the frame.

We analysed the *MDI* Dopplegrams by constructing egression power maps centred at 6 mHz in order to identify if the seismic transients produced by the flares resonate at this frequency. The 5-minute photospheric oscillations of the Sun makes it difficult to distinguish such a seismic signature for most of the seismic flares we detected. However, for reference, the seismic transient reported by [Donea et al. \(1999\)](#) makes itself present in the egression power maps even at such low frequencies.

## 2.2 Time-Distance Diagrams

[Kosovichev and Zharkova \(1998\)](#) constructed seismograms (maps of distances traveled by the wave front) of the solar flare by remapping the *SOHO-MDI* Doppler images into polar coordinates centred at the point of the initial velocity impulse, and then applying a Fourier transform with respect to the azimuthal angle ([Kosovichev and Zharkova, 1998](#), See Fig. 1d). A seismogram is the record of an earth tremor made by a seismograph, so their idea was to create an analog concept for the solar quake to show the corresponding wave movement in the Sun.

In the case of the July 9, 1996 X2.6 solar flare, the seismic wave was so powerful that it was even seen in simple differences of Dopplergrams as ridges which began about 18 Mm from the flare site and reached about 120 Mm.

This technique is used to show the wave front moving in time. Because of the strong fluctuating motions of the background, the ripple is difficult to see in individual Dopplergrams. Only a few of the reported seismic sources produced visible surface ripples ([Kosovichev and Zharkova, 1998](#); [Kosovichev, 2006](#); [Zharkova and Sekii, 2007](#); [Moradi et al., 2007](#); [Martinez-Oliveros et al., 2007](#)) making the physics of seismic flares even more interesting. This raises important questions: why do only a few of the solar flares display surface ripples? Is the magnetic structure of the active region (photospheric and sub-photospheric) relevant for sound wave propagation? What is the relationship between sun quakes and photospheric mass flows? What is the main cause

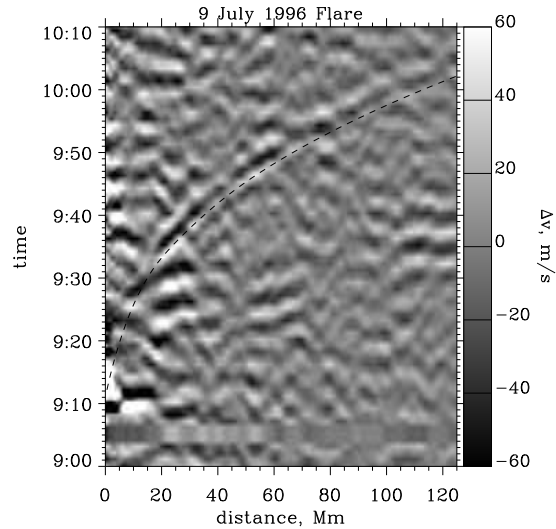


Figure 2.2: Flare seismogram representing the axisymmetrical components of the velocity disturbance. Dashed curve: theoretical time-distance relation for acoustic rays initiated at the flare core at 09:11; the flare signal is a black-and-white ridge around this curve. Other disturbances are solar noise. Figure from [Kosovichev and Zharkova \(1998\)](#) made available by courtesy of Prof. Valentina Zharkova.

of the anisotropy of the wave fronts?

Later, [Kosovichev \(2006\)](#) constructed seismograms of some of the events and reported the anisotropy of the waves. [Martinez-Oliveros et al. \(2007, 2008b\)](#) discovered seismic ridges from an even weaker, M6.7, flare.

## 2.3 Temporal Variations

We have also studied the temporal profiles of the intensity continuum emission, Doppler LOS velocities and magnetic transients associated with sun quakes. Understanding the connection between the evolution of different measures should give us insight and information about the heating processes and the different mechanisms of energy transportation from the corona to the photosphere. All temporal profiles have been computed by integrating the signal within the sun quake area at each moment of observation.

We inspected a two-hour sequence of the data and compared plots of

the mean ( $\langle I_{los} \rangle$ ) and the root-mean-square ( $RMS_I \sim \langle I_{los}^2 \rangle^{1/2}$ ) values of the specific data versus time.

### 2.3.1 Intensity Continuum Variations

For the intensity continuum temporal profiles we have used data from *MDI* (having the same characteristics as the Doppler maps described in Section 2.1) and Global Oscillation Network Group (*GONG*) data. The raw data taken from *GONG* (courtesy Sean Mcmanus, National Solar Observatory) consist of full disk images (860×860 pxs) and represents a measure of radiation in a 0.7 Å bandpass centred on the Ni I 6768 Å line with an equivalent width of 0.07 Å.

It has already been established that there is a very good temporal and spatial correlation between the intensity continuum and sun quakes (Donea et al., 2006a,b; Moradi et al., 2006b; Beşliu-Ionescu et al., 2007a; Martinez-Oliveros et al., 2007).

Donea et al. (2006b) and Beşliu-Ionescu et al. (2007a) state that the persistence of a sudden, co-spatial white-light signature in flares where no energetic protons were evident is consistent with acoustic emission driven by back-warming of the low photosphere by radiation from a heated overlying chromosphere. Similar conclusions were drawn by Moradi et al. (2007), too.

Martinez-Oliveros et al. (2007) found kernels spatially aligned close to similar hard X-ray kernels in the 12–25 keV energy range. Visible continuum emission, similarly aligned with the holographic kernels, reinforces the hypothesis that heating of the photosphere contributes to the observed seismic emission.

### 2.3.2 Doppler Velocities Variations

We have used *MDI*'s Dopplergrams (the same Doppler maps described in Section 2.1) to study the local variation of the photospheric velocities during the acoustic emission.

Moradi et al. (2007) compared Doppler LOS velocity profiles with hard X-ray emission and the acoustic emission to find a very good correlation between their maxima. They suggested that high-energy particles supply the energy that drives the acoustic emission, and it is evident from the electromagnetic emission attributed to these particles that they contain more than sufficient energy for this purpose.

Doppler velocity variations will give us specific details about the displacements of plasma at the photospheric level and correlations between the magnitude of this displacement and the acoustic source power.

### 2.3.3 Magnetic Variations

Using the magnetograms from *MDI* we have also analysed the temporal profiles of the magnetic transients. The purpose of this study is to see if there is any correlation between the magnetic transients and other transients associated with the seismic emission, such as studied in [Beşliu et al. \(2005b\)](#); [Beşliu-Ionescu et al. \(2006b\)](#); [Donea et al. \(2006b\)](#); [Martinez-Oliveros et al. \(2007, 2008a\)](#).

Given that we only had *MDI*'s NiI data, one can argue the veracity of the recorded transients. However, this kind of study had been performed by Zharkova & Kosovichev ([Zharkova and Kosovichev, 2002b](#); [Kosovichev and Zharkova, 2001](#)) and many others. We would like to add our interpretation to this phenomenon.

We must emphasize another aspect of the observed variations of magnetic field. The magnetograms may render a false signature during the white light flare, for example, due to changes in the thermal structure of the photosphere and the effect this would have on the formation of the Ni I 6768 Å. However, the further possibility should be considered that the nominal penumbral magnetic signature is significantly contaminated by magnetically insensitive molecular lines, such as are formed by TiO, in the neighbourhood of Ni I 6768 Å. If these molecules are destroyed in great numbers by the thermal or radiative enhancement evident in the sunspot photosphere during the white light flare, the magnetic signature could be changed accordingly, and a considerable amount of time may elapse (10 minutes) before the molecular composition of the penumbral photosphere recovers to pre-flare conditions.

To study the magnetic field evolution in time, we used *MDI* line-of-sight magnetograms consisting of continuous, full-disk Doppler images obtained at a cadence of one minute over a two-hour interval. The noise level for the magnetograms is about 20 G.

[Kosovichev and Zharkova \(2001\)](#) named the magnetic variations, magnetic transients. They suggested that the transients are caused by either the interaction of high-energy particles with the photosphere or by variations in the line profile due to the impulsive heating. However, [Zharkova and Kosovichev \(2002b\)](#) calculated that the line profile inversion is a very weak

and short-lived (a few seconds) process. A second physical scenario with a high-energy particle beam interacting with the photosphere could be ruled out since it is less likely that an M-class flare can efficiently accelerate such particles (Machado et al., 1989).

Beşliu et al. (2005b) studied the magnetic field variations for the two “Halloween Flares” October 28 and 29, 2003 which have seismic emission associated. They detected rapid variations of the photospheric magnetic field only in AR 10486, during the acoustically active flare on October 29, 2003. They found that the largest variation of  $\sim 60$  G occurred in the region with the weakest detected acoustic seismicity. The region with lesser variations of  $\sim 35$  G produced the largest acoustic signal detected in AR 10486. Their conclusion referring to the Halloween flare magnetic field variations states that the acoustic power of the seismic sources and the amount of magnetic energy released during the flare are in inverse proportion.

Donea et al. (2006b) also found that the acoustic signature was spatially and temporally coincident with suddenly changing magnetic signatures, suggesting that suddenly changing magnetic forces might have contributed to the seismic emission.

Recent theoretical and computational modelling of magnetized photospheres and subphotospheres (Cally, 2006; Bogdan et al., 2002) has revealed that fast-to-slow or vice versa magneto-acoustic wave conversion occurs near surfaces where the sound and Alfvén speeds coincide, provided the local attack angles of the wave on the magnetic field lines is small. Depending on the precise magnetic structure of the active region, and the location of the acoustic source, a complex array of mode conversions and refractions is likely. Schunker et al. (2005) have shown that magnetic forces are of particular significance for acoustic signatures in penumbral regions, where the magnetic field is significantly inclined from vertical. Therefore, understanding the 3D magnetic configuration of the coronal loops hosting flares would give us a powerful control utility for seismic diagnostics of active region sub-photospheres. This will be useful for addressing questions concerning the MHD of inclined magnetic fields, the role of fast and slow magneto-acoustic mode coupling in magnetic photospheres, sub-photospheric thermal structure, and how wave generation by turbulence in active region sub-photospheres differs from that in the quiet sub-photosphere.

Thus a precise interpretation of flare observations requires careful MHD modelling.

## 2.4 Spectral Hardness

We have also computed the spectral hardness of the continuum emission associated with sun quakes. The spectral hardness is computed the same way as the acoustic power, by integrating the mean square of the local amplitude ( $A$ ) within the source region:

$$P_a = \int_{S_q} |A|^2 dS. \quad (2.5)$$

For these computations we have used two different sets of data: high resolution continuum data given by *SOHO-MDI* and low resolution data from the *GONG*.

Given that the *GONG* instruments are ground based, the difference in the quality of data between *MDI* and *GONG* data was considerable. Therefore, we have used the technique described by [Lindsey and Donea \(2008\)](#) to filter *GONG* data in order to compute the spectral hardness of the white light emission. The raw data taken from *GONG* is the same data described in Section 2.3.1. The instrument *SOHO-MDI* uses two observing modes: the “normal resolution” mode, which generated full disk images of 1024×1024 pxs with a nominal pixel separation of the projection of 2 arcsec, and the “high resolution” mode, which generated images of 1024×500 pxs at a 0.6 arcsec nominal pixel separation focused on the Sun’s centre. For the spectral hardness computations we have used the 1 minute cadence high resolution data.

The *GONG* data has undergone a filtering process using the technique described in [Lindsey and Donea \(2008\)](#). They considered possible effects upon the observations such as: local stochastic translation of the region to be studied (defined by a vector displacement  $\alpha$ ) and the smearing of the image (defined by a scalar parameter  $\beta$ ). The effects of the smearing can be approximated by a field of the following form:

$$I'(\mathbf{r}) = I(\mathbf{r}) - \boldsymbol{\alpha} \cdot \nabla I(\mathbf{r}) + \beta \nabla^2 I(\mathbf{r}) \quad (2.6)$$

$I'(\mathbf{r})$  represents the intensity map of the translated and smeared source at location  $\mathbf{r}$  in the image plane such that  $I(\mathbf{r})$  would represent that of the un-smearing, untranslated source.

The characteristic lifetime of atmospheric scintillation is only a fraction of a second. For intensity maps integrated over one minute, during which

the solar disk image is continually stabilized by limb tracking,  $\alpha$  averages to only a small fraction of what it could be for a single, instantaneous snapshot. This is the case for the *GONG* observations, in which each pixel represents radiation integrated for a full minute. The smearing that characterizes the integrated image might be significantly greater than for an instantaneous snapshot, but it is more likely isotropic. Figure 3 from [Lindsey and Donea \(2008\)](#) makes it clear that atmospheric smearing integrated over a full minute varies significantly from one minute to the next, and it is straightforward to confirm that the pattern that appears in Figure 3b conforms closely to some constant times the Laplacian of either of the two intensity maps from which the difference was computed.

Further more, [Lindsey and Donea \(2008\)](#) state that in practice, what is more important than whether Equation 2.6 accurately represents the overall smearing introduced by the terrestrial atmosphere is that it can be applied to just the variation in smearing.

The procedure [Lindsey and Donea \(2008\)](#) prescribe, then, is to adjust  $\alpha$  and  $\beta$  so as to optimize the fit of each image in the time series to a single reference image in a region that excludes that in which significant white-light emission actually occurs during the flare. The resulting image will be the difference between that intensity and the preflare intensity averaged over a 300 second period. Having these new images stabilised it is possible to apply essentially the same spectral analysis techniques to *GONG* intensity observations as those applied to the *MDI* Dopplegrams for helioseismic applications.

With the intensity maps stabilized to this degree, it is now possible to apply essentially the same spectral-analysis techniques, to *GONG* intensity observations of active regions as those applied to the *MDI* Doppler images for helioseismic applications.

We have computed the excess power in the 2.5–4.5 and 5–7 mHz intensity from the smearing-corrected *GONG* intensity maps and the *MDI* intensity data and compared them to concurrent maps of the acoustic power (i.e. egression power).

I will present the detailed analysis of the egression power emission of the acoustically active flares in Chapter 3 and show comparisons to excess power emissions in Chapter 5.

# Chapter 3

## Comprehensive Survey of Sun Quakes – Data Analysis

This chapter will present a detailed analysis of the detection and properties of the seismic sources, that form the major focus of my work. I will start with a short motivation for our survey and a general characterization of Solar Cycle 23 (SC23). Then I will present the description of each active region that hosted an acoustically noisy solar flare and its seismic source properties.

### 3.1 Sun Quakes

Following [Donea et al. \(1999\)](#) and [Donea and Lindsey \(2005\)](#), in 2005 we begun a comprehensive survey of the X-class flares observed by *SOHO-MDI* in order to detect solar flare generated sun quakes. This work has brought an explosion in the discovery of sun quakes in SC23, some generated from relatively small, M-class, flares. By June, 2005, we had discovered 11 seismic sources generated by X-class solar flares and two generated by M-class flares.

We first presented our results on-line at <http://users.monash.edu.au/~dionescu/sunquakes/sunquakes.html>. We then published our first discoveries of several X-type acoustically noisy flares in [Beşliu et al. \(2005a\)](#). This was followed by [Beşliu-Ionescu et al. \(2006c\)](#) where we showed that M-type solar flares can produce sun quakes, too. A more detailed statistical view of our survey was published in [Donea et al. \(2006b\)](#).

Then we took the initiative of studying some of these sun quakes in detail ([Beşliu-Ionescu et al., 2006a,b](#); [Donea et al., 2006b](#); [Beşliu-Ionescu et al.,](#)

2007a; Moradi et al., 2007).

To date, we have discovered and analysed about 20 sun quakes generated by a very wide range of solar flares, the strongest being an X17 (Donea and Lindsey, 2005) and the weakest being an M6.7 (Martinez-Oliveros et al., 2008b).

The purpose of this survey has been to improve our statistical database on acoustic emission from flares and our understanding about the variety of dynamical factors that can determine the appearance of flare emission into the solar interior. With the sun quakes so far surveyed by us, there has been little correlation between the *GOES* X-ray energy of the flare and the energy of the seismic transient. While the proportion of M-class flares that are acoustically active is substantially smaller than of X-class flares, the increasing number of weaker flares suggests that a continuation of this survey will further improve the physics of acoustic flares.

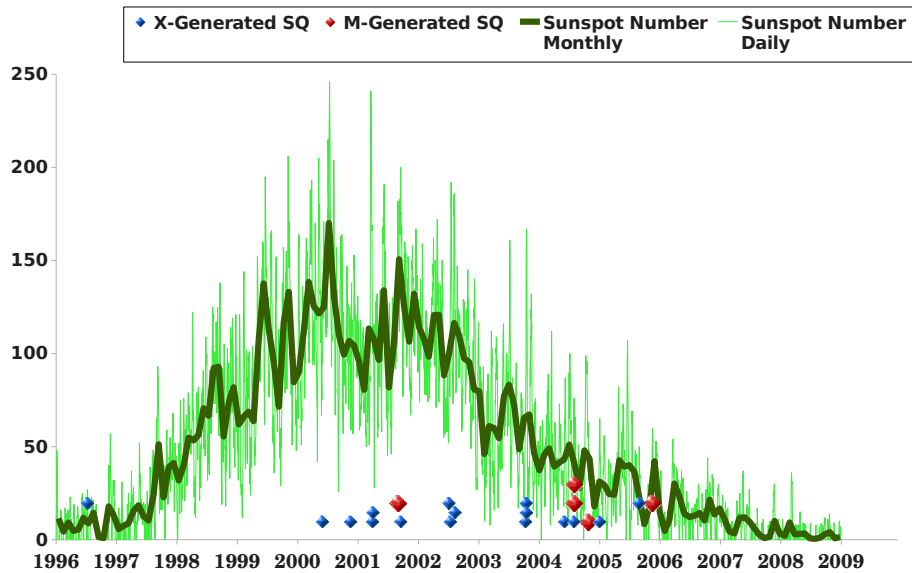


Figure 3.1: Position of sun quakes discovered to date against the SC23.

Figure 3.1 shows SC23 characterised by the daily (thin green line) and the monthly (thick dark green line) sunspot number. It had two relative maxima around the middle of 2000 and 2001. Overplotted are the sun quakes

generated by X-type solar flares (blue diamonds) and M-type solar flares (red diamonds).

Since the *MDI* database covered only a fraction of the flares that occurred during SC23 (namely a small part at its beginning, the maximum, and its descending phase) we cannot positively say that the descending phase has a more prominent seismicity than the rest of SC23 (Kosovichev, 2006).

It would appear that the Helioseismic Magnetic Imager (*HMI*), initially scheduled for launch in 2008 and launched in February 2010, on the Solar Dynamics Observatory (*SDO*), will observe scores of sun quakes over the full term of SC24. This expectation opens major new prospects for *HMI*, not only for understanding the dynamics of flares but for addressing important outstanding questions that bear on the use of helioseismic observations to probe the subphotosphere of active regions. A better understanding of the causality of the sun quakes will lead to a better understanding of the flares, and therefore a better model which could, eventually, predict the outcome of a particular flare.

All the sun quakes listed in the following sections have been detected with the helioseismic holography technique described in Section 2.1. For a clear confirmation of the acoustic sources we used comparisons to other excess emissions and the movement of the wave front in time. We have filtered out all the acoustic sources which lasted for less than 8 minutes.

The apparently long,  $\sim 8$  min, duration of the egression power signature is an artifact of the truncation of the helioseismic spectrum by a 2 mHz pass-band (see Equation 3.1). The egression power signatures that result are temporally smeared to a minimum effective duration of order

$$\Delta t = \frac{1}{\Delta\nu} = \frac{1}{2 \text{ mHz}} = 500 \text{ s.} \quad (3.1)$$

This means that the acoustic signature of the flare generally begins several minutes before the actual onset of the flare and lasts for several minutes after, even if the actual acoustic disturbance was instantaneous.

Firstly, we present a very short summary of the sun quakes known to date split into two tables, as sun quakes generated by X-type solar flares in Table 3.1 and sun quakes generated by M-type solar flares in Table 3.2.

Table 3.1 differentiates between sun quakes discovered before our survey and sun quakes discovered during our survey, using bold type letters for the latter. We would like to specify that there were no discoveries of sun quakes generated by M-type solar flares before our studies.

Date	Class	3 mHz (ergs)	6 mHz (ergs)	Begin (UT)	Peak (UT)	End (UT)
1996 Jul 09	X2.6	$6.3 \times 10^{27}$	$2.2 \times 10^{26}$	09:01	09:13	09:19
2003 Oct 28	X17.2	$2.1 \times 10^{26}$	$1.2 \times 10^{26}$	11:00	11:07	11:12
		$3.1 \times 10^{26}$	$1.6 \times 10^{26}$	11:01	11:09	11:15
2003 Oct 29	X10.0	$5.1 \times 10^{26}$	$2.3 \times 10^{26}$	20:35	20:43	20:50
<b>2000 Jun 6</b>	X2.3	$2.8 \times 10^{27}$	$2.2 \times 10^{26}$	14:57	15:05	15:11
<b>2000 Nov 24</b>	X2.6	$6.5 \times 10^{27}$	$1.3 \times 10^{27}$	04:54	05:00	05:06
<b>2001 Apr 6</b>	X5.6	$4.7 \times 10^{26}$	$2.8 \times 10^{26}$	19:13	19:20	19:28
		$1.2 \times 10^{27}$	$2.8 \times 10^{26}$	19:13	19:20	19:23
<b>2001 Apr 10</b>	X2.3	$3.2 \times 10^{26}$	$6.2 \times 10^{25}$	05:01	05:04	05:09
<b>2001 Sep 24</b>	X2.6	$6.7 \times 10^{25}$	$5.4 \times 10^{25}$	09:35	09:37	09:45
<b>2002 Jul 15</b>	X3.0	$3.7 \times 10^{27}$	$7.1 \times 10^{26}$	19:52	19:59	20:06
<b>2002 Jul 23</b>	X4.8	$9.0 \times 10^{25}$	$6.1 \times 10^{25}$	00:17	00:24	00:30
<b>2002 Aug 21</b>	X1.0	$2.9 \times 10^{26}$	$1.5 \times 10^{26}$	05:24	05:31	05:39
<b>2003 Oct 23</b>	X5.4	$2.4 \times 10^{26}$	$5.2 \times 10^{25}$	08:45	08:47	08:53
<b>2004 Jul 16</b>	X3.6	$9.5 \times 10^{26}$	$5.8 \times 10^{26}$	13:48	13:56	14:03
<b>2004 Aug 13</b>	X1.0	$4.2 \times 10^{26}$	$1.0 \times 10^{26}$	18:07	18:11	18:16
<b>2005 Jan 15</b>	X1.2	$2.1 \times 10^{27}$	$1.0 \times 10^{27}$	00:33	00:41	00:47

Table 3.1: Summary of seismic sources generated by X-type solar flares: first and second columns show the solar flare date and its type; third and fourth column show the estimated egression power energy released at the maximum of the emitting source at 3.5 and 6 mHz, respectively. Last three columns show the specific times of the seismic source evolution. For comparison – estimated energy released during flares  $\sim 10^{32}$  ergs.

Date	Class	3 mHz (ergs)	6 mHz (ergs)	Begin (UT)	Peak (UT)	End (UT)
<b>2001 Sep 09</b>	M9.5	$1.2 \times 10^{27}$	$6.9 \times 10^{26}$	20:38	20:44	20:49
<b>2004 Aug 14</b>	M7.5	$4.7 \times 10^{26}$	$5.9 \times 10^{25}$	05:40	05:45	05:51
<b>2004 Aug 15</b>	M9.4	$1.8 \times 10^{26}$	$3.0 \times 10^{26}$	12:35	12:40	12:45
<b>2005 Dec 02</b>	M7.8	$2.5 \times 10^{28}$	$5.7 \times 10^{27}$	10:05	10:12	10:20
<b>2001 Mar 10</b>	M6.7	$1.8 \times 10^{26}$	$3.7 \times 10^{25}$	04:00	04:05	04:10

Table 3.2: Summary of seismic sources generated by M-type solar flares: Same as Table 3.1.

Both tables have the same column structure showing the main characteristics of the seismic source and its progenitor solar flare as Class - flare type, 3 mHz and 6 mHz - energy estimations for the seismic source in the 2 mHz bandwidth centred at 3 and 6 mHz integrated over the sun quake area, and specific times for each source.

Next we present descriptions for each sun quake.

## 9 July 1996

The first solar X-type flare of SC23 was the X2.6 flare detected on July 9, 1996. It was not a very short flare, but an impulsive one, with 11 minutes for the ascending phase, starting at 09:01 UT and ending at 09:49 UT. It was hosted by the  $\beta\gamma\delta$  NOAA 7978 AR, situated at S10W38.

This was the first discovery of a solar quake, detected by direct imaging (Kosovichev and Zharkova, 1998). Donea et al. (1999) computed its seismic source using computational helioseismic holography.

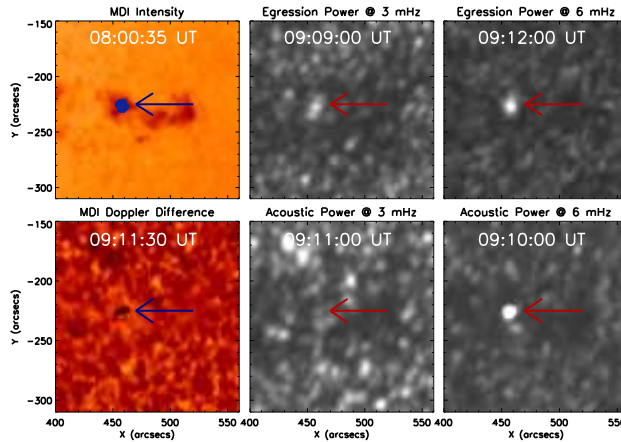


Figure 3.2: View of AR NOAA 7978 on July 9, 1996. Each panel shows specific times and wavelengths. The arrow points the location of the sun quake. Overplotted on the intensity continuum are contour levels of the egression power at the maximum of its emission.

Figure 3.2 shows a general description of AR 7978. The first frame in the first row is an *MDI* intensity continuum. The contours overplotted are level contours of 10%, 30%, 50%, 70% and 90% of the egression power emission

at its maximum, namely at 09:12 UT. The next two frames are the egression power maps centred at 3 and 6 mHz.

All the frames showing egression and acoustic power snapshots from here on have been “smeared”. We convolve the image with a Gaussian smear of 0.004 width to increase the contrast for the enhanced emissions.

Both egression and acoustic power at 6 mHz show excess emissions, the acoustic maximum being ahead the seismic transient by about three minutes.

On the next row of Figure 3.2 we can see an *MDI* Doppler difference (that is two consecutive Dopplegrams taken at 09:11 and 09:12 UT subtracted one from the other). The behaviour of this photospheric signature will be discussed in detail in the next chapter. The last two frames show the acoustic power maps also centred at 3 and 6 mHz. Only the acoustic power transient at 6 mHz is noticeable against the solar background noise, being very well correlated both spatially and temporally with the egression power signature. The arrow in all frames points to the egression power maximum as seen in the last frame of the first row.

The sun quake has an oval shape with an area of about 149 Mm<sup>2</sup>.

The areas of the acoustic signatures were determined by counting the pixels they covered. To determine the dimensions of each pixel in Mm<sup>2</sup>, I multiplied the dimensions of each pixel in solar radii, determined by the geometry of the *MDI* image, by  $R_{\odot}^2$ , where  $R_{\odot} = 695.997$  Mm (Allen, 1973) is the solar radius. Corrections for foreshortening were made by dividing the area,  $A_c$ , of the region as it appears in the solar image, by the cosine of the inclination,  $I$ , of the line of sight from the normal to the Sun’s surface:

$$A_r = A_c / \cos I. \quad (3.2)$$

In terms of Carrington coordinates,

$$\cos I = \cos B_0 \cos B \cos (L - L_0) + \sin B_0 \sin B \quad (3.3)$$

where  $L_0$  and  $B_0$  are the Carrington coordinates of Sun centre in the *MDI* image, and  $L$  and  $B$  are the Carrington coordinates of the centre of the active region.

Figure 3.3 depicts the temporal evolution of the sun quake. The first two panels plot the egression power temporal profile in the 2–4 mHz band (panel a) and 5–7 mHz (panel b), integrated over the sun quake area. The central vertical line represents the maximum of the seismic emission and the other two lines the time resolution as  $\pm 8$  minutes.

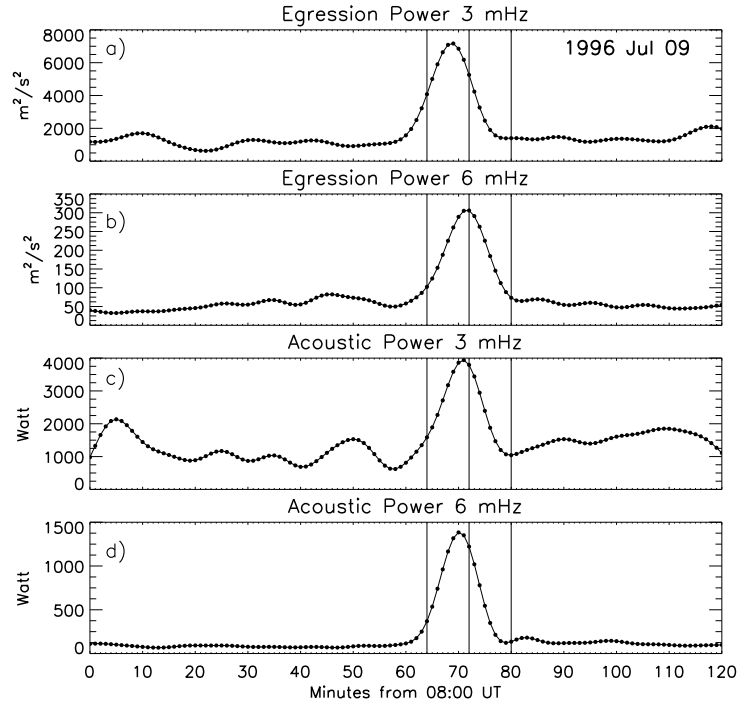


Figure 3.3: Plots of the 2–4 mHz (panel a) and 5–7 mHz (panel b) egression power of seismic signatures on July 9, 1996 solar flare. The central vertical line represents the maximum of the seismic signature of the flare, while the other two vertical lines represents the maximum  $\pm 8$  minutes. Panel c and d show the acoustic power of detected sources at 3 and 6 mHz.

This case was very a fortunate one, where even the 3 mHz signature in the egression power maps is visible and very easy to distinguish against the background emission. The peak in this excess emission is three minutes ahead of the 6 mHz signature and is about three times larger than the background emission.

Panels c) and d) in Figure 3.3 show the acoustic power integrated over the seismic source area, in 2 mHz bands centred at 3 and 6 mHz. These emissions are only two minutes ahead of the peak of the seismic source and represent about three and seven times, respectively, the background emission. The acoustic power increased starting at 09:04 UT, reached its peak at 09:11 UT and ended after another 10 minutes.

We have also estimated the energy released at the photospheric level by

a particular seismic source using Equation 3.4

$$E = \frac{1}{2} \rho c t \times (M_2 - M_1) \times A. \quad (3.4)$$

Here,  $\rho$  is  $2.07 \times 10^{-7}$  g/cm<sup>2</sup> density at the photospheric level according to the Christensen-Dalsgaard model,  $c$  (sound speed) is  $7.79 \times 10^5$  cm/s (both density and sound speed values taken for the photospheric level),  $t$  is the time between the frames corresponding to the reading of  $M_1$  and  $M_2$  (mean 1 and mean 2), where  $M_2$  is the averaged value of the 6 mHz, and 3 mHz respectively, egression values over the seismic transient region, at its maximum (or at the flaring time) and  $M_1$  is the averaged value of the 6 mHz, respectively 3 mHz, egression value over a quiet region taken  $t$  seconds before (pre-flaring time) and  $A$  is the sun quake area.

For the July 9, 1996 sun quake we found the energy released in the 2–4 mHz bandpass to be  $6.33 \times 10^{26} \pm 6.27 \times 10^{25}$  ergs and in the 5–7 mHz bandpass  $2.17 \times 10^{26} \pm 1.34 \times 10^{25}$  ergs.

## 6 June 2000

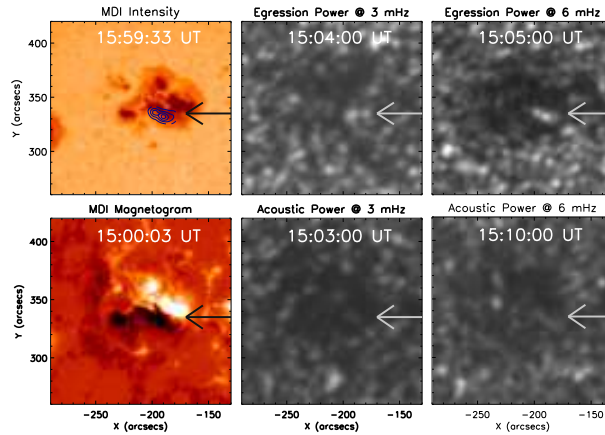


Figure 3.4: View of AR NOAA 9026 on June 6, 2000. Each panel shows specific times and wavelengths.

The X2.3-type flare that triggered this sun quake started at 14:58 UT, peaked at 15:25 UT and ended at 15:40 UT, with the times as given by the *GOES* integrated flux. This flare was also characterised by a proton event. It

was generated in the  $\beta\gamma\delta$  AR NOAA 9026 (N21E10). The sun quake lasted for 14 minutes, starting 14:57 UT and having its maximum at 15:05 UT.

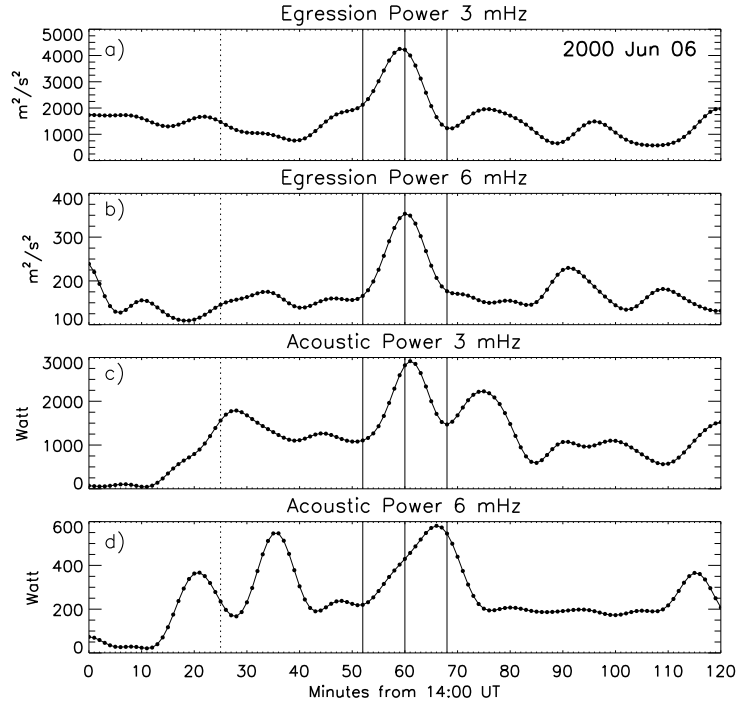


Figure 3.5: Same plots as Figure 3.3 for June 6, 2000 solar flare. Here, the first vertical dashed line represents the beginning of the real data.

Figure 3.4 shows the AR 9026 that hosted the seismic source. The first panel on the first line shows an *MDI* intensity continuum map with five levels (10%, 30%, 50%, 70%, 90%) of the egression power maximum contours. The seismic source is situated in the southeastern region of the penumbra. The next two panels show the egression power snapshots at 3 and 6 mHz. The seismic source is obvious in the 6 mHz centred band-pass and fainter at 3 mHz. The sun quake has a total area of about 149 Mm<sup>2</sup>.

The next row in Figure 3.4 begins with an *MDI* magnetogram from which we can see that the seismic signature has the same WE orientation and position as the magnetic neutral line. The next two panels in the same row are snapshots of the acoustic power maps at the maximum of the emission at 3 and 6 mHz, respectively. Although they are comparable in intensity with the background emission, the acoustic signature at 6 mHz can be detected

near the arrow.

Figure 3.5 shows the temporal profiles of the egression and acoustic power emissions. The vertical line at 04:25 UT shows the start of the real (*MDI* Dopplergrams) data taken into account in this computation. The first and second panel show egression power emissions at 3 mHz and, respectively, 6 mHz, both maxima being about twice the background noise. The last two panels show the acoustic emissions at 3 and 6 mHz. The peak at 6 mHz in the acoustic emission is delayed by approximately 5 minutes, but it is distinguishable from other emissions. Disregarding the other peaks, unrelated to seismic emissions, the peak for the acoustic emission is about three times the background noise.

The estimated energy released into the photospheric level at 3 mHz is:  $2.81 \times 10^{27} \pm 2.30 \times 10^{26}$  ergs and at 6 mHz:  $2.18 \times 10^{26} \pm 2.88 \times 10^{25}$  ergs.

## 24 November 2000

This sun quake was generated by an X2 type flare on a  $\beta$  type active region, AR NOAA 9236. The flare started at 04:55 UT, had its maximum at 05:02 UT and ended six minutes later. It was also accompanied by a proton event. The associated sun quake started at 04:54 UT, had its maximum after six minutes and ended at 05:08 UT.

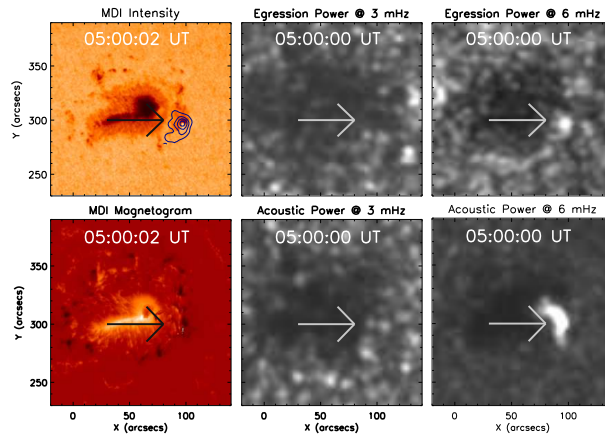


Figure 3.6: View of AR NOAA 9236 on November 24, 2000. Each panel shows specific times and wavelengths.

Figure 3.6 shows a general description of AR 9236 (N21W07). This is one of the few rare cases when *MDI* covered the whole solar flare in high resolution data. Therefore we have a more detailed view of the location of the seismic source as seen in the first frame of this figure. The centre of the seismic source is situated at the same location as the western spot. The white light emission is also visible beneath the contour levels and it will be broadly discussed in the next chapter.

The next two frames of Figure 3.6 show the 3 and 6 mHz egression power maps at the maximum of the seismic emission. Although the 3 mHz seismic emission is not visible against the 5-minute oscillation, the 6 mHz seismic emission is easily seen in the last frame on the top row.

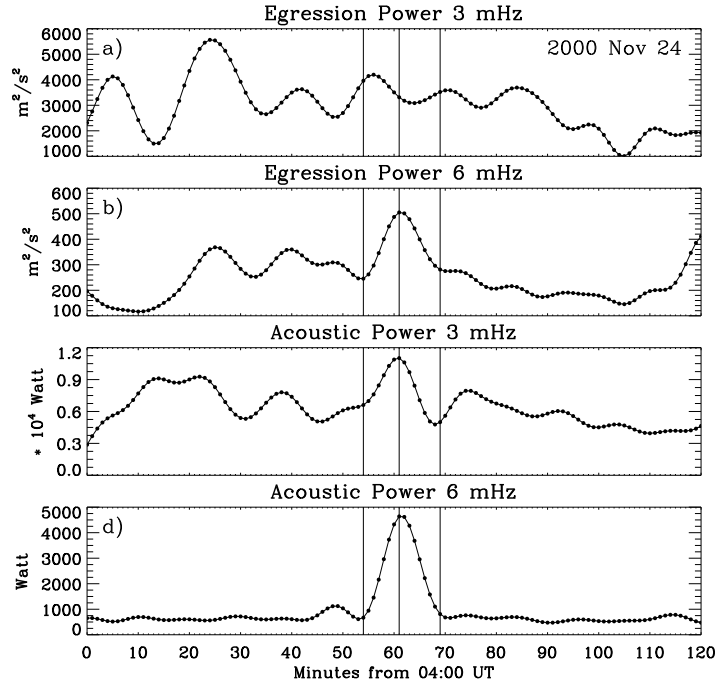


Figure 3.7: Same as Figure 3.3 for the November 24, 2000 solar flare.

The second row of Figure 3.6 shows an *MDI* magnetogram and the 3 and 6 mHz acoustic power maps. This sun quake spreads over 122 Mm<sup>2</sup>. This seismic emission is also coaligned with the local magnetic neutral line of the western spot. The acoustic emission shown in the last frame of the bottom row is quite extended and spreads over that entire side spot.

Figure 3.7 shows the temporal profiles of the egression and acoustic power emissions for the November 24, 2000 sun quake. In this figure we can see, on the first row, the more common behaviour of the 3 mHz egression power, that is, a practically unseen peak emission.

The second row of Figure 3.7 clearly shows the excess emission of the egression power at 6 mHz (almost three times stronger than the background noise). The peaks in the acoustic power are easy to observe both at 3 and 6 mHz, the latter being about six times above background noise.

The estimated energy released into the photospheric level at 3 mHz is:  $6.45 \times 10^{27} \pm 3.19 \times 10^{26}$  ergs and at 6 mHz:  $2.27 \times 10^{27} \pm 1.86 \times 10^{26}$  ergs.

## 6 April 2001

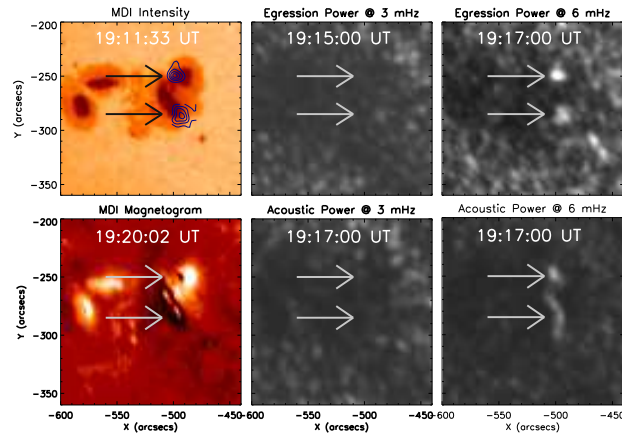


Figure 3.8: View of AR NOAA 9236 on April 6, 2001. Each panel shows specific times and wavelengths.

Another acoustic source was detected in the  $\beta\gamma$  type active region AR 9415, during the X5.4 flare which began at 19:10 UT, had a maximum at 19:21 UT and ended at 19:31 UT. The AR was situated at S21E34. The seismic signature of the flare at 6 mHz is very strong, possessing a double structure corresponding to the footpoints of the coronal loop. This will be described in detail in Chapter 4. We make a point in noticing that only the large flare of October 28, 2003 presented a similar complexity, with a double acoustic source evolving within  $\sim 15$  minutes. The seismic sources are

spatially extended, located in the penumbrae of the right sunspots of AR 9415 seen in the first panel in Figure 3.8.

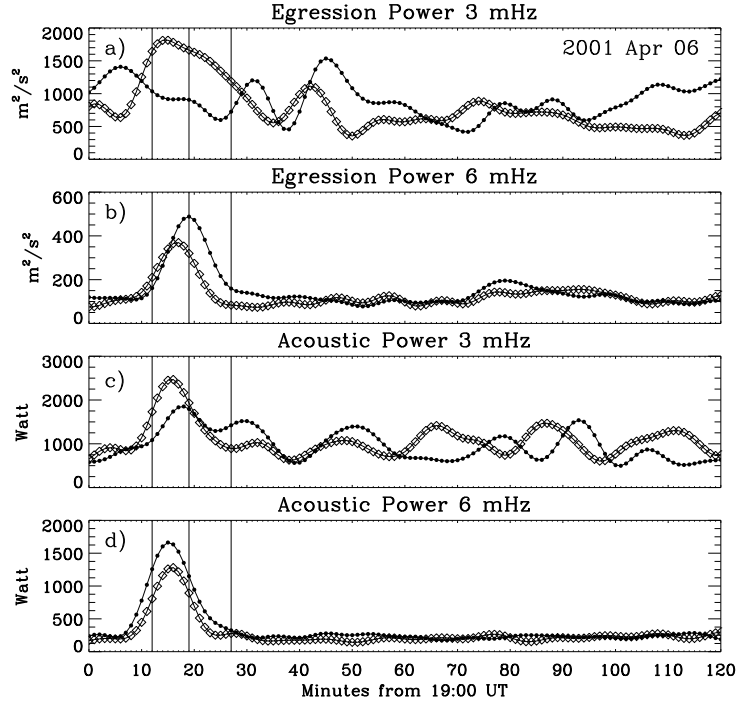


Figure 3.9: Same as 3.5 for the seismic signatures of the April 6, 2001 solar flare. The dotted line shows the evolution for the northern seismic source and the diamond represents the southern source as seen in Figure 3.8.

Figure 3.8 presents an *MDI* intensity continuum, 3 mHz and 6 mHz egression power maps on the first row. This sun quake is composed of two almost round shapes structures spreading over 140 and, respectively, 186  $\text{Mm}^2$ . Again, there is no noticeable excess emission at 3 mHz. The seismic emission at 6 mHz shows two different structures evolving with just about two minutes difference.

On the second row we can see an *MDI* magnetogram, followed by the acoustic power maps at 3 and 6 mHz. The seismic sources are aligned with the magnetic neutral line. The acoustic power snapshot at 6 mHz is quite extended, but the double structured emission is clearly seen.

Figure 3.9 shows the time evolution of the egression power at 3 mHz (first panel) and 6 mHz (second panel) for the observed seismic sources. The

two sources are represented by a dotted line - the northern source - and a diamond line - the southern seismic source. The northern source lags the southern seismic source by approximately three minutes. The solar flare did not produce significant seismic activity at 3 mHz.

The northern seismic source profile, the dotted line in Figure 3.9, started at 19:13 UT, had a maximum of 19:20 UT and ended at 19:28 UT, while the southern seismic source (the diamond line in Figure 3.9) started at 19:13 UT, evolved to a maximum at  $\sim 19:19$  UT and ended at 19:23 UT.

The excess emission in the egression power at 6 mHz is about five times larger than the background signal for the northern source and about four times larger for the southern seismic source.

The last two panels in Figure 3.9 show the 3 and 6 mHz acoustic power at the location of the double source. The acoustic power at 3 mHz is only about 50% greater than the background noise, but the 6 mHz ones show an almost five times increase in magnitude.

The total estimated energy released into the photospheric level at 3 mHz is:  $1.63 \times 10^{27} \pm 3.39 \times 10^{26}$  ergs and at 6 mHz:  $5.59 \times 10^{26} \pm 3.91 \times 10^{25}$  ergs.

## 10 April 2001

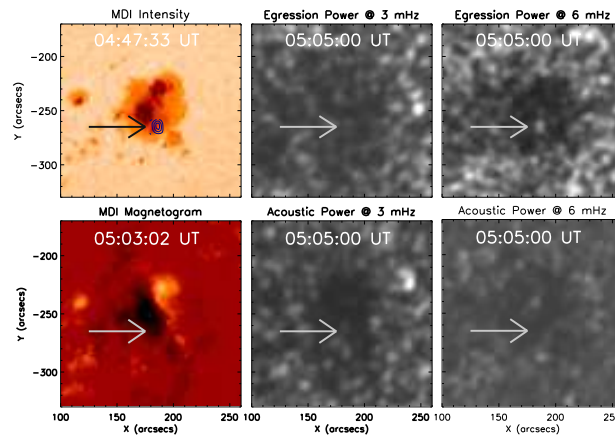


Figure 3.10: View of AR NOAA 9415 April 10, 2001. Each panel shows specific times and wavelengths.

This acoustic source was detected in the same active region AR 9415 as

the sun quake from April 6, which meantime had evolved to be a  $\beta\gamma\delta$  region at S22W20. The X2.3 flare which began at 05:06 UT, had a maximum at 05:26 UT and ended at 05:42 UT is responsible for this seismic emission. This flare was characterized by a proton event too. It is one of the six sun quakes which are accompanied by proton events and the third in our count. The seismic signature is conspicuous at 6 mHz and it evolved for a short period of time, starting at 05:01 UT and ending at 05:09 UT.

Figure 3.10 shows the same structure as Figure 3.8 composing of an *MDI* intensity continuum and the two egression power maps at 3 and 6 mHz.

We can again observe the position of the sun quake with respect to the AR, namely in the penumbra of the main spot. This sun quake has a two kernel structure and its area is about 32 Mm<sup>2</sup>. The 3 mHz egression power map shows no significant signature.

The bottom row of Figure 3.10 shows the *MDI* magnetogram, followed by the 3 and 6 mHz acoustic power maps. The acoustic signature is extremely faint in these frames.

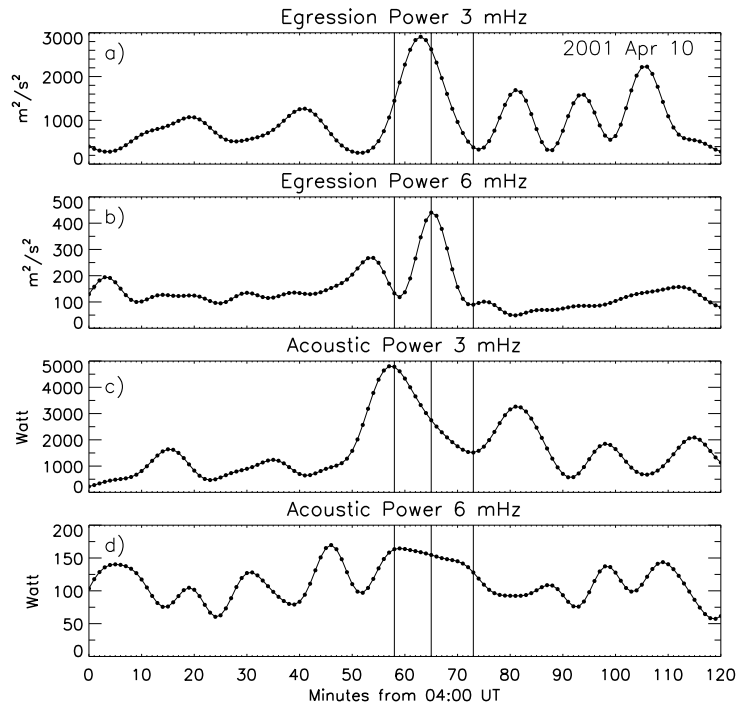


Figure 3.11: Same as 3.9, but for the single seismic source of April 10, 2001 solar flare.

Figure 3.11 shows time series of the egression and acoustic power at 3 and 6 mHz. The seismic source presents a strong egression power signature at 6 mHz and a weak one at 3 mHz. The 3 mHz acoustic power of the seismic source (third panel in Figure 3.11) is about three times stronger than the background emission, but the 6 mHz emission does not show a characteristic enhancement.

This seismic source is also detected in the penumbra of the 9415AR, as shown by the egression power contour plots in Figure 3.10 (upper left frame).

The estimated energy released into the photospheric level at 3 mHz is:  $3.16 \times 10^{27} \pm 9.08 \times 10^{25}$  ergs and at 6 mHz:  $6.15 \times 10^{26} \pm 3.70 \times 10^{24}$  ergs.

## 9 September 2001

A very interesting discovery was made by Donea et al. (2006b). On September 9, 2001 at 20:40 UT, a M9.5 flare occurred at the coordinates S31E26 in the  $\beta\gamma$  AR NOAA 9608. This was the first sun quake discovered to be generated by an M-class solar flare.

This active region was characterised by a main spot which had an extensive penumbra and a negative polarity, but surrounded by positive polarity plages.

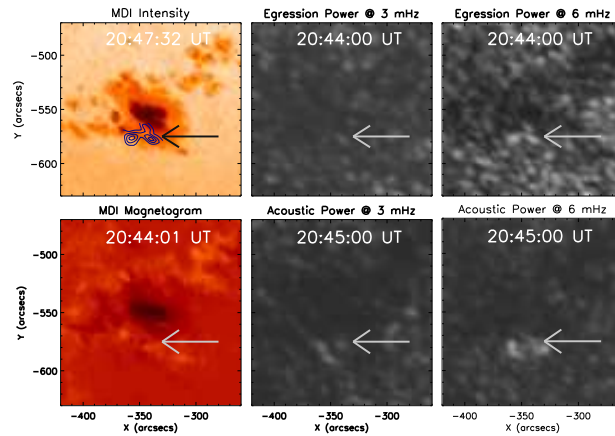


Figure 3.12: View of AR NOAA 9608 on September 9, 2001. Each panel shows specific times and wavelengths.

The X-ray flux from the flare measured by *GOES* reached a peak at 20:46 UT

two minutes after the maximum of the seismic emission. Significant acoustic emission at 6 mHz is visible in the penumbra of the main sunspot as Figure 3.12 shows in the first panel in an intensity continuum map with the contour levels of the egression power maximum overplotted. The next two panels of Figure 3.12 show the egression power maps centred at 3 and 6 mHz.

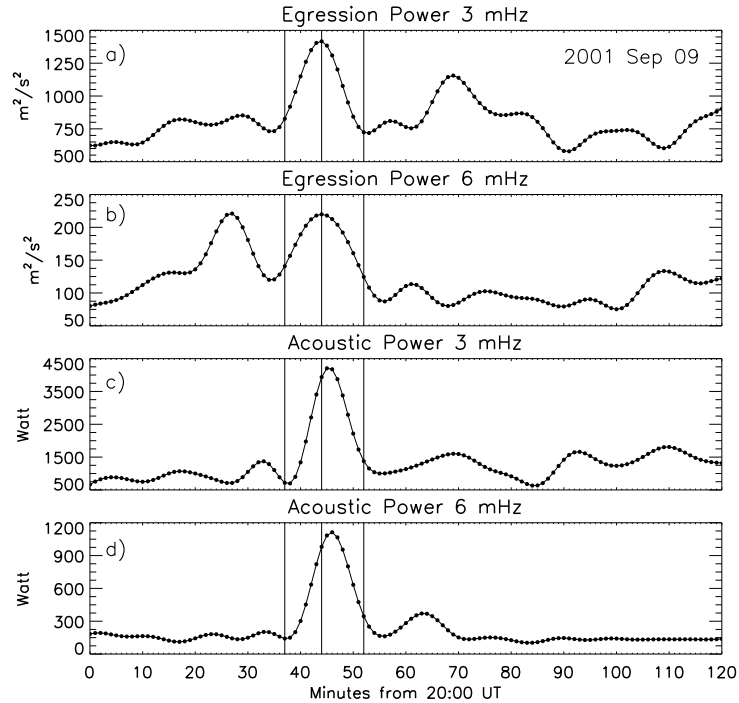


Figure 3.13: Same as 3.9, but for the seismic source of September 9, 2001 solar flare.

The sun quake is shaped as a circular arc spreading over  $\sim 309 \text{ Mm}^2$ . This is a fortunate case where the seismic emission is also visible, although with difficulty, at 3 mHz.

The bottom row of Figure 3.12 shows the *MDI* magnetogram and the two acoustic snapshots at 3 and 6 mHz. We note that the sun quake is located near the magnetic neutral line and has a similar inclination. The acoustic signature is visible in both frequencies and shows a larger surface covered.

The sun quake started at 20:37 UT, reached its peak at 20:44 UT and ended 20:52 UT. Figure 3.13 shows the temporal profile of the egression power emissions at 3 and 6 mHz and the acoustic power at the same frequencies.

The egression excess emission is about twice the background signal at both frequencies, while the acoustical signal exceeds about five times the background level.

The estimated energy released into the photospheric level at 3 mHz is:  $1.20 \times 10^{27} \pm 1.35 \times 10^{26}$  ergs and at 6 mHz:  $2.68 \times 10^{26} \pm 1.08 \times 10^{25}$  ergs.

## 24 September 2001

This sun quake was generated by the X2.6 solar flare on September 24, 2001. The flare evolved for more than one and a half hours, starting at 09:32 UT and having its maximum at 10:38 UT. This flare was also accompanied by a proton event. The flare was generated in the  $\beta\gamma\delta$  type AR 9632 (N21W07).

Figure 3.14 shows the location of the seismic source (first top-left panel) in the penumbra of the small north-eastern spot. The next two frames in Figure 3.14 show the seismic signature at 3 and 6 mHz. The sun quake is shaped as a box with an area of about  $38 \text{ Mm}^2$ . We can not observe any significant activity in the 2–4 mHz bandwidth. The bottom row of Figure 3.14 shows the *MDI* magnetogram and the two acoustic signals at 3 and 6 mHz.

The sun quake started just three minutes after the beginning of the flare and evolved for ten minutes having its maximum at 09:37 UT. The seismic excess emission is clearly visible in Figure 3.15 at 6 mHz with an increase of

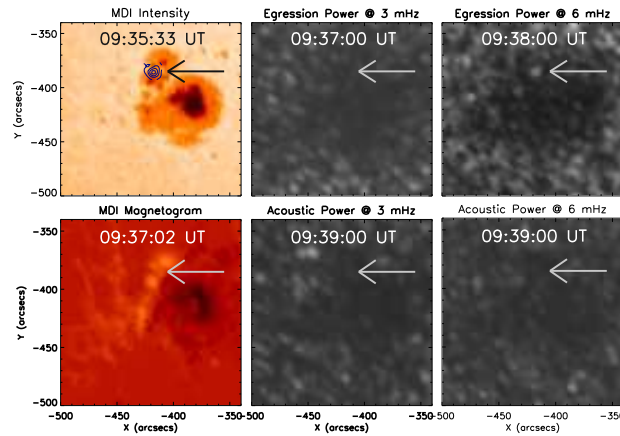


Figure 3.14: View of AR NOAA 9632 on September 24, 2001. Each panel shows specific times and wavelengths.

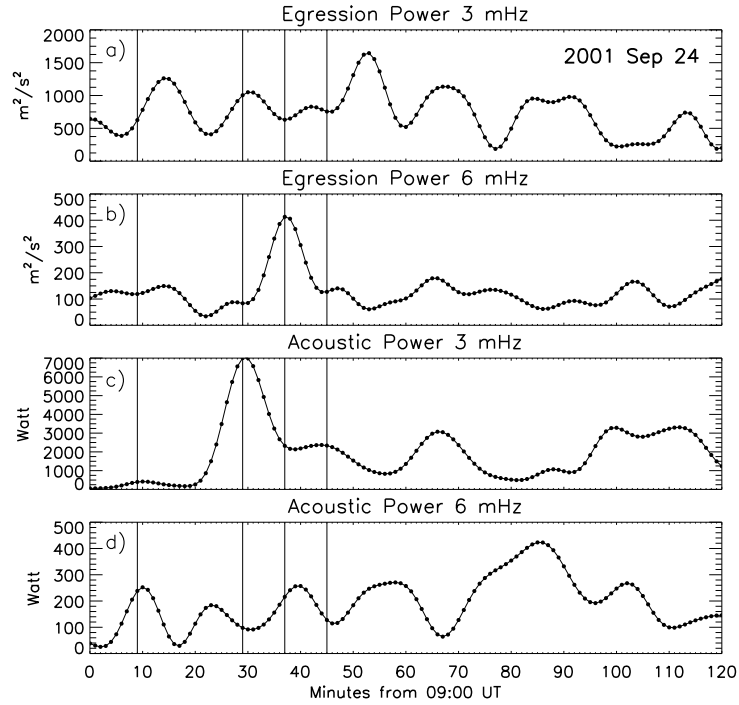


Figure 3.15: Same as 3.9, but for the seismic source of September 24, 2001 solar flare. The first vertical line, at 09:09 UT represents the beginning of the real data from *MDI*.

more than three times the pre- and post-flare values. The other time series of Figure 3.15 do not show a very well correlated behaviour or any excess emissions at all.

The estimated energy released into the photospheric level at 4 mHz is:  $6.70 \times 10^{25} \pm 3.07 \times 10^{25}$  ergs and at 6 mHz:  $5.36 \times 10^{25} \pm 4.12 \times 10^{24}$  ergs.

## 15 July 2002

This sun quake appeared in the  $\beta\gamma\delta$  AR NOAA 10030, generated by a X3.0 solar flare associated with a proton event, an extensively analysed flare on July 15, 2002 (Liu et al., 2003; Allen Gary and Moore, 2004; Harra et al., 2005; Li et al., 2005; Peterson et al., 2008; Li et al., 2009).

This was a very impulsive and short flare, starting at 19:59 UT, having its maximum after only nine minutes and finishing after another six minutes.

Figure 3.16 shows the general view of the active region hosting the sun quake. Having the same structure as Figure 3.14, the figure consists of: first frame on the first row the active region as seen in intensity continuum; the second and third frame on the first row show the two emissions in egression power, the 3 and 6 mHz centred with 2 mHz bandwidth; the first frame on the second row shows the magnetic structure of this active region; the last two frames show the acoustic power at 3 and 6 mHz.

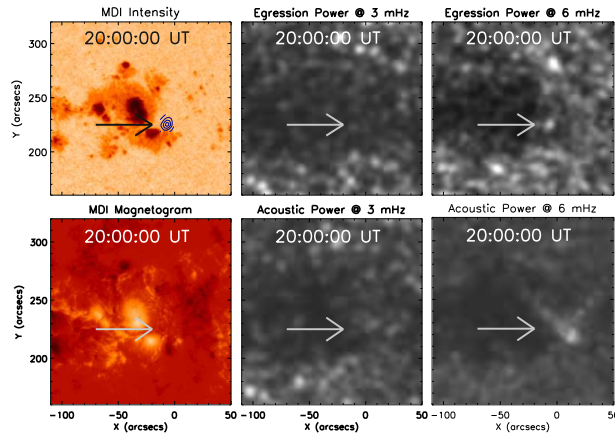


Figure 3.16: View of AR NOAA 10030 on July 15, 2002. Each panel shows specific times and wavelengths.

All arrows show the maximum of the source as seen in the egression power map at 6 mHz. This seismic emission is situated in the plages near the southwestern sunspot. It has a shape similar to two rain drops spreading over  $177 \text{ Mm}^2$ .

Figure 3.17 shows the temporal profiles corresponding to this seismic source in the 3 and 6 mHz egression and acoustic power. The maximum in the 6 mHz egression power emission is about six times the value of the background emission. The sun quake started at 19:52 UT and evolved for 14 minutes, having its maximum at 20:00 UT. This excess emission has a corresponding peak in the 6 mHz acoustic power delayed by about ten minutes, but the 3 mHz emissions show no substantial peak.

The estimated energy released into the photospheric level at 3 mHz is:  $3.72 \times 10^{27} \pm 5.53 \times 10^{26}$  ergs and at 6 mHz:  $7.11 \times 10^{26} \pm 2.02 \times 10^{25}$  ergs.

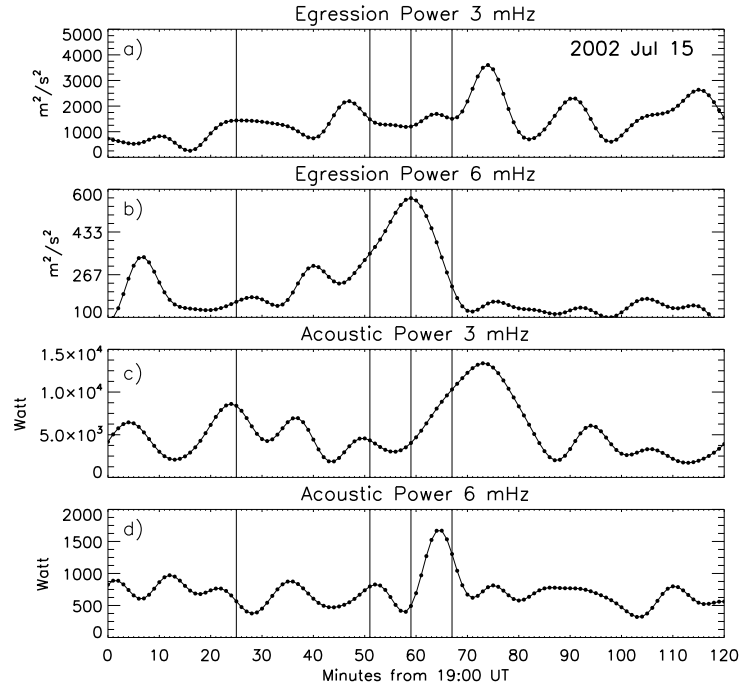


Figure 3.17: Same as 3.9, but for the seismic source of July 15, 2002 solar flare. First vertical line, at 19:25 UT, represents the beginning of the real data from *MDI*.

## 23 July 2002

A very interesting seismic source is that generated by the X4.8 solar flare which ignited on July 23, 2002. It was first reported at <http://users.monash.edu.au/~dionescu/sunquakes/xx.html> in June 2005 and then analysed by [Kosovichev \(2006\)](#). This is also a famous flare with a wide range of observations ([Share et al., 2003, 2004](#)), very useful to understand the physics of the seismic event.

This sun quake was generated by a  $\beta$  type active region situated very close to the solar limb: S12E54. The triggering flare started at 00:18 UT, peaked at 00:35 UT and ended at 00:47 UT.

The sun quake evolved starting 00:27 UT for 13 minutes, having its maximum at 00:34 UT. As seen in the third frame of the first row in [Figure 3.18](#) the seismic source is situated very close to the limb testing the limits of the helioseismic holography technique. The level contours of this source are

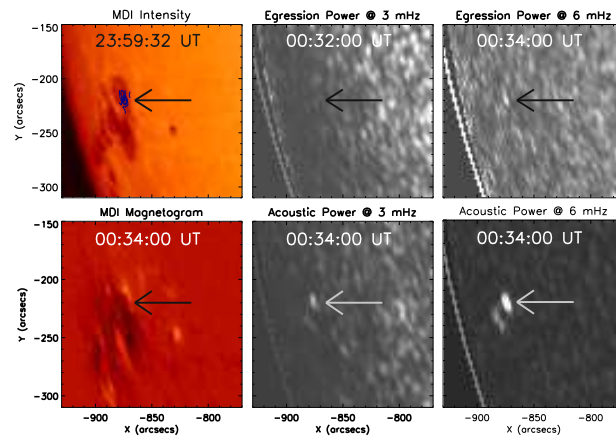


Figure 3.18: View of AR NOAA 10039 on July 23, 2002. Each panel shows specific times and wavelengths.

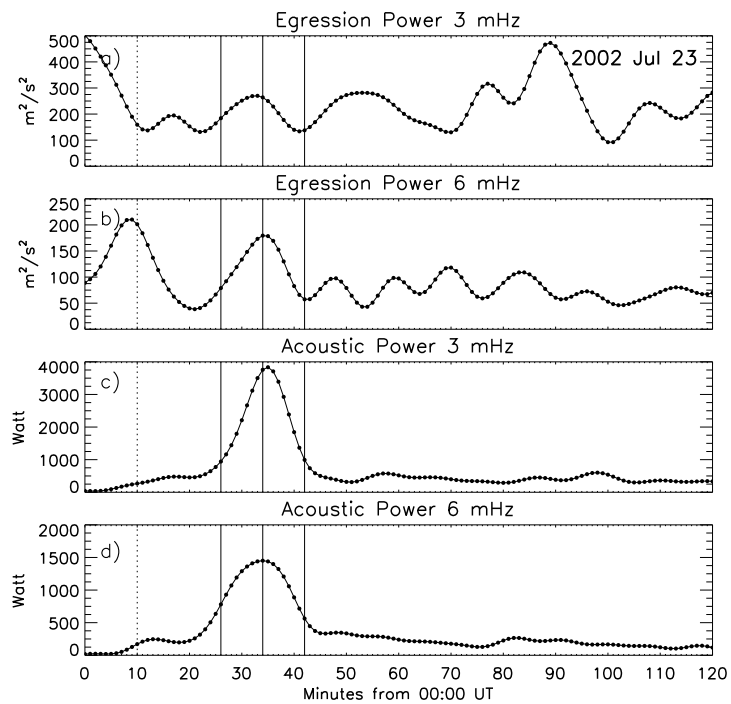


Figure 3.19: Same as 3.9, but for the single seismic source of July 23, 2002 solar flare. First vertical line, at 00:10 UT, represents the beginning of the real data from *MDI*.

over-plotted on the intensity continuum (first) frame, showing the position of the seismic source in the penumbra of the main spot. The seismic emission is coaligned with the magnetic neutral line, as seen in the first frame of Figure 3.18. It has a kernel structure and its area is about  $402 \text{ Mm}^2$ .

The egression power excess emission is clearly seen in the 6 mHz band and it is about twice the background noise. This signal is accompanied by signatures in the acoustic emissions, both at 3 and at 6 mHz (last two rows in Figure 3.18). The 3 mHz egression power time profile shows no significant signature at the time of the sun quake.

The vertical dashed line in all four frames situated at 00:10 UT, represents the start of the data. The first ten points of the graphs are artifacts resulting after applying the helioseismic holography technique. Taking into consideration that close to the limb we only analyse the line-of-sight component of the velocity, the acoustic noise is huge compromising our technique based on the perpendicular photospheric movement.

Figure 3.19, showing the temporal profiles of the egression and acoustic power, highlights the seismic activity peaking almost at the same minute as the integrated *GOES* flux maximum (the middle vertical line).

The estimated energy released into the photospheric level at 3 mHz is:  $2.51 \times 10^{27} \pm 5.92 \times 10^{25}$  ergs and at 6 mHz:  $1.33 \times 10^{27} \pm 4.76 \times 10^{24}$  ergs.

## 21 August 2002

This sun quake was generated by a weaker solar flare, an X1.0 type, but an impulsive one on August 21, 2002. Starting at 05:28 UT, it had its maximum after just six minutes and ended at 05:36 UT, two minutes after the maximum.

The active region that hosted this flare was AR NOAA 10069, a  $\beta\gamma\delta$ -type region situated at S08W58.

Figure 3.20 shows a view of this seismically active AR, having in the first column an *MDI* intensity continuum map and a magnetogram, followed by the egression power maps at 3 and 6 mHz in the first row and acoustic power maps at 3 and 6 mHz in the second row.

We can observe the seismic source located in the penumbra of the eastern spot. The seismic source has a double elongated structure with an area of  $120 \text{ Mm}^2$ .

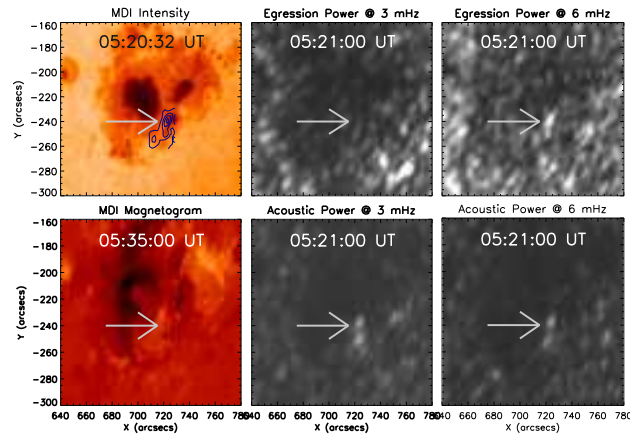


Figure 3.20: View of AR NOAA 10069 on August 21, 2002. Each panel shows specific times and wavelengths.

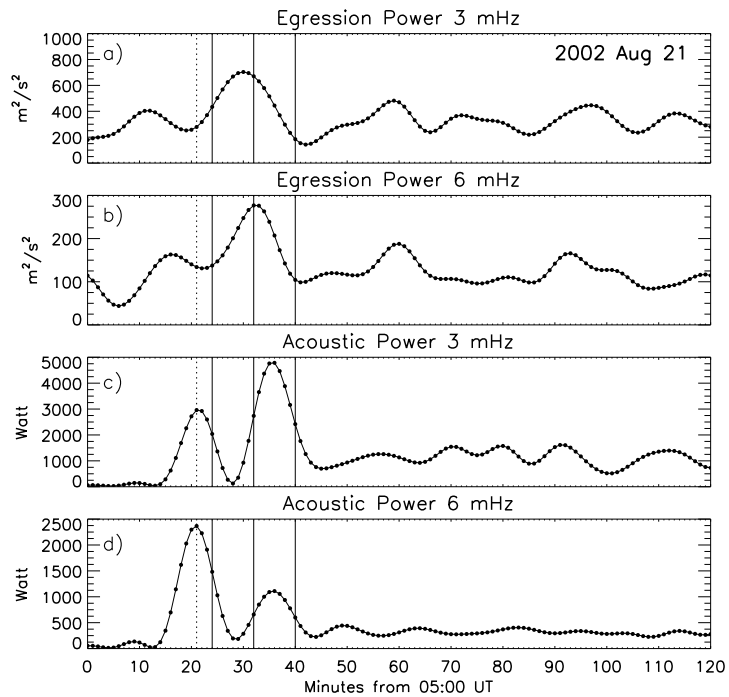


Figure 3.21: Same as 3.9, but for the seismic source of August 21, 2002 solar flare. First vertical line, at 05:21 UT, represents the beginning of the real data from *MDI*.

The sun quake associated with this flare started at 05:24 UT, peaked at 05:31 UT and ended at 05:39 UT.

The data set used for this flare was also corrupted, as indicated by the dashed vertical line situated at 05:21 UT in Figure 3.21. Therefore, disregarding the false maxima before this mark we can see the following: the sun quake can be seen both at 3 and at 6 mHz in the egression power time profiles, both of them being roughly double the background noise. They are also accompanied by signatures in the acoustic power profiles, with about five times the pre- and post-flare values, the excess emission at 3 mHz, and about three times at 6 mHz as seen in Figure 3.21.

The estimated energy released into the photospheric level at 3 mHz is:  $3.94 \times 10^{26} \pm 1.48 \times 10^{26}$  ergs and at 6 mHz:  $1.50 \times 10^{26} \pm 4.03 \times 10^{24}$  ergs.

## 23 October 2003

The sun quake generated by the X5.4 flare of October 23, 2003 is close to the end of the solar flare, rather than the general tendency of sun quakes being correlated with the ascending phase of the generating flare.

This flare started at 08:19 UT, peaked after 16 minutes and ended at 08:48 UT and was located above AR NOAA 10484, one of the most active AR of SC23. In October 23, 2003 this AR was situated at N04W01.

The sun quake started at 08:45 UT, peaked after two minutes and ended at 08:53 UT.

Figure 3.22 shows the main characteristics of this sun quake. In the first column of this figure we can see *MDI's* intensity continuum and magnetogram around the maximum of the seismic emission. The seismic contour levels are overplotted in the penumbra of the left spot of the AR.

The two egression power maps at 3 and 6 mHz follow in the top row of Figure 3.22, but only the 6 mHz snapshot shows the seismic transient. It has a rectangular shape and spreads over 39 Mm<sup>2</sup>. Just below we can find the corresponding acoustic power maps.

Figure 3.23 shows the time profiles of the sun quake as described by the egression and acoustic power. Taking into consideration that the AR was very close to the limb, the line-of-sight signal is diminished. The excess emission in the egression power is just about one and a half times the background noise, while all other time profiles show almost no significant activity associated with the seismic transient.

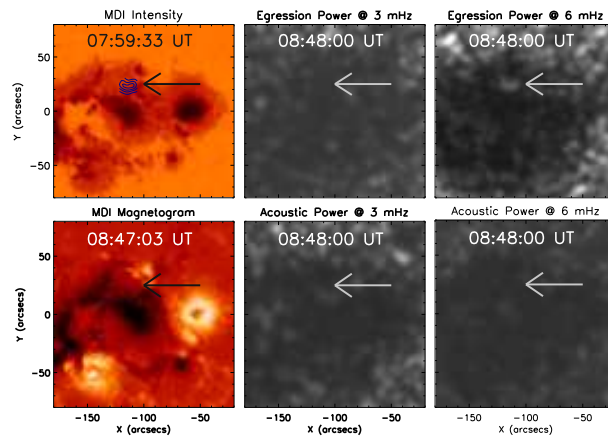


Figure 3.22: View of AR NOAA 10484 on October 23, 2003. Each panel shows specific times and wavelengths.

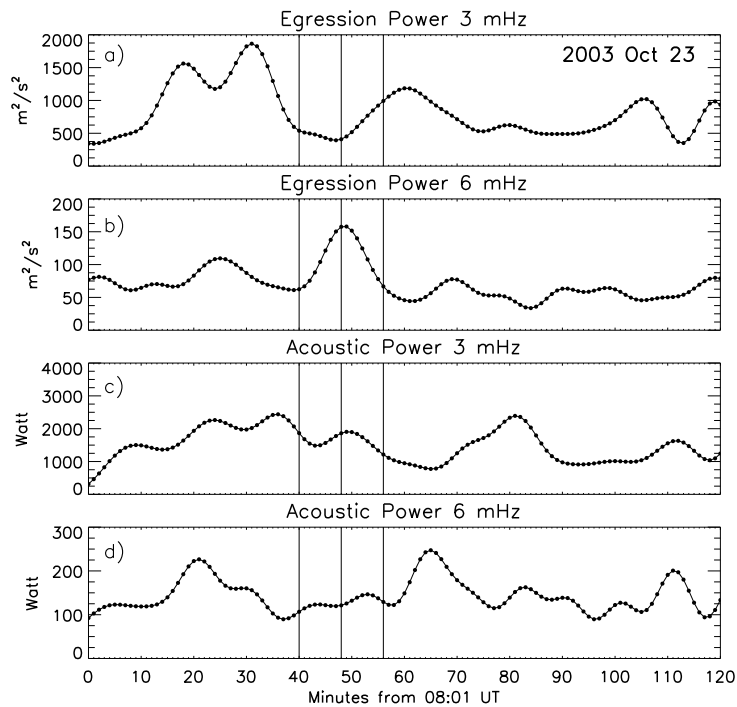


Figure 3.23: Same as 3.9, but for the seismic source of October 23, 2003 solar flare.

The estimated energy released into the photospheric level at 4 mHz is:  $2.14 \times 10^{26} \pm 6.28 \times 10^{25}$  ergs and at 6 mHz:  $5.53 \times 10^{25} \pm 1.67 \times 10^{24}$  ergs.

## 28 October 2003

The flares of October 28 and 29, 2003 include the famous ‘‘Halloween Flare’’ which has been highly analysed (Share et al., 2004). Two of the many flares of these dates were accompanied by seismic emissions. The sources were first detected by Donea and Lindsey (2005).

The acoustic response of the photosphere in October 28, 2003 was generated by the X17.2 flare, which started at 09:51 UT, had a very late peak at 11:10 UT and finished just 14 minutes after the maximum.

The source was seen in the NOAA 10486 AR, a  $\beta\gamma\delta$  region, situated at S16E04. It is one of the two known seismic sources to have signatures in two footprints. Both of them took place very close to the maximum of the integrated *GOES* flux emission.

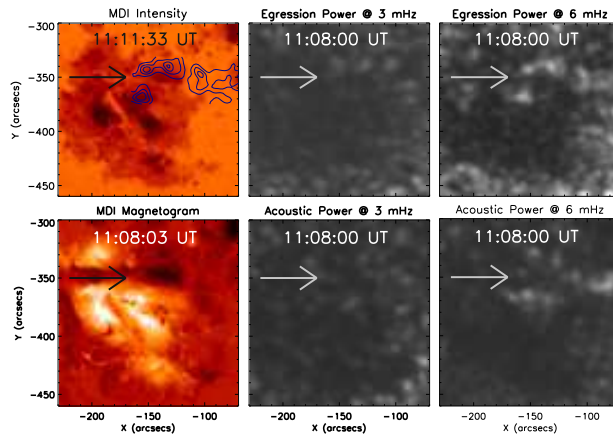


Figure 3.24: View of AR NOAA 10486 on October 28, 2003. Each panel shows specific times and wavelengths.

Figure 3.24 represents the usual configuration of the AR as the *MDI* intensity continuum and magnetograms, followed by the 3 and 6 mHz, egression and acoustic power signatures.

We can see the huge ribbon-like seismic emission spreading from the penumbra of the sunspot to the western plages surrounding this sunspot

in the third panel of the top row. It has an accompanying acoustic emission visible in the last panel of the bottom row. The total area covered by this sun quake is 1347 Mm<sup>2</sup>.

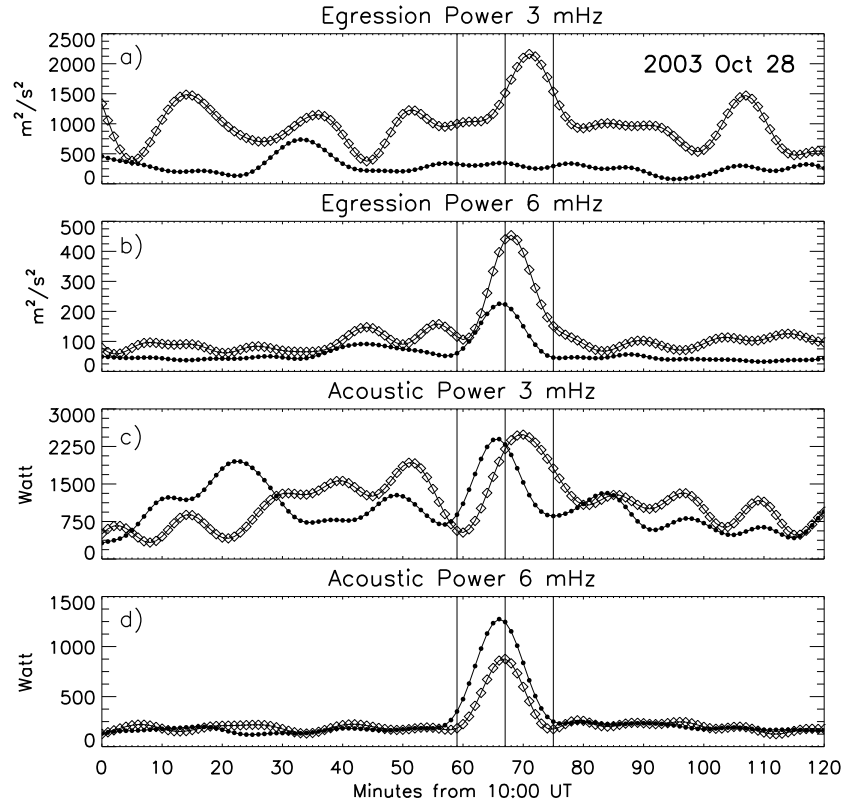


Figure 3.25: Same as 3.9, but for the seismic source of October 28, 2003 solar flare. The circled line represents the time evolution of the northern seismic source, while the diamond line represents the evolution of the southern seismic source as defined in Figure 3.24.

Figure 3.25 shows the time profiles of the two seismic sources plotted with circled line for the northern source and diamonds line for the southern one. The northern seismic source has no signature at 3 mHz, while the signal exceeds the background noise at 6 mHz by a factor two. The southern source is visible at 3 mHz too, although with about four minutes delayed, and has the 6 mHz power increasing almost five times compared with the pre- and post-flare values. The acoustic emissions show similar behaviour for the two sources, the difference being about five minutes difference at 3 mHz and one

minute at 6 mHz.

The estimated energy released into the photospheric level at 3 mHz is:  $2.14 \times 10^{26} \pm 6.28 \times 10^{25}$  ergs and at 6 mHz:  $5.53 \times 10^{25} \pm 1.67 \times 10^{24}$  ergs.

## 29 October 2003

This seismic source was, also, first detected by [Donea and Lindsey \(2005\)](#). They have extensively described the behaviour of the acoustic emission. We will just summarize its properties here. The solar flare of October 29, 2003 has been classified as an X10 type and it occurred in the NOAA AR 10486, localized at S17W10.

The egression power snapshot from Figure 3.26 shows a single compact signature spreading over  $183 \text{ Mm}^2$ . This acoustic emission came from the eastern outer boundary of the penumbra encompassing the sunspot.

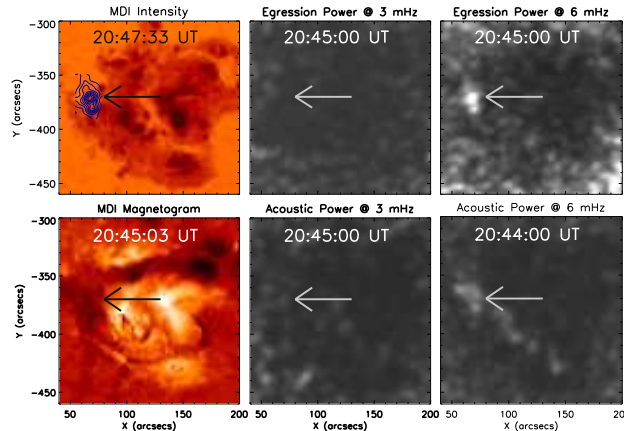


Figure 3.26: View of AR NOAA 10486 on October 29, 2003. Each panel shows specific times and wavelengths.

The flare times as registered by *GOES* were: beginning: 20:37 UT, maximum: 20:49 UT and ending: 21:01 UT. The sun quake evolved around the maximum of the flare, that is: beginning: 20:35 UT, maximum: 20:43 UT and ending: 20:50 UT.

As [Donea and Lindsey \(2005\)](#) considered, it is possible that the increase in intensity at the onset of the flare is considerably more sudden than the linear rise over the two minutes suggested by the time plot.

Figure 3.26 shows the general view of the hosting AR with the *MDI* intensity continuum map and the magnetogram on the first row, followed by the 3 and 6 mHz egression and acoustic power. The egression power signature at 20:45 UT is obvious in the third panel of the first row and is also located in the eastern region of the penumbra (as shown by the overplotted contour levels), coaligned with the magnetic neutral line.

The acoustic signature is wider with a stronger conspicuous shape at the same location as the egression power maximum.

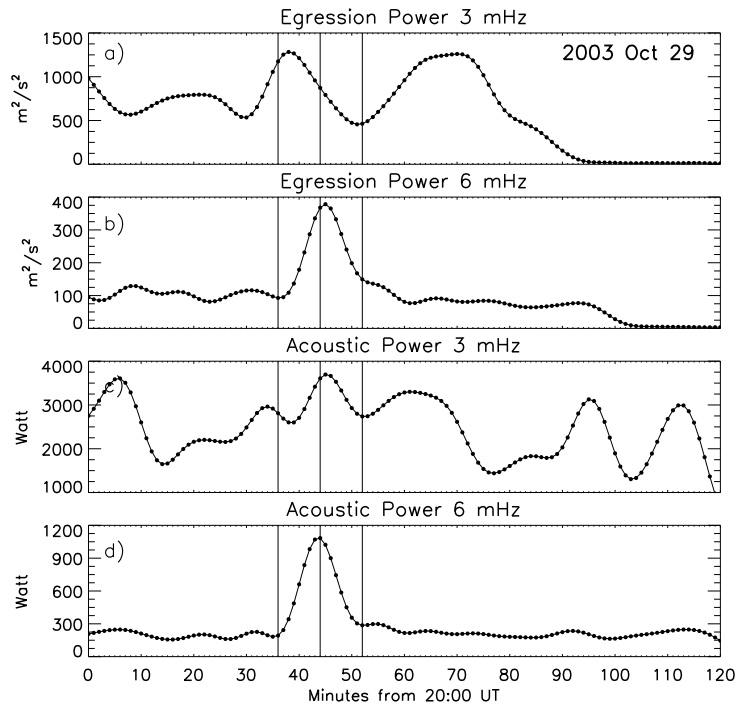


Figure 3.27: Same as 3.9, but for the seismic source of October 29, 2003 solar flare.

Figure 3.27 shows the temporal profiles of the 3 and 6 mHz egression and acoustic power. Although the 3 mHz profiles do not show any significant activity during the flare, the 6 mHz plots show the excess emissions to be about four times stronger than the background level for the egression and acoustic power.

The estimated energy released into the photospheric level at 3 mHz is:  $5.12 \times 10^{26} \pm 1.58 \times 10^{26}$  ergs and at 6 mHz:  $2.57 \times 10^{26} \pm 1.70 \times 10^{25}$

ergs.

## 16 July 2004

The seismic source generated by the X3.6-type solar flare from July 16, 2004 is one of the most interesting sources detected to date. Located in AR NOAA 10649 (S10E26), the flare started at 13:49 UT, had its maximum at 13:55 UT and ended at 14:01 UT.

We reported the discovery of this seismic source for the first time in [Donea and Lindsey \(2005\)](#) and [Beşliu et al. \(2005b\)](#) and we have also studied it in [Beşliu-Ionescu et al. \(2007a,b,c\)](#). The acoustic source at 6 mHz is almost four times more intense than the acoustic source produced by the X2.6 flare of July 9, 1996 (reported as the first acoustically active flare). However, the seismic source at 3 mHz, although very hard to distinguish against the 5-minute oscillation background in the maps, had only 15% of the total acoustic power of the July 9, 1996 sun quake. Seismic images of this source were displayed at [users.monash.edu.au/~dionescu](http://users.monash.edu.au/~dionescu). Consequently, [Kosovichev \(2006\)](#) plotted the time-distance diagrams of this event showing that the expanding seismic waves increase their speed with distance from the centre of AR10649. Interestingly, although the flare produced a much weaker soft X-ray emission, it produced higher amplitude seismic waves than the X17 super flare of October 28, 2003.

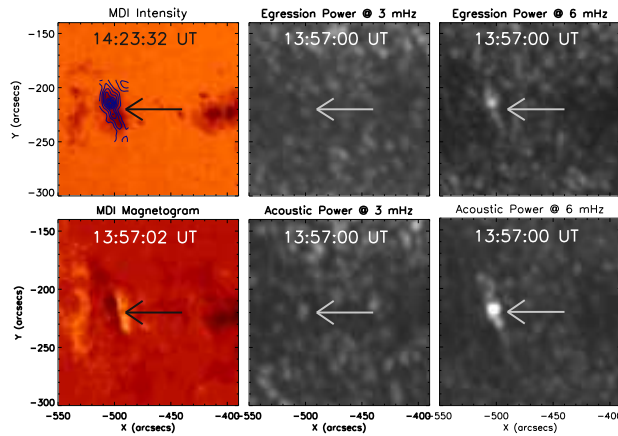


Figure 3.28: View of AR 10649 on July 16, 2004. Each panel shows specific times and wavelengths.

Figure 3.28 shows a general view of this  $\beta\gamma\delta$ -type AR10649. The observation times are specified in each frame. In the first column we can see the *MDI* intensity continuum map and magnetogram showing that the seismic emission is located in the penumbra of the dominant spot and is oriented along the magnetic neutral line (NS). The egression power map shows a compact seismic source acting at 6 mHz at its maximum and a corresponding acoustic signature to which it coincides both spatially and temporally as seen in the last column of Figure 3.28. This sun quake has an inclined kernel shape and its area is about 284 Mm<sup>2</sup>.

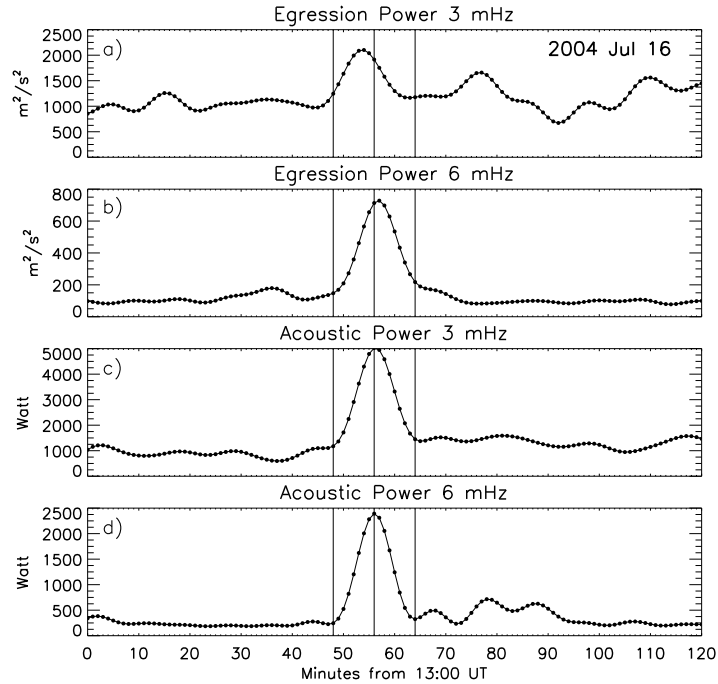


Figure 3.29: Same as Figure 3.3 for the seismic source of July 16, 2004.

Time series of the 3 and 6 mHz egression and acoustic power are shown in Figure 3.29. The excess emission is extremely visible in all the panels, with huge increases of almost eight times for the egression power at 6 mHz and about five times for the acoustic emissions.

The estimated energy released into the photospheric level at 3 mHz is:  $9.51 \times 10^{26} \pm 7.89 \times 10^{25}$  ergs and at 6 mHz:  $5.85 \times 10^{26} \pm 2.65 \times 10^{24}$  ergs.

## 13 August 2004

AR NOAA 10656 appeared on the solar surface on August 7, 2004 at S12E55 as an  $\alpha$  sunspot. During one week the region has continued to increase in magnetic complexity and evolved to a  $\beta\gamma\delta$  type. From August, 8 to 16 it produced 2 X-class, 36 M-class and more than 150 C-type flares.

This highly active region produced three sun quakes. The first sun quake was generated by the X1.0 solar flare on August 13, 2004 which started at 18:07 UT, peaked five minutes later and ended at 18:15 UT.

Figure 3.30 shows the general view of AR NOAA 10656 with the usual *MDI* intensity continuum map and magnetogram, the 3 and 6 mHz egression and acoustic power snapshots.

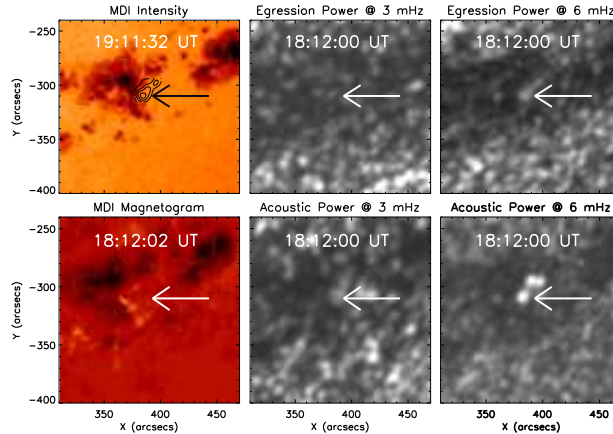


Figure 3.30: General description of AR 10656 on August 13, 2004.

Its associated seismic emission started at the same time as the flare, peaked two minutes before the maximum of the flare and ended at 18:16 UT.

The seismic emission is visible in the 6 mHz egression power map in the third panel of the top row and is located in the western penumbra of the central spot in the positive plages.

This sun quake is shaped as a thin rectangle and has an area of about  $115 \text{ Mm}^2$ . The corresponding acoustic signature is visible on the bottom row, last panel.

Figure 3.31 shows the time profiles of the egression and power at 3 and 6 mHz. The first four minutes of data were corrupted (before the first vertical line). The excess emission is visible in all the panel with peaks as high as six

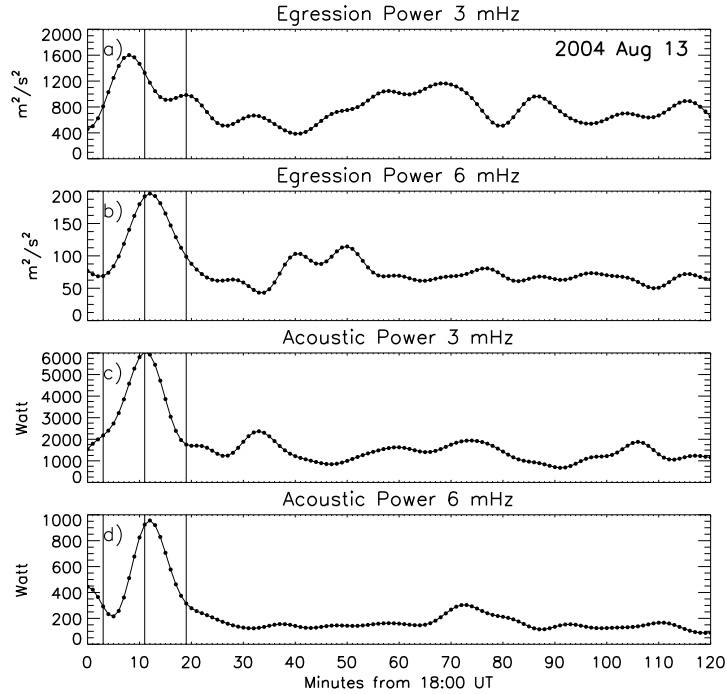


Figure 3.31: Same as 3.9, but for the seismic source of August 13, 2004 solar flare. First vertical line, at 18:04 UT, represents the beginning of the real data from *MDI*.

times (acoustic power) the pre- and post-flare values. The egression power at 6 mHz exceeds the background emission by a factor two.

The estimated energy released into the photospheric level at 3 mHz is:  $4.20 \times 10^{26} \pm 3.00 \times 10^{25}$  ergs and at 6 mHz:  $1.02 \times 10^{26} \pm 1.91 \times 10^{24}$  ergs.

## 14 August 2004

On Aug 14th the region situated at S13 W36 was characterised by a strong  $\delta$  configuration in the middle of the sunspot and a general configuration of  $\beta\gamma\delta$  type. At 05:36 UT an M-class flare occurred, peaked at 05:44 UT and had a maximum at 05:52 UT (as given by *GOES12*) with a X-ray flux of  $3.8 \times 10^{-2}$ . This M 7.4 type solar flare produced seismic emission. To this date, this is the second smallest flare class generating an acoustic source.

Figure 3.32 shows the general view of AR NOAA 10656 with the usual

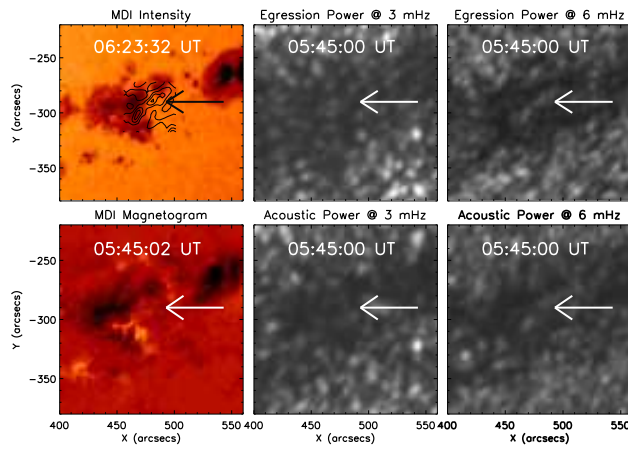


Figure 3.32: General description of AR 10656 on August 14, 2004.

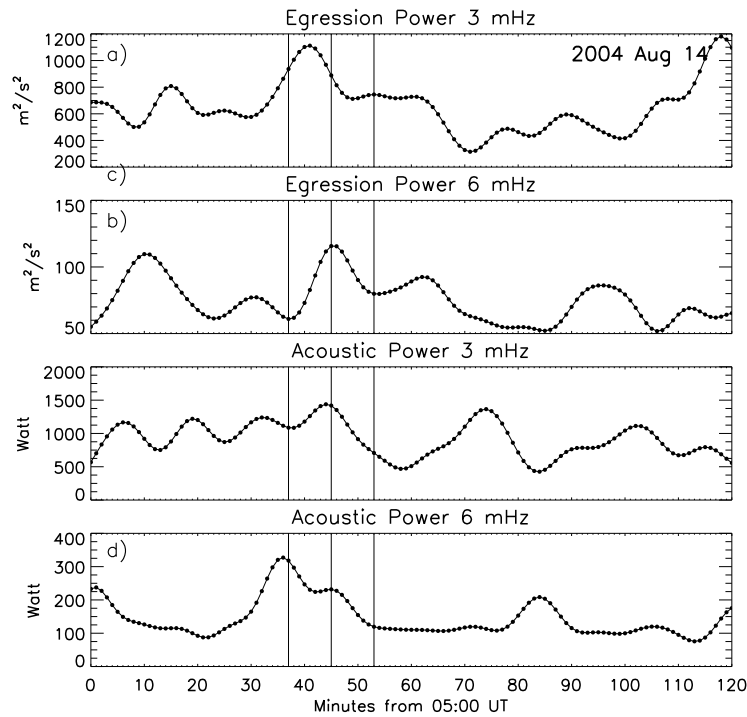


Figure 3.33: Same as 3.9, but for the seismic source of August 14, 2004 solar flare.

MDI intensity continuum map and magnetogram and 3 and 6 mHz egression and acoustic power maps. The seismic emission is visible in the 6 mHz egression power map spreading from the north-eastern penumbra of the main spot to the south-western penumbra of the western side spot.

This seismic signature is kernel structured and spreads over  $\sim 194 \text{ Mm}^2$ . The corresponding acoustic signature is visible on the bottom row, last panel.

Figure 3.33 shows the time profiles of the egression and power at 3 and 6 mHz. The excess emission is visible in all the panel as local maxima compared with the pre- and post-flare values.

The estimated energy released into the photospheric level at 3 mHz is:  $4.65 \times 10^{26} \pm 1.43 \times 10^{26}$  ergs and at 6 mHz:  $5.91 \times 10^{25} \pm 9.62 \times 10^{24}$  ergs.

## 15 August 2004

This sun quake was generated by an M9.4 type solar flare. It was a short flare that evolved over nine minutes starting at 12:34 UT, peaking at 12:41 UT and ending two minutes later.

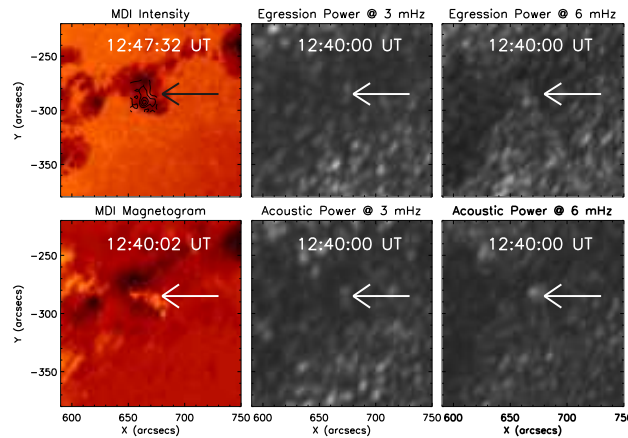


Figure 3.34: General description of AR 10656 on August 15, 2004.

We would like to remind the reader that the same active region produced two more sun quakes within 48 hours: one generated by the X 1.0-type from August 13 and the other generated by the M 7.4-type solar flare from August 14, 2004.

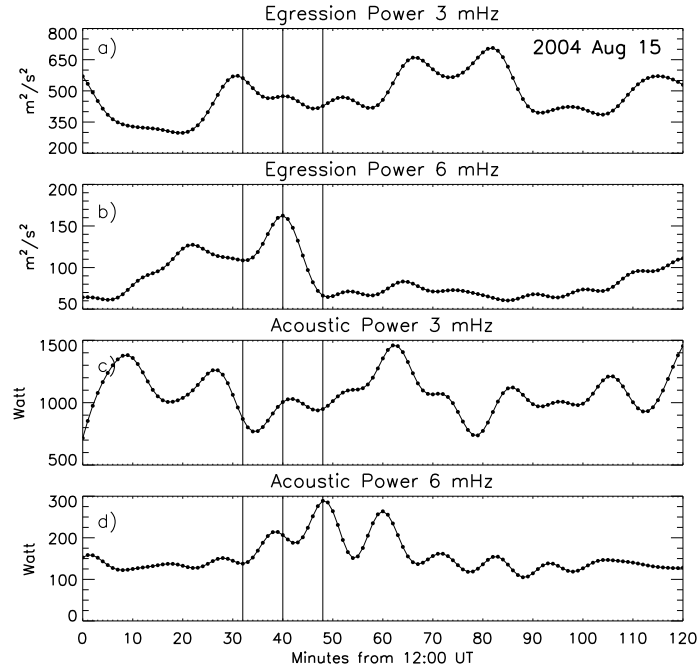


Figure 3.35: Same as 3.9 but for the seismic source of August 15, 2004 solar flare.

Figure 3.34 shows the general description of the AR NOAA 10656 with the same structure as Figure 3.32. We just underline here the presence of the seismic source in the penumbral central region of this AR. The sun quake has an inclined kernel structure with an area  $\sim 435 \text{ Mm}^2$ . The 3 mHz signature is visible both in the egression and acoustic power.

Figure 3.35 shows time profiles of the egression and power at 3 and 6 mHz. The excess emission is visible in the second panel showing the egression power profile at 6 mHz, but no other correlated emissions are noticeable.

The estimated energy released into the photospheric level at 4 mHz is:  $6.76 \times 10^{26} \pm 2.10 \times 10^{26}$  ergs and at 6 mHz:  $3.01 \times 10^{26} \pm 5.46 \times 10^{24}$  ergs.

## 15 January 2005

This sun quake was extensively studied by [Moradi et al. \(2007\)](#). I will remind the reader of some of the main characteristics of this emission.

Very close to the end of the descending phase of SC23 very few active regions were still producing flares. One of these was NOAA AR10720 with plenty of activity, counting five X-type solar flares and almost 20 M-type flares. Unfortunately, just this X1.2 flare was fully covered with *MDI* data. On January 15, 2005 at 00:22 UT the flare started. It peaked at 00:43 UT and ended 19 minutes later. At this date the AR10720 was a  $\beta\delta$ -type region situated at N13W04.

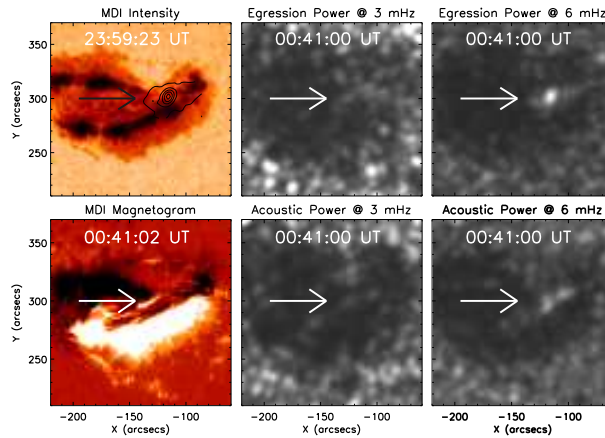


Figure 3.36: General description of AR 10720 on January 15, 2005. First row: first panel is a

The seismic emission is very well time correlated with the flare, both having the maximum around 00:42 UT.

Figure 3.36 shows the general description of the flaring AR with the *MDI* intensity continuum followed by the two egression power snapshots centred at 3 and 6 mHz and having on the second row the magnetogram, followed by the corresponding acoustic power snapshots.

The seismic signature is shaped as a dove, with a central very bright kernel and two fainter kernels situated by each side. Its area is about 530  $\text{Mm}^2$ .

Figure 3.37 shows the time profiles of the egression and power at 3 and 6 mHz. The excess emission is visible in all the panels with power excess of a factor of at least two compared with the pre- and post-flare values.

The estimated energy released into the photospheric level at 3 mHz is:  $2.20 \times 10^{27} \pm 2.72 \times 10^{25}$  ergs and at 6 mHz:  $1.02 \times 10^{27} \pm 2.72 \times 10^{25}$  ergs.

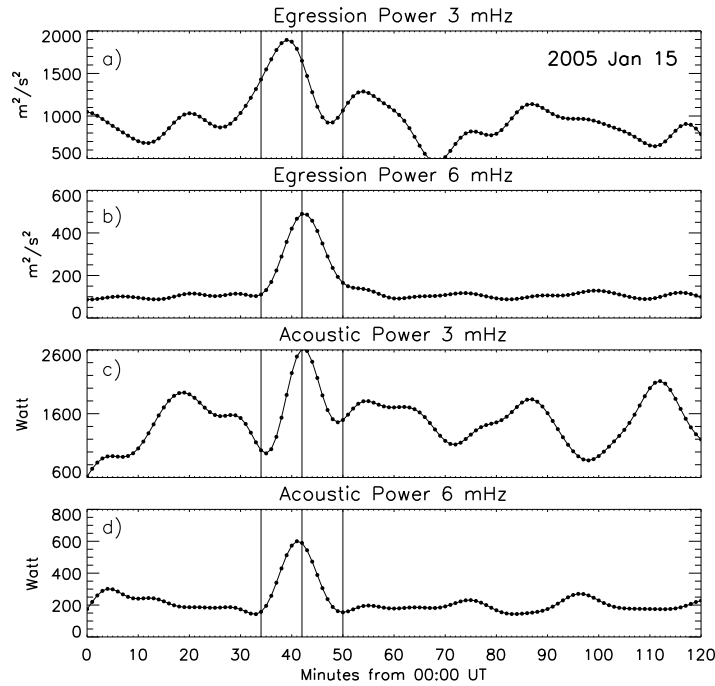


Figure 3.37: Same as 3.9, but for the single seismic source of January 15, 2005 solar flare.

## 13 September 2005

On September 13, 2005 an X1.5 flare erupted above  $\beta\gamma\delta$  AR NOAA 10808 situated at S11E17. The integrated *GOES* flux started to increase at 19:19 UT, reached the peak at 19:27 and ended one and a half hour later. Concomitant with this fast rising ascending phase we discovered a sun quake that had its maximum at 19:22 UT.

Figure 3.38 shows the AR in an *MDI* intensity continuum and a magnetogram on the first column. Overplotted on the intensity continuum are the contour levels of the egression power at the maximum of its emission.

On the first row of Figure 3.38 we can also see the two egression power snapshots at 3 and 6 mHz. The seismic signature at 3 mHz looks more like noise, but at 6 mHz we can see a torsioned snake-like shape in the plages of the AR. The area of this sun quake is about  $199 \text{ Mm}^2$ . The last two frames on the second row show the acoustic emissions at 3 and 6 mHz at the time of the maximum excess emission in the egression power.

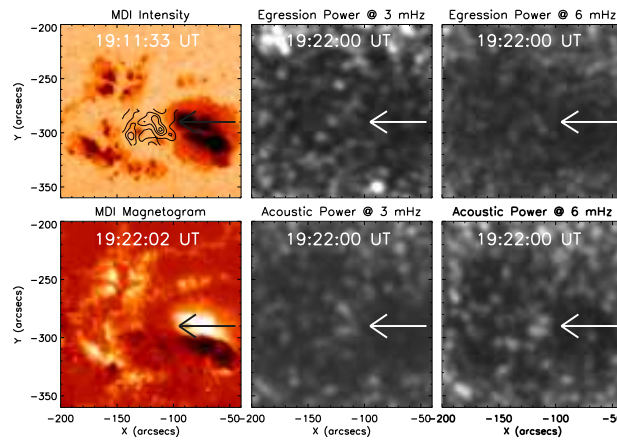


Figure 3.38: General description of AR 10808 on September 13, 2005.

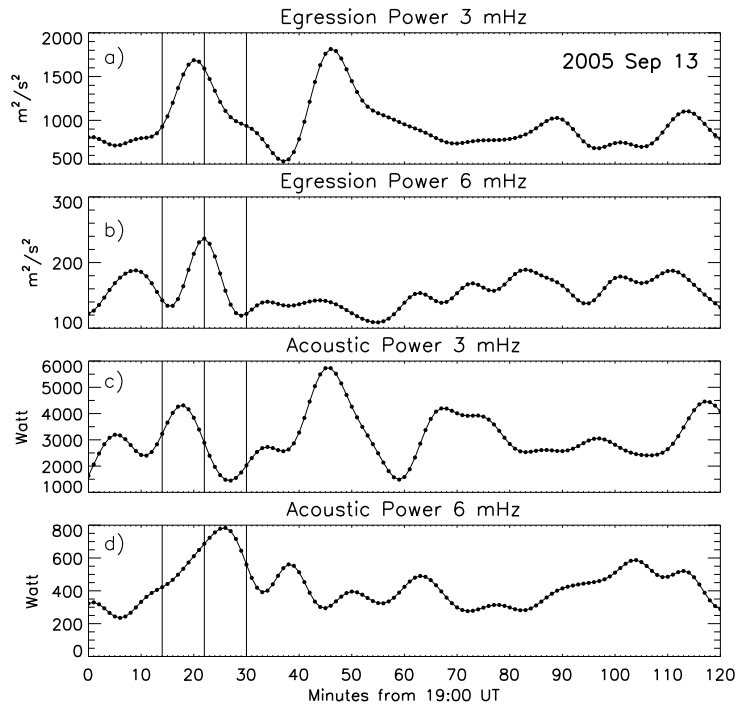


Figure 3.39: Same as but for the single seismic source of September 13, 2005 solar flare.

Figure 3.39 shows the temporal profiles of the egression and acoustic power integrated over the sun quake's area. Although the excess emission in the egression power at 6 mHz exceeded only by one and a half times the background noise, there is a good correlation in between all temporal profiles.

The estimated energy released into the photospheric level at 3 mHz is:  $1.11 \times 10^{27} \pm 7.89 \times 10^{26}$  ergs and at 6 mHz:  $1.15 \times 10^{26} \pm 2.65 \times 10^{25}$  ergs.

## 2 December 2005

One of the most powerful sun quakes was generated by the M7.8-type solar flare of December 2, 2005. It is one of the most puzzling phenomena reported first by [Beşliu-Ionescu et al. \(2006c\)](#).

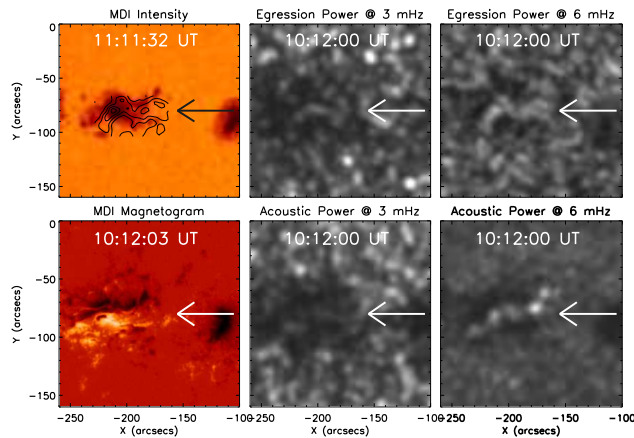


Figure 3.40: General description of AR 10826 on December 2, 2005.

This flare was an impulsive one, lasted for 20 minutes, starting at 10:05 UT, had its maximum at 10:12 UT and ended at 10:25 UT. Hosted by the  $\alpha\beta\gamma$  10826 AR (S02E08) the sun quake lasted for 14 minutes.

Figure 3.40 displays the structure of the AR 10826 represented by *MDI* intensity continuum map and magnetogram, and the 3 and 6 mHz egression and acoustic power maps.

This seismic source is spread over a significant part of the AR, mainly in its penumbra, but also covering the central umbra of the spot. This is a very widely spread sun quake, covering an area of  $659 \text{ Mm}^2$ , and shaped as a sinusoidal function.

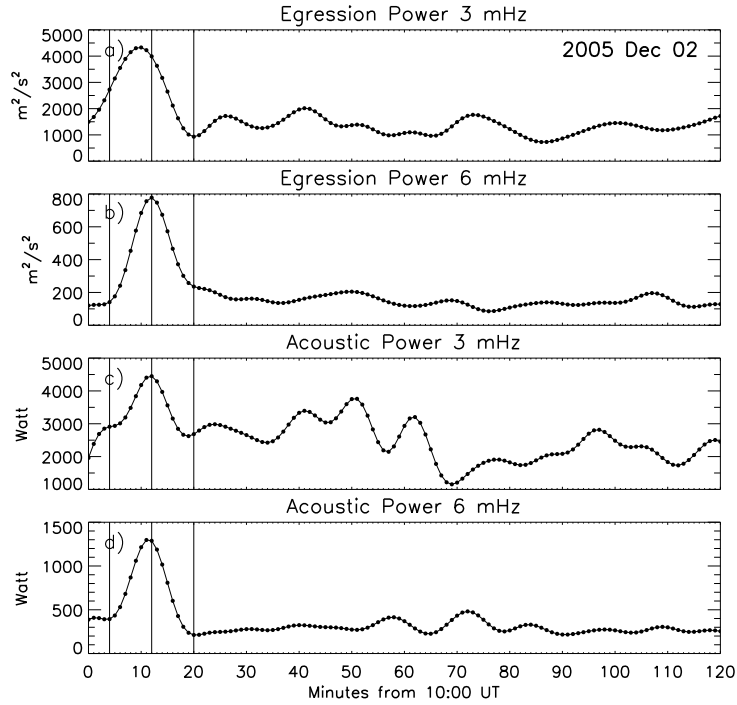


Figure 3.41: Same as but for the single seismic source of December 2, 2005 solar flare.

Figure 3.41 shows the temporal profiles of the egression and acoustic power having visible peaks in all panels very well correlated with the maximum of the X-ray flux.

The estimated energy released into the photospheric level at 3 mHz is:  $2.54 \times 10^{28} \pm 4.49 \times 10^{27}$  ergs and at 6 mHz:  $5.72 \times 10^{27} \pm 4.43 \times 10^{26}$  ergs.

## 3.2 WEB Database

One of the first outcomes of our work was a detailed database, available on-line, to show the solar flares from SC23 and many of their properties. Figure 3.42 shows a caption from the website database. The entire database is available at

<http://users.monash.edu.au/~dionescu/sunquakes/sunquakes.html>.

Each row in this table represents one flare with some characteristics such

as: on the first three columns the date (year, months, date), the fourth column the NOAA number of the AR, the next column states the type of the AR, the next three columns represent the location of the AR and the Carrington coordinates of the AR's centre.

Columns nine, ten, eleven represent the flare times (beginning, peak and end as defined by the integrated flux from *GOES*). In the next column we can see the type of the solar flare.

The largest and most important column is generically named "Observation". This is where we defined the sun quake, or the inactivity of the flare, or the lack of data to analyse. Where we found the solar flare to have seismic activity, the note is "SQ" and it represents a link to another page describing some basic properties of the sun quake.

The sun quake descriptive page is comprised of six figures: 1. a general description of the hosting AR – an intensity continuum map, a magnetogram and two Dopplegrams before and at the seismic maximum emission; 2. Dopp-lergram differences – two Dopplergram differences obtained by subtracting the previous minute map from the current map, at the time of the flare maximum and, on the second row, the two maximum emissions of the egression power at 3 and 6 mHz; 3. acoustic power maps – the acoustic maps inte-grated over the entire period included in the helioseismic holography analysis (usually four hours) on the first row and on the second row, the acoustic emis-sion maps at the maximum of the emission; 4. 6 mHz egression power maps at times specified above each frame to show the seismic source's evolution; 5. time series – the time profiles of the 3 and 6 mHz egression power and acoustic power emissions integrated over the sun quake area; 6. an animated gif to show the formation of the sun quake as seen from the egression power maps.

This WEB database will be continuously updated with the latest results obtained from our research.

### 3.3 Conclusions

The concerted work in discovering and analysing the seismic properties of flares presents many tantalizing clues to their physical nature.

A first observation would be that the sun quakes are not such a rare phenomenon as previously thought. They seem to cover quite well solar cycle 23, if we take into consideration that the lack of sun quakes during

1997–1999 is due to the absence of data coverage from *MDI*. *HMI* should provide us a better data coverage of SC24 and hopefully will help us discover a possible relationship between the solar cycle and the ignition of sun quakes.

We also note that there is no obvious relationship between the type of the hosting active region and the occurrence of sun quakes, although there is a preference towards the  $\beta\gamma\delta$ -type (75% of seismic emissions evolved in this type of region). This preference might be explained by the complex magnetic configuration of the flaring region. The complexity of the magnetic field definitely plays an important role in triggering the acoustic source.

All sun quakes appear in some connection with the magnetic neutral line, usually taking the same direction and being situated near by. There might be a connection between the occurrence of the sun quakes and the inclination of the magnetic field lines, but to sustain such a conclusion one would need 3D magnetograms covering the entire duration of the flare. Again, *HMI* should be able to provide us that information too.

With only one exception, all the sun quakes are situated in the penumbra of the flaring region. The exception is the seismic emission associated with the July 15, 2002 flare, where its location is coincident with the presence of the white light. All other sun quakes are also co-aligned with the white light excess emission (further details in Chapter 4), but in the July 15, 2002 flare, the white light emission passed over the entire active region.

It is now clear that the conclusion from [Beşliu et al. \(2005a\)](#); [Beşliu-Ionescu et al. \(2006c\)](#); [Donea et al. \(2006b\)](#); [Moradi et al. \(2007\)](#) referring to the amount of energy required to ignite a sun quake being a very small fraction of the energy released during the flare, is valid for all the sun quakes. Therefore, the closing question of this chapter will remain: why do most of the flares releasing more than enough energy to ignite a seismic response, remain acoustically inactive?

Year	Month	Day	AR	Type of AR	Position	L0	B0	Begin (UT)	Max (UT)	End (UT)	Type	Observations	Proton Event	White Flare	SQ Begin (UT)	SQ Max (UT)	SQ End (UT)	Seismic Energies 3 mHz (erg)	Seismic Energies 6 mHz (erg)	GOES Xray (J/m2)
1996	7	9	7978	$\beta\gamma\delta$	S10W38 (574',-213')	249	-10.5	09:01	09:12	09:49	X 2.6	First sunquake discovered by its acoustic source detected	-		09:01	09:13	09:19	7.50E+027	8.90E+026	7.30E-002
1997	11	4	8100	$\beta\gamma\delta$	S20W40 (572',-370')	-	-	05:52	05:58	06:02	X 2.1	No data	X		-	-	-	-	-	5.60E-002
2001	9	9	9608	$\beta\gamma$	S28E20 (-291',-513')	106	-28	20:40	20:45	20:48	M 9.5	SQ	-	X	20:44	20:46	20:54	1.11E+027	2.05+26	0
2001	9	24	9632	$\beta\gamma\delta$	S18E18 (-278',-394')	273	-19	09:32	10:38	11:09	X 2.6	SQ	X		09:35	09:37	09:45	0	5.97E+025	6.30E-001
2001	10	19	9661	$\beta\gamma\delta$	N16W37 (548',190')	-	-	00:47	01:05	01:13	X 1.6	Not enough data	-		-	-	-	-	-	1.20E-001
2002	7	3	10017	$\beta\gamma$	S18W65 (815',-313')	-	-	02:08	02:13	02:16	X 1.5	At the limb	-		-	-	-	-	-	4.10E-002
2002	8	3	10039	$\beta\gamma$	S15W84 (907',-253')	-	-	18:59	19:07	19:11	X 1.0	At the limb	-		-	-	-	-	-	3.30E-002
2002	8	21	10069	$\beta\gamma\delta$	S08W58 (795',-190')	303	-8	05:28	05:34	05:36	X 1.0	SQ	-		05:24	05:31	05:39	2.83E+026	7.70E+025	2.30E-002
2002	8	24	10069	$\beta\gamma\delta$	S08W91 (935',-128')	-	-	00:49	01:12	01:31	X 3.1	At the limb	X		-	-	-	-	-	4.60E-001
2003	10	26	10484	$\beta\gamma\delta$	N04W41 (620',4')	356	3	17:21	18:19	19:21	X 1.2	In progress	X		-	-	-	-	-	6.30E-001
2003	10	28	10486	$\beta\gamma\delta$	S16E04 (-63',-335')	288	-19	09:51	11:10	11:24	X 17.2	SQ discovered by A.C. Donnea & C. Lindsey	X		11:00/11:07/11:12/11:11	11:12/11:11	11:12/11:11	1.00E+027	9.40E+026	1.80E+000
2003	10	29	10486	$\beta\gamma\delta$	S17W10 (157',-348')	288	-19	20:37	20:49	21:01	X 10	SQ discovered by A.C. Donnea & C. Lindsey	-		20:35	20:43	20:50	1.10E+027	2.70E+026	8.70E-001
2003	11	2	10486	$\beta\gamma\delta$	N08W69 (874',106')	-	-	17:03	17:25	17:39	X 8.3	At the limb	-		-	-	-	-	-	9.10E-001
2003	11	3	10488	$\beta\gamma\delta$	N08W82 (926',121')	-	-	01:09	01:30	01:45	X 2.7	At the limb	-		-	-	-	-	-	3.60E-001
2004	7	16	10649	$\beta\gamma\delta$	S10E26 (-409',-230')	44	-10	10:32	10:41	10:46	X 1.1	Negative	-		-	-	-	-	-	4.00E-002
2004	7	16	10649	$\beta\gamma\delta$	S10E26 (-409',-230')	44	-10	13:49	13:55	14:01	X 3.6	SQ	-		13:48	13:56	14:01	7.31E+026	3.06E+025	1.40E-001
2005	1	15	10720	$\beta\delta$	N13W04 (66',297')	180	13	00:22	00:43	01:02	X 1.2	SQ	-	X	00:33	00:42	00:47	1.78E+027	9.50E+026	1.20E-001

Figure 3.42: Caption of the WEB database.



## Chapter 4

# Multiwavelength Analysis of Seismic Sources Generated by Flares

The discovery of a significant number of seismic sources with a very interesting temporal and morphological behaviour leads us to the next step of our study: the multiwavelength analysis of these events. Investigation of sun quakes provides new insight into the physics of solar flares and new means for local helioseismic diagnostics. Previously, our analysis was mainly based on identifying significant correlations (such as temporal, spatial relationships) between the seismic transients located in the photosphere and other flare-related spectral signatures situated above the solar surface (in the chromosphere or corona).

For example, we found acoustic signatures spatially and temporally coincident with impulsively changing magnetic signatures, suggesting that suddenly modifying magnetic forces might have contributed to the seismic emission. Of course, we need to understand possible effects of an inversion of the NiI 6768 Å line as a result of heating of the solar atmosphere by high-energy particles. However, [Sudol and Harvey \(2005\)](#) likewise found transient magnetic signatures in flaring photospheres using *GONG* data in the same NiI line.

We have also found that the fraction of energy emitted into the subphotosphere as seismic waves remained a small fraction of the total energy released in the flare. The persistence of a sudden, co-spatial white-light signature in flares where no energetic protons were evident was consistent with acoustic

emission driven by back-warming of the low photosphere by radiation from a heated overlying chromosphere. Clearly, the  $H\alpha$  ribbons occurring during the Halloween flares at the sun quake site (Donea and Lindsey, 2005) is another sign that the multiwavelength analysis of the seismic solar flares can give us more clues about these interesting and powerful events (Beşliu-Ionescu et al., 2007a,c,d).

The following sections contain the analysis of the atmosphere response to a seismically active flare. We will analyse the following:

- the intensity continuum images of seismic sources;
- the Doppler signatures in LOS velocities of the photosphere during a highly seismic event;
- properties of seismic ripples on the solar surface;
- temporal behaviour of photospheric magnetic fields during flares;
- observation of the UV at 1600Å emission during flares using data from *TRACE* satellite;
- NaDI and  $H\alpha$  emission lines of significant seismic transients;
- Going upwards in the atmosphere, the Fe lines measured by *TRACE* and *SOHO-EIT* have covered seven flares with seismicity in the 171Å and 195Å wavelengths.

## 4.1 Results of the Analysis of Intensity Continuum Data

In this section we study properties of the continuum emission at the photospheric level observed during the evolution of seismic transients.

Recent discoveries show that solar flares are accompanied by a white light (WL) excess emission (Jess et al., 2008; Hudson et al., 2006). However, current observations made with *Hinode* (Wang, 2009) suggest that this is not always the case. We want to emphasise here that all seismically active flares with a good data coverage in the intensity continuum, had indeed significant white light emissions spatially and temporally correlated with the seismic transient. White light flares are thought to have a strong relationship with

the non-thermal processes producing hard X-rays and EUV (Hudson, 1972) indicating that the mechanism responsible for their occurrence must be the thick-target model (Svestka, 1970). Kosovichev and Zharkova (1998) linked the thick-target model of flare generation with the process of solar quake formation. The high-energy electrons, accelerated during the flare high in the corona, produce hard X-ray fluxes in the lower atmosphere and generate downward propagating chromospheric shocks which hit the photosphere. The shocks that have reached the photospheric level generate in turn the seismic waves and the overall hydrodynamic response (e.g. Kostiuk and Pikelner, 1975; Kosovichev, 1986).

Figures 4.1 to 4.6 show the results (mainly maps) of our data reduction of all existing intensity continuum observations associated with acoustically active flares.

Each row in these figures represents a sun quake with its occurrence date printed above the left frame. The first frame in each row represents an intensity continuum image of the active region that hosted the seismic transient. The second and third frame represent intensity continuum difference maps showing the location of the white light excess emission. Intensity continuum differences are maps of intensity values with the previous minute values subtracted.

Intensity continuum differences, as well as all differences maps used from here on, are the result of two consecutive frames subtracted one from the other, choosing the set up of the process in order to highlight the existing transient. The times showed above such an image are usually centre of the time interval where seconds are specified or simply xx:yy:30 (where yy minutes are read from the first frame).

The fourth frame in each row shows the egression power map for the time where the seismic source generated from the flare had its maximum strength. The observational times are shown above each frame. Arrows point to the seismic source, as seen in the egression power maps. The *SOHO/MDI* images were reduced and centred on the active region that hosted the solar flares.

We refer the reader to Tables 3.1 and 3.2 in Chapter 3 listing the detected seismic transients. The list contains details of the solar flares generating sun quakes.

All egression power snapshots mapped in Figures 4.1 to 4.6, show considerably suppressed acoustic emission from the magnetic region, attributed to strong acoustic absorption by magnetic regions, discovered by Braun et al. (1988) (see also Braun, 1995; Braun et al., 1998; Braun and Lindsey, 1999).

Furthermore, all 6 mHz egression power snapshots also show acoustic emission “halos”, i.e. significantly enhanced acoustic emission from the outskirts of complex active regions (Lindsey and Braun, 1999; Donea et al., 1999). An arrow indicates where conspicuous seismic sources are seen in the 6 mHz egression power snapshots in all frames.

The first row of Figure 4.1 shows the **November 24, 2000** sun quake. The solar flare generating the quake was observed by *SOHO-MDI* operating in the high resolution mode.

The seismic emission is pointed out by the arrow, as in Figure 3.6. The source appears in the penumbra of a smaller spot in the 9236 AR. The excess white light emission presents an extended structure similar to a horse shoe and evolves over a few minutes. We noted a very good temporal correlation between the intensity continuum excess and the seismic power of the source. The white light horse-shoe signature presents two kernels, with the southwestern one spatially correlated with the egression power signature.

The temporal profile of the white light emission (seen in the first row of Figure 4.2) has a sudden increase at 04:58 UT with a three minutes peak, followed by a smoother decrease to pre-flare values. All the temporal profiles of the intensity continuum data have been calibrated to the quiet sun, therefore the scales in these plots show relative intensity.

The second row in Figure 4.1 shows the seismic emission associated with the **September 9, 2001** solar flare. The white light excess emission is ahead of the egression power maximum by  $\sim 3$  minutes. Significant acoustic emission at 6 mHz is visible in the penumbra of the main sunspot. The arrow indicates the most conspicuous feature of acoustic emission. The intensity difference from 20:42 to 20:43 UT, rendered on this row, shows two or possibly three, compact kernels in the southern penumbra of the main sunspot. This closely matches kernels that represent the sources of acoustic emission. This flare was extensively analysed by Donea et al. (2006b). We showed that, within the  $\sim 500$  seconds temporal resolution of the 6 mHz egression power computations, the acoustic signatures spatially and temporally coincide with the onset of the white-light emission during the flare. The spatial correspondence between the *GONG* intensity and the egression-power kernels is remarkable.

Some spots visible on the left side of the intensity continuum maps and the differences of intensity continuum maps, are actually atmospheric noise while recording the *GONG* data.

The temporal profile of the September 9, 2001 sun quake is shown in the

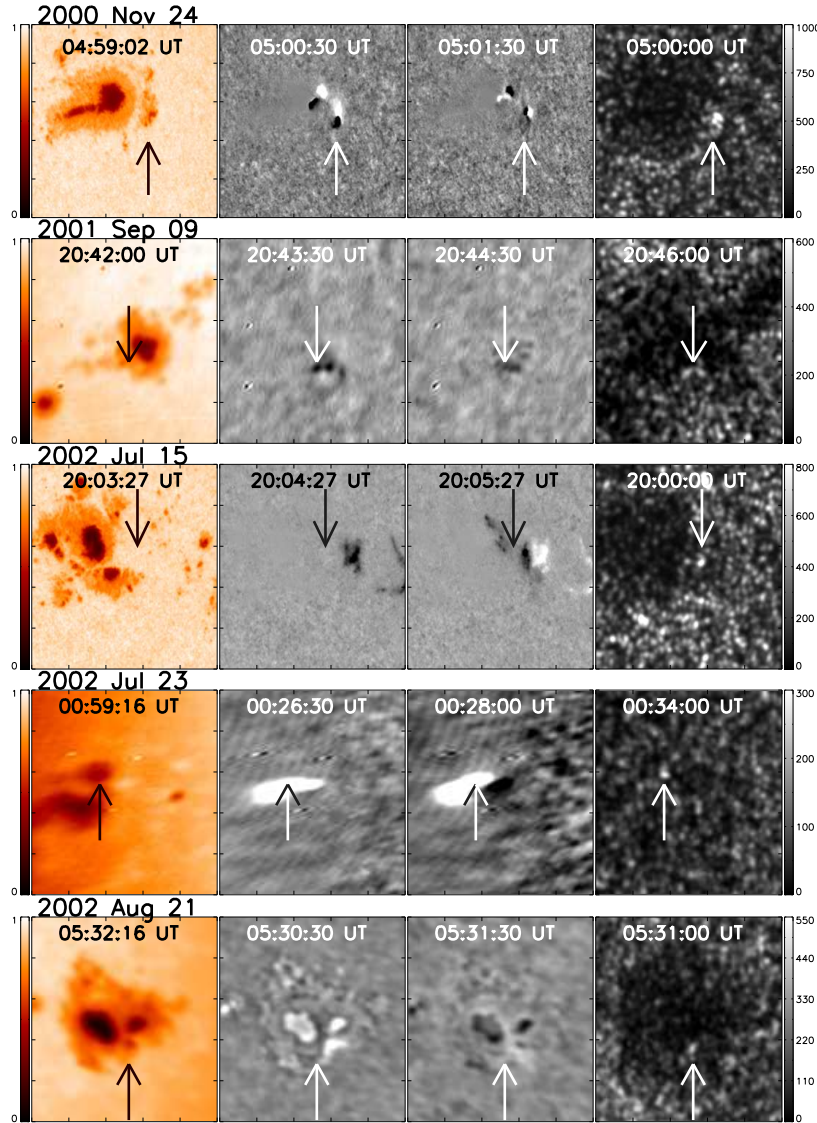


Figure 4.1: The continuum emission associated with the detected seismic source. Each row represents a specific sun quake with the date printed on top of the first frame. Each row is composed of an intensity continuum image of the active region - first frame; two intensity continuum differences showing the white light excess emission - next two frames; the last frame shows the egression power map at the maximum of the sun quake. Specific times are shown in each frame. The arrow points to the egression power signature.

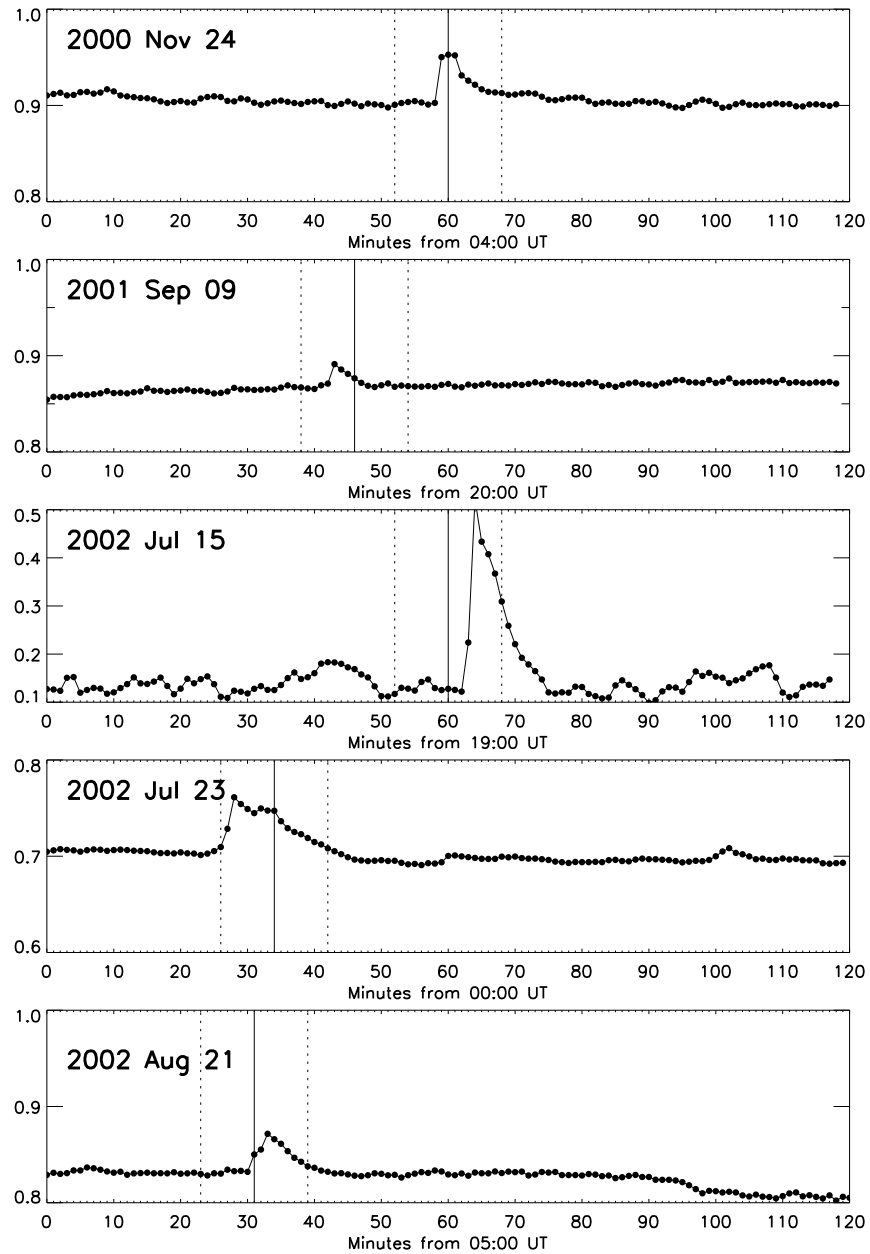


Figure 4.2: Temporal profiles of the intensity continuum data integrated over the sun quake area for the acoustically active flares. Specific dates shown on each row. The vertical line represents the maximum of the seismic emission. The dashed vertical lines are  $\pm 8$  minutes from the maximum.

second row of Figure 4.2. At 20:42 UT we can see the sudden increase in the excess emission of white light integrated over the sun quake area. 20:43 UT is the peak of this profile, after which, in about four minutes, the emission returns to pre-flare values.

The third row in Figure 4.1 shows the seismic emission from **July 15, 2002** which is the second sun quake covered by *MDI*'s high resolution data. This flare had a very wide and highly intense white light signature, that spread over almost the entire active region. Although the white light emission is about four minutes later than the egression power maximum, we must remember that the helioseismic holography technique introduces an  $\pm 8$  minutes smearing effect (see Equation 3.1). This sun quake and its corresponding white light emission appear in the western plages, near the main spot. The temporal profile of the WL emission shows an extreme steep peak at 20:02 UT (about three times the pre-flaring values, which makes this the strongest WL transient), followed by a steadier decrease, over about ten minutes, back to background values (third row in Figure 4.2).

On the fourth row we find the description of the **July 23, 2002** sun quake. We can see the image is smeared, due to the limb proximity of the AR. In addition, the poor quality in the WL images is due to atmospheric noise in the *GONG* data. Nevertheless, we could still detect significant seismic activity in the Doppler images. The seismic source lags the white light signature by about six minutes and is located in the middle of the white light excess emission.

The temporal profile included in the fourth row in Figure 4.2 shows the sudden temporal increase of the WL flux, starting at 00:26 UT, with a maximum at 00:28 UT and a second local maximum at 00:34 UT. The decrease to pre-value flares spreads over more than ten minutes.

The last row of Figure 4.1 shows the seismic emission from **August 21, 2002**. The data is very noisy, as seen in the intensity continuum differences. However, we could notice an excess corresponding to the location of the seismic emission, in the southern region of the penumbra, the seismic source lagging by about two minutes.

The temporal profile can be seen in the last row of Figure 4.2 and presents the increase over three minutes. Then, after about seven minutes it returns to pre-flare values.

Figures 4.3 and 4.4 show the next set of five sun quakes as follows: on the first row we can see the sun quake triggered by the **October 23, 2003** solar flare, second and third rows **October 28** and **29, 2003** sun quakes; fourth

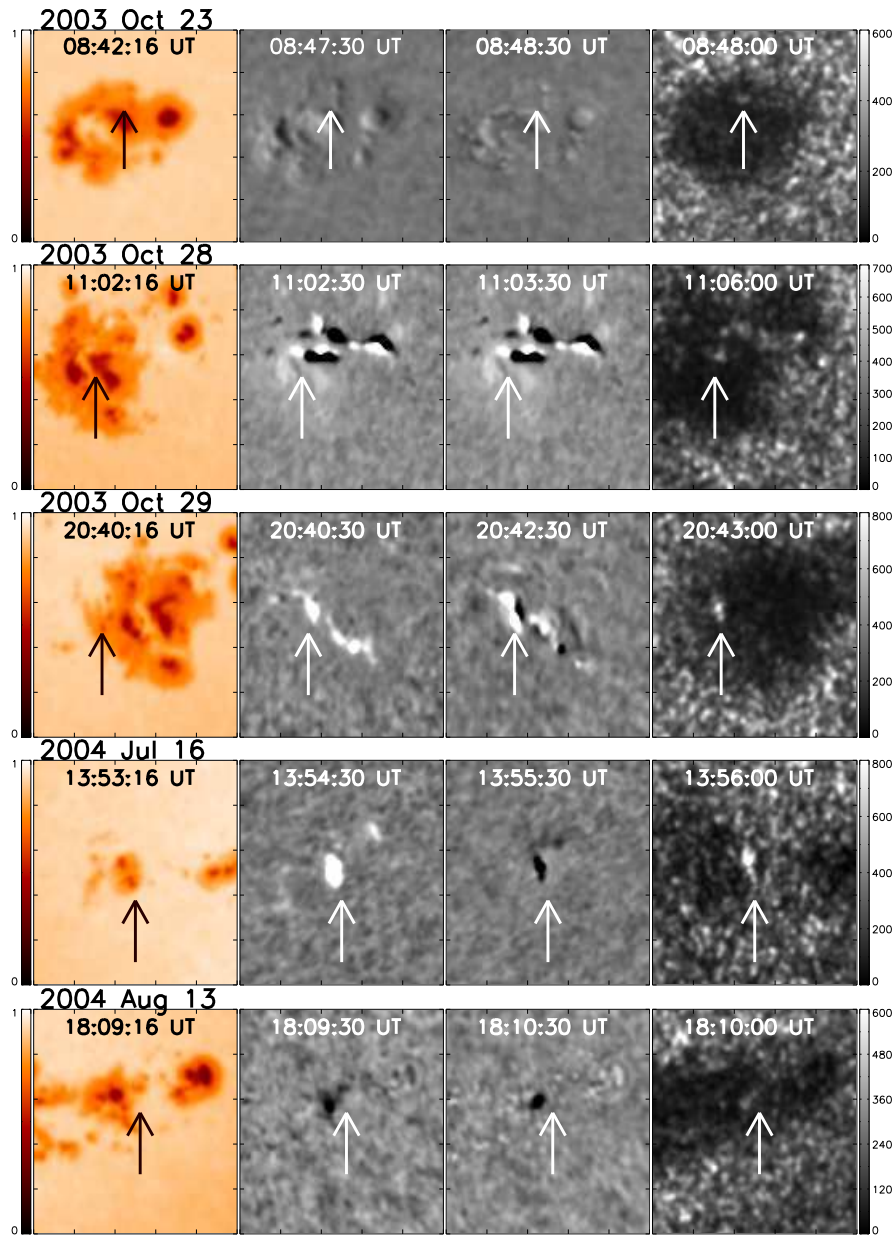


Figure 4.3: Same as Figure 4.1

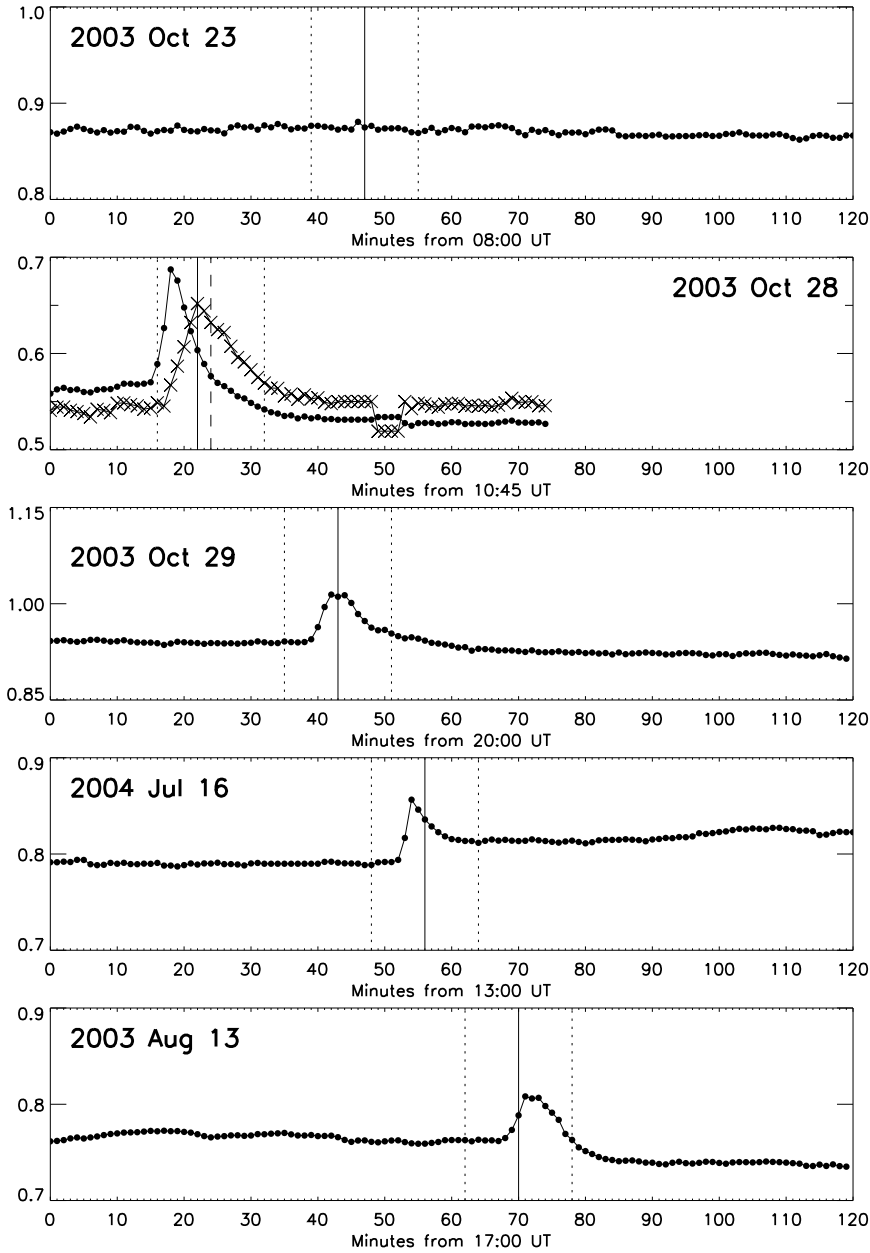


Figure 4.4: Same as Figure 4.2.

row: **July 16, 2004** and the last row from this figure shows the **August 13, 2004** sun quake. These seismic sources had a very good data coverage by the *GONG* instrument. The first row in Figures 4.3 and 4.4 describing the **October 23, 2003** sun quake is characterised by an extremely noisy AR in the intensity continuum data. Hence there is practically no excess emission in the frame differences, nor in the temporal profile, although there is a WL signature visible in the raw data.

The second row in Figures 4.3 and 4.4 shows the **October 28, 2003** sun quake. We notice here the same double structure of the WL, as the egression power, with a maximum in emission nearly four minutes ahead of the time of maximum emission from the sun quake.

The temporal behaviour of the WL emission in this case shows the same sudden steep peak (with an increase greater than 50%) starting at 11:02 UT and 11:06, respectively, for the two seismic sources associated with the October 28, 2003 flare (as defined in Figure 3.24). Both of these profiles come back to pre-flaring values after about four and two minutes, respectively.

Third row in Figures 4.3 and 4.4 shows the WL emissions associated with the **October 29, 2003** flare. Here, the WL signature shows two different kernels appearing in the region of plages between the spots of the NOAA 10486AR. The north-eastern kernel coincides with the acoustic emission having its maximum less than a minute ahead. Their shapes are strikingly similar. [Donea and Lindsey \(2005\)](#) have widely analysed these seismic transients, that is the seismic emission associated with October 28 and 29, 2003 flares. Here we re-did some of the analysis, mainly emphasizing the white light properties of the seismic transients.

The temporal profile shows the sudden increase in WL emission starting at 20:40 UT, having a maximum value for three minutes. There is practically no time lag between the WL maximum and the sun quake one.

The last row of Figures 4.3 and 4.4 shows one of the most spectacular solar quakes, generated by the **July 16, 2004** flare. The WL spatial signature is also very well correlated with the seismic transient. The sudden onset of the WL flare starts at 13:52 UT, lasts for about two minutes, after which, the WL profile decreases to pre-flare values after seven minutes.

The last row of Figures 4.3 and 4.4 shows the sun quake of **August 13, 2004**. Despite the data being affected by atmospheric turbulence, the WL signature was visible and had a morphology similar to that of the seismic source. Both of these signatures appear in the region adjacent to the eastern penumbra and plages between the two spots of NOAA 10656AR. The next

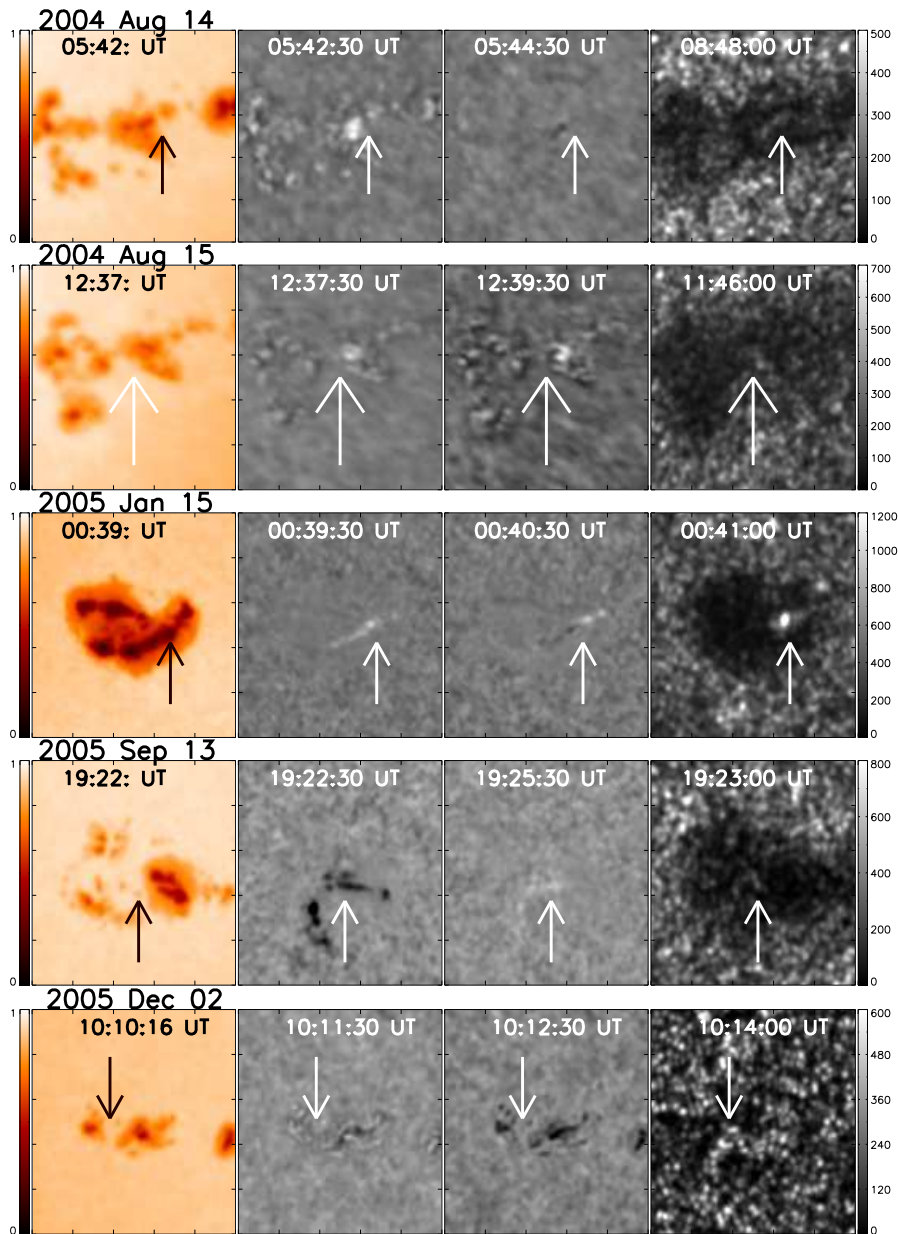


Figure 4.5: Same as Figure 4.1

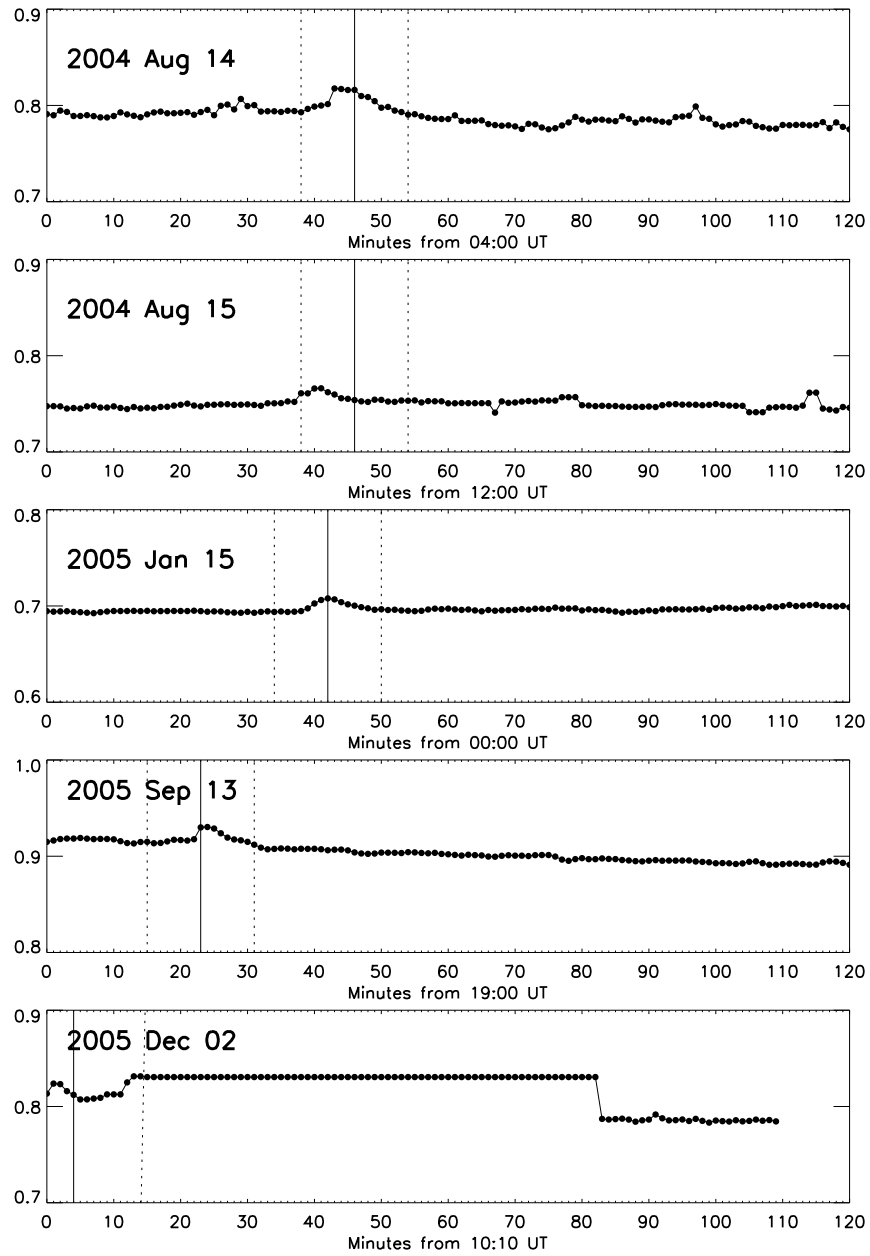


Figure 4.6: Same as Figure 4.2.

two sun quakes produced in the same AR were similarly located.

The WL observations of the **August 14 and 15, 2004** solar flares are noisier, but the WL signature was still visible and spatially correlated with the seismic transient.

The third row in Figures 4.5 and 4.6 shows the **January 15, 2005** sun quake. The WL signature and the seismic signature have the same location and orientation. Their maxima are practically at the same time. The temporal profile of the WL emission does not show the same sudden effect. Here, the increase towards flaring values is about four minutes. After four more minutes, the profile returns to pre-flaring values.

The fourth row in Figures 4.5 and 4.6 shows the **September 13, 2005** sun quake. The WL signature is huge and lasted a long period of time, compared with the seismic transient evolution. The maximum of the WL starts at the time of the acoustic emission maximum. The WL temporal profile shows the usual sudden onset at 19:02 UT, reaching its maximum after just one minute, and returning to background level after about five minutes.

The last row in Figures 4.5 and 4.6 shows the **December 2, 2005** sun quake. This seismic source is widely spread, covering most of the eastern penumbra of the hosting AR. The WL signature has a similar morphology. The WL observations were available only for the time interval 10:10 to 10:23 UT. This was just enough to watch the sudden WL flux increase followed by a smoother decrease to pre-flare values.

To conclude, the visible continuum emission, similarly aligned with the holographic seismic signatures, led us to the proposal in [Donea et al. \(2006b\)](#) based on similar instances in other seismically active flares, that heating of the photosphere may contribute to the observed seismic emission, possibly as a result of back-warming by the chromospheric source of the continuum emission. We will analyse in detail this process in the following chapter of this thesis.

## 4.2 Results of the Analysis of SOHO/MDI Doppler Data

We applied the local helioseismic technique known as computational seis-

mic holography (Lindsey and Braun, 2000) to the *SOHO/MDI* observations and imaged the seismic source of flares. The resulting “egression power maps” showed a relatively compact seismic source surrounded by some diffuse emission. The seismic sources were clearly visible in 2–4 mHz holographic images and even more pronounced in 5–7 mHz images. The *SOHO/MDI* data (Postel projected images) are also used to identify seismic ripples on the photosphere, and hence to identify sun quakes.

Every seismic event starts with a local depletion of the photosphere due to the impact created by the energy and probably momentum deposited by the solar flare. Kosovichev and Zharkova (1998) and later Kosovichev (2006); Martinez-Oliveros et al. (2007); Moradi et al. (2007) analysed in details the emerging seismic waves appearing about 20 minutes after the photospheric impact. The difficulty in finding these wave-like features on the solar surface is increased by the continuous oscillation of the photosphere and also by the projection effects when reducing the data. It was also shown that subphotospheric flows and magnetic field (Schunker et al., 2008) in active regions hosting a seismic flare, can decrease the velocity signal from a seismic source.

There are several ways to analyse the Dopplergram images of active regions. In the case of exceptionally powerful seismic transients (for example the flare of January 15, 2005), the surface signature is quite evident in the raw *MDI* Doppler observations (Kosovichev, 2006; Moradi et al., 2007). To extract the flare seismic oscillations we subtracted consecutive *MDI* Doppler images separated by one minute in time. We applied this Doppler-difference method to a period of observation ( $\sim 1$  hour) around the time of the flare.

Plotting the average *MDI* line of sight velocity  $\langle v \rangle$ , integrated over the sun quake area, and the root mean square (abbreviated  $RMS_V$ ) of  $\langle v \rangle$  gives also an insight into the temporal trends of the event. For these computations we have used the following definition of RMS:

$$RMS_V = \sqrt{\frac{1}{N} \sum_{k=1}^N v^2 - \left( \frac{1}{N} \sum_{k=1}^N v \right)^2} \quad (4.1)$$

where  $N$  is the number of pixels inside the sun quake area and  $\langle v \rangle$  is the local value  $\langle v \rangle$  (m/s) of the pixel.

The following two sections will present characteristics of the temporal evolution of the photospheric velocity disturbances during four of the de-

tected sun quakes. We will analyse the seismic events with large amplitudes ring-shaped waves propagating from the flare sites.

### 4.2.1 Temporal LOS-velocity Profiles

The temporal profiles of  $\langle v \rangle$  are obtained by integrating the velocity signal over the area of the seismic transient (normally around 10–20 Mm<sup>2</sup>). We then compare the velocity temporal profile with that of the acoustic emission.

Figures 4.7 to 4.9 show (one sun quake per row) the mean velocities  $\langle v \rangle$  and RMS<sub>V</sub>. All frames show the time at the maximum of the flare along with the  $\pm 8$  minutes time interval. The amplitude of the flare-generated seismic waves (ripple-like features) rarely exceeds 100 m/s. Thus, because of the strong stochastic motions in the background, these waves are difficult to detect.

The first row in Figure 4.7 shows the variation in the LOS velocities for the **July 9, 1996** sun quake. This is similar to the results of [Kosovichev \(1996\)](#). We can see that the dent in the velocity profile at the time of the flare represents a local disturbance in the source region that begins with a rapid downward depression (redshift) of the photosphere followed by an upward rebound (blueshift).

According to [Kosovichev \(1996\)](#), the shock observed in *SOHO/MDI* Dopplergrams as a localized large-amplitude velocity impulse of about 1 km/s represents the first hydrodynamic impact of the flare. In addition, [Kosovichev and Zharkova \(1998\)](#) found that the seismic wave propagates anisotropically, having a quadrupole component. While we regard the existence of a significant local disturbance to be secure, its interpretation in terms of absolute motion requires some caution. One needs to identify thermal or other non-Doppler radiative-transfer effects precipitated in magnetic photospheres by flares that could be confused with Doppler effects.

The RMS<sub>V</sub> for this flare has a peak with a magnitude about twice the background noise. This plot shows the significance of the downward depression of the photosphere, at the moment of ignition of the seismic source.

The second row in Figure 4.7 describes the **June 6, 2000** sun quake with a similar descending velocity trend and a local minimum at the beginning of the flare in the mean values, and a sharp peak in the RMS<sub>V</sub> values.

The third row in Figure 4.7 shows the temporal profile of the LOS velocities for the **November 24, 2000** sun quake. The quality of the data – high resolution data – and the position of the hosting AR – very close to the

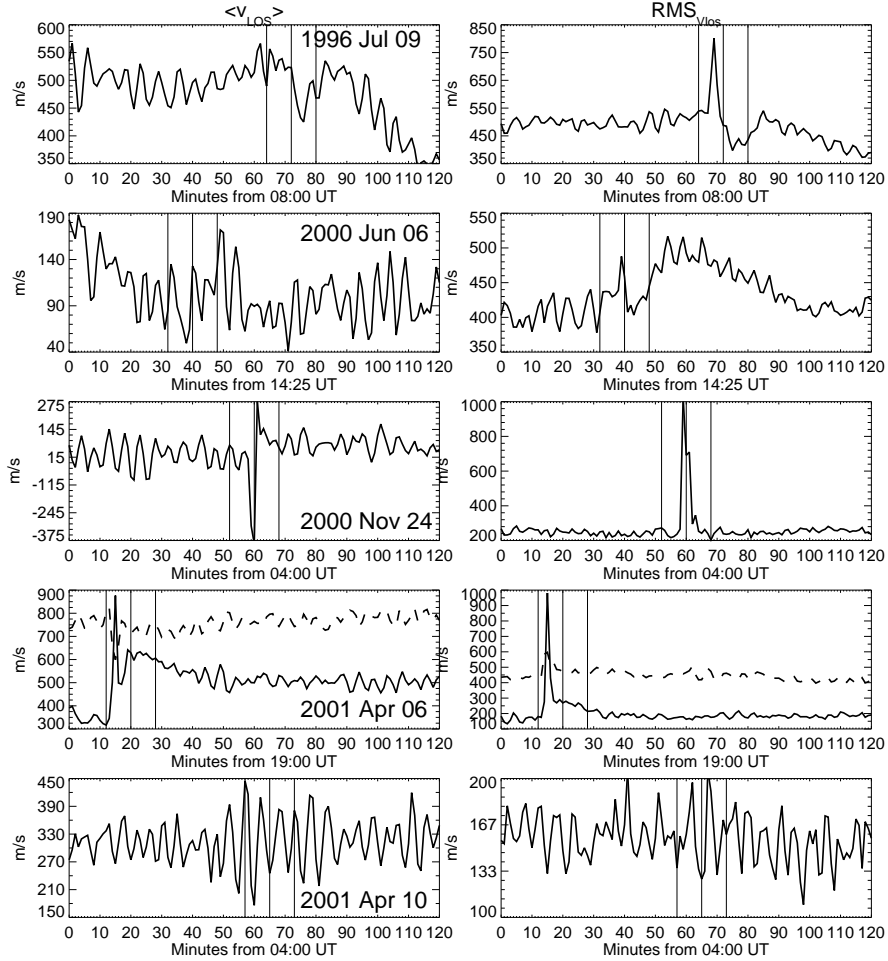


Figure 4.7: Time series of the Doppler LOS velocities  $\langle v \rangle$  and  $\text{RMS}_V$  integrated over the sun quake area. The corresponding dates are shown on each row. The vertical central line represents the flare time at the maximum of the *GOES* flux, whereas the other two lines show a time interval of  $\pm 8$  minutes.

centre of the Sun – makes this flare one with the best data coverage, showing the depletion in the photospheric level coincident with the maximum of the flare. The corresponding  $\text{RMS}_V$  has a very sharp peak with a magnitude of five times the background level.

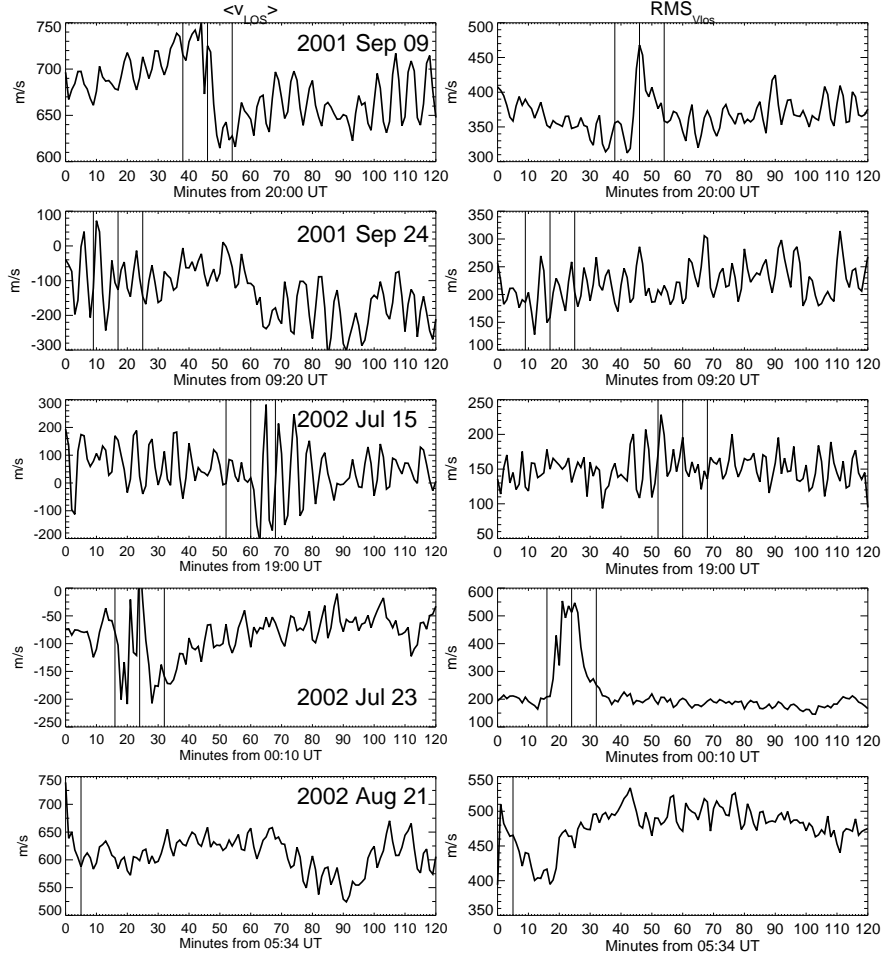


Figure 4.8: Same as Figure 4.7.

The **April 6, 2001** sun quake has a double morphology, with prominent seismic sources acting at the photospheric level. The fourth row in Figure 4.7 shows the Doppler velocity profile of the two sources. In order to have the plots of both seismic sources on the same graph, we have scaled the values of the southern source adding a constant factor - 750 - (see Figure 3.8). The northern source is plotted with a straight line and the southern one is plotted with a dashed line. The northern source has a high peak in the LOS and

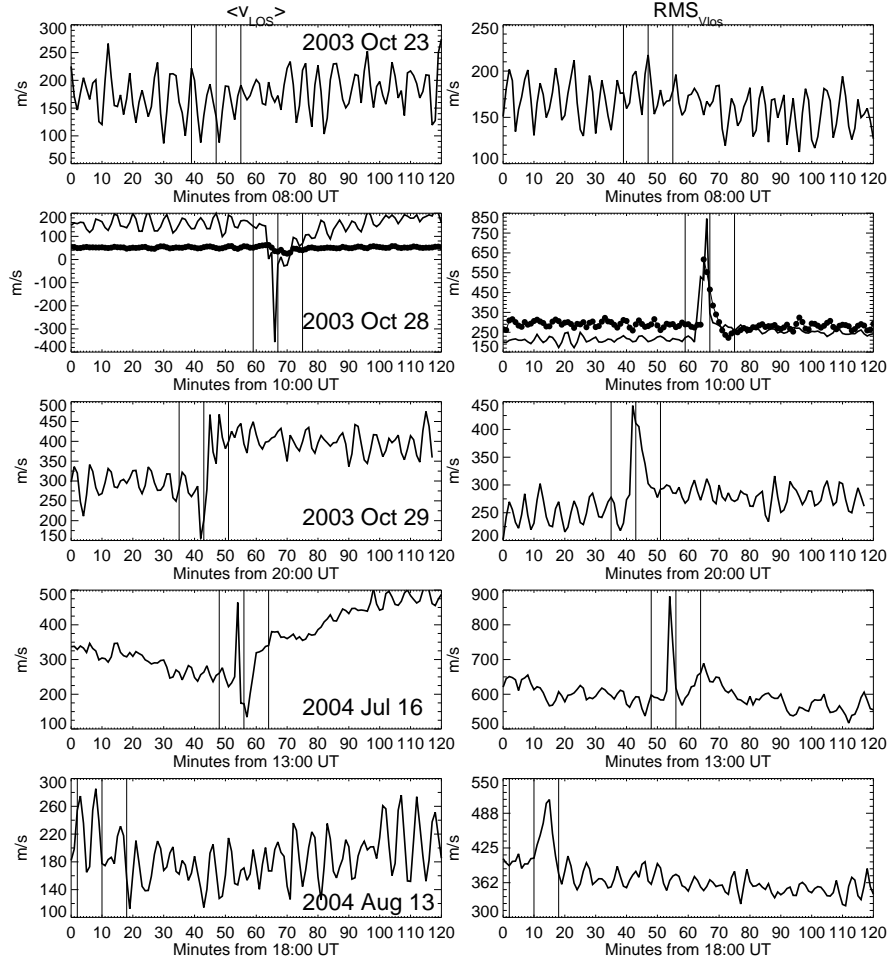


Figure 4.9: Same as Figure 4.7.

$\text{RMS}_V$  velocities, while the southern one has a smaller peak in both plots.

The last row in Figure 4.7 describes the **April 10, 2001** sun quake. Here the local velocity variations seem to follow the general sinusoidal trend, but with increased amplitude at the time of the flare. The seismic signal was much more difficult to identify in the raw *MDI* data.

Figure 4.8 shows the LOS velocities variations for the next five sun quakes **September 9 and 24, 2001, July 15 and 23 and August 21, 2002**.

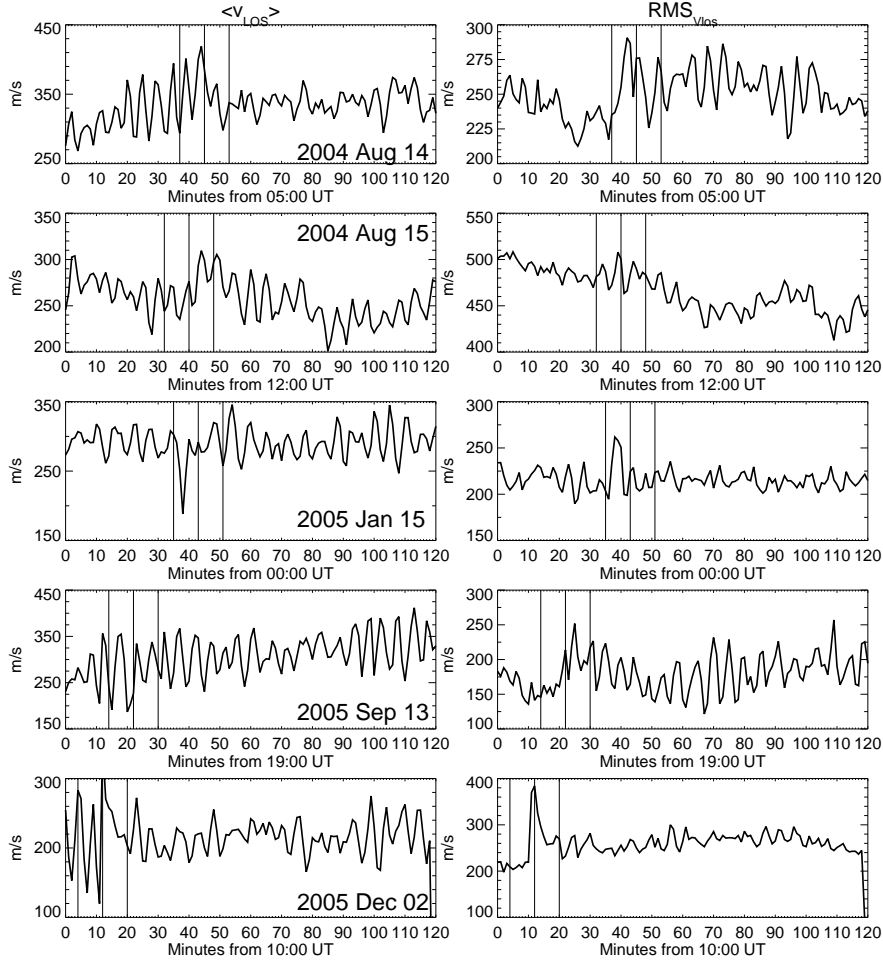


Figure 4.10: Same as Figure 4.7.

Unfortunately the data for the August 21, 2002 is corrupted before 05:34 UT, however strong variation at the time of the flare can be seen.

The September 9, 2001, July 23, 2002 and August 21, 2002 are characterised by high depletion at the beginning of the flare, with corresponding high peaks in the  $\text{RMS}_V$  profiles. The September 24, 2001 and July 15, 2002 flares have higher amplitudes associated at the flaring time.

Figure 4.9 shows the LOS velocity variations for the next five sun quakes:

### **October 23, 28 and 29, 2003, July 16 and August 13, 2004.**

The **October 23, 2003** sun quake does not have a significant variation in the observed photospheric velocities, due to strong noise in the data.

The **October 28, 2003** flare has strong depletions associated with both sources (see Figure 3.24). In order to plot the time series for both kernels we have divided the series for the southern source by a factor of 10. Both profiles show an  $\text{RMS}_V$  variation of about five times the background noise.

The **October 29, 2003** and **July 16, 2004** flares are very similar in the  $\langle v \rangle$  time series, having strong depletion at the time of the flare then showing higher mean velocity values after the flare and high peaks in the  $\text{RMS}_V$ .

The **August 13, 2004** flare is characterised by a strong variation at the time of the flare, with a decreasing trend for the decay period of the flare and a high peak in  $\text{RMS}_V$  values a few minutes after the maximum of the flare.

Figure 4.10 shows the LOS velocity variations for the last five sun quakes in our count: **August 14 and 15, 2004, January 15, September 13 and December 2, 2005.**

In conclusion, we can say that the sun quake sources are observed directly in the *MDI* Dopplergrams as localized high-velocity impulses. The local disturbance appears to be the result of a sudden depression of the photosphere in the neighbourhood of the sun quake. Such a depression would be consistent with a wave travelling substantially downwards from the overlying chromosphere, some of which penetrates into the subphotosphere. The seismic sources are typically located in penumbrae of active regions. Detailed analysis of *SOHO/MDI* data showed that the structure of sun quake sources can be quite complicated in space and time.

## **4.2.2 Seismic Ripples observed on the SOHO/MDI Doppler maps**

To extract the seismic oscillations in the observations we subtracted consecutive *MDI* Doppler images separated by one minute in time. Four solar flares generated sun quakes with easily detectable wave fronts: July 9, 1996, July 16, 2004, January 15, 2005 and December 2, 2005. These waves form an almost circular expanding ring. The velocity of expansion of the ring is determined by the sound speed inside the Sun and by using a solar model. Typically, the expansion speed increases from 10 km/s to 100 km/s. In the

egression power maps (see Chapter 2) the wave signal is integrated over the whole time of sun quake evolution, along the time-distance ridge, thus giving the total average of the seismic signal power in each point of the photosphere.

The wave accompanying the first discovered sun quake **July 9, 1996** (Kosovichev and Zharkova, 1998), is shown in Figure 4.11 and has the shape of an ellipse with the two foci oriented in the NS direction. The centre of the expanding wave coincides with the seismic source (confirming the initial observation of Kosovichev and Zharkova, 1998; Donea et al., 1999). This ellipse has its major axis very well aligned with the 6 mHz egression power signature at 09:12 UT which is shown as contour plots in all frames. The seismic wave developed 20 minutes after the generation of the seismic source. Figure 4.11 shows in the three central frames the seismic waves which lasted for about six minutes with dotted circles, after which they dissipate into the photospheric noise.

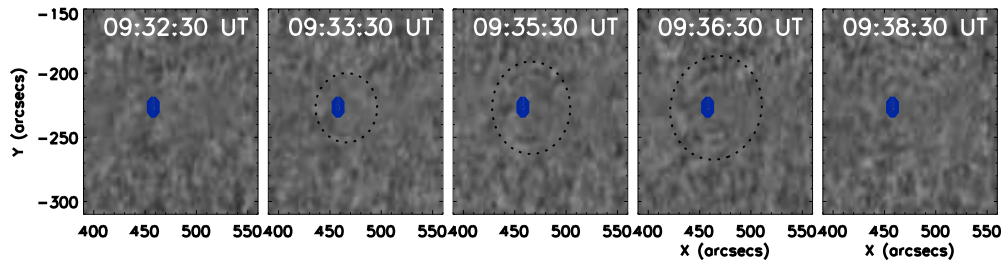


Figure 4.11: Snapshots of the *MDI* Doppler difference images showing the seismic waves accompanying the solar flare of July 9, 1996 (dotted curves). The contour levels show the location of the 6 mHz egression power signature at its maximum. These figures can also be compared with the results presented in the Figure 3.2.

Figure 4.12 shows the seismic wave, developing 18 minutes after the flaring of the **July 16, 2004** solar event. The wave fronts have elliptical shapes (underlined by the dotted contours in the three central frames), with the main axis oriented along the egression power signature at 6 mHz which is shown as contour plots in all frames). The seismic waves dissipate after about five minutes.

Figure 4.13 shows the seismic wave appearing at the photospheric level 21 minutes after the occurrence of the **January 15, 2005** flare. The flare of January 15, 2005, produced the most conspicuous acoustic signature of

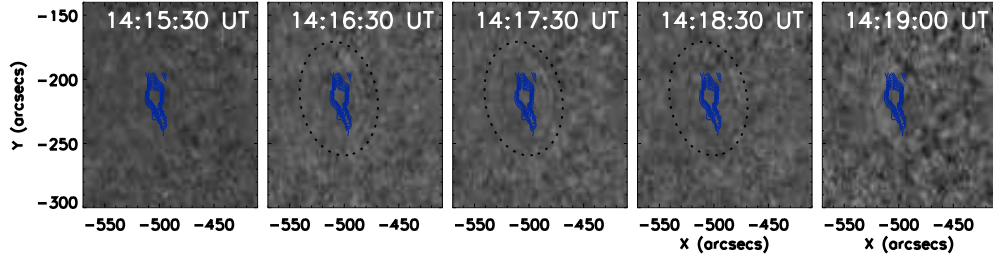


Figure 4.12: Same as 4.11 for the July 16, 2004 sun quake.

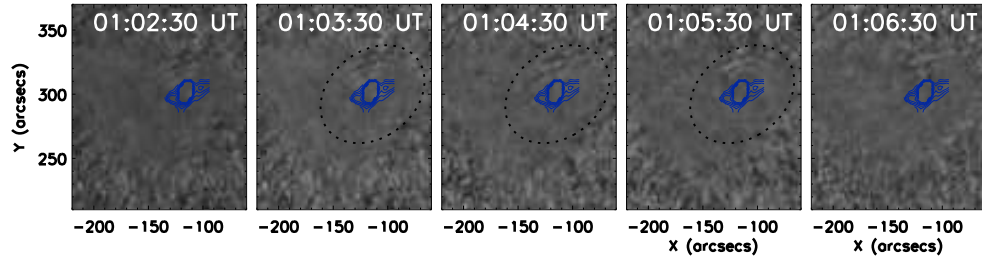


Figure 4.13: Same as 4.11 for the January 15, 2005 sun quake.

any flare that has induced a detectable seismic emission. Its sun quake has the shape of an arc of ellipse with the major axis in the SE–NW direction. We recall here that this sun quake was extensively analysed by [Beşliu et al. \(2005a\)](#); [Moradi et al. \(2006b,a, 2007\)](#); [Martinez-Oliveros et al. \(2008a\)](#).

We also include a zoomed in map (Figure 4.14) to show the morphology of the seismic ripples and its anisotropy.

Another interesting seismic event with visible seismic ripples in the *MDI* Doppler differences map is shown in Figure 4.15. The **December 2, 2005** solar flare generated a powerful sun quake. The seismic wave at the solar photosphere is only seen as two fragments of arcs around the seismic source: one arc expands in the north-west direction and the second one extends in the southern direction. Again, the position of the seismic source and the symmetry of the expanding arcs are remarkable. The wave disappears after about five minutes.

Again, we include here a zoom in map (Figure 4.16) to show the morphology of the seismic ripples and its anisotropy. A strong sudden downflow

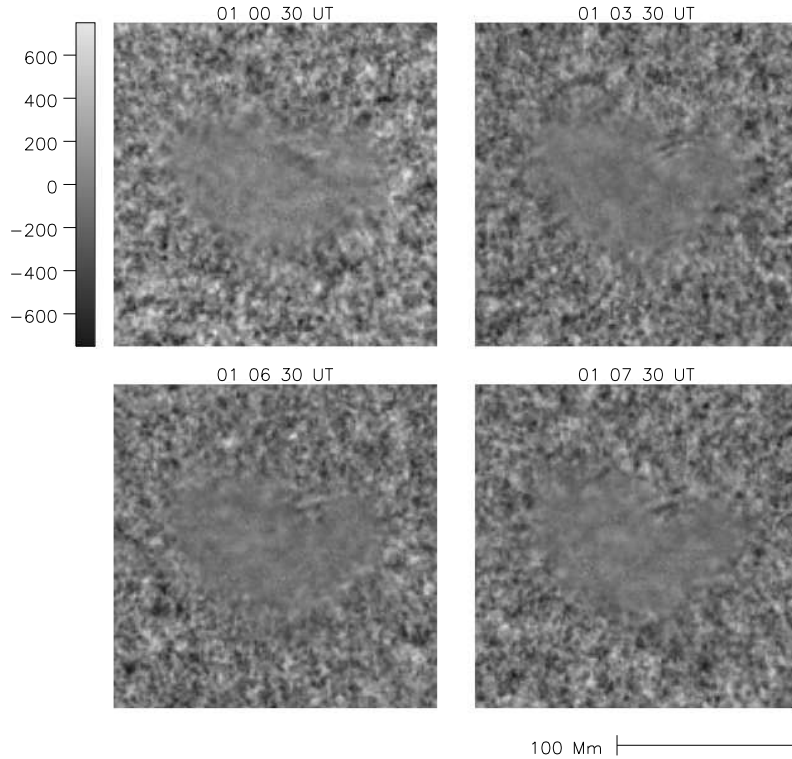


Figure 4.14: Left: Difference between consecutive *MDI* Doppler images of AR10720 at: 00:40 UT and 00:41 UT. The local velocity disturbance is visible near the centre of the image; and Right: 01:05 UT and 01:06 UT. The asymmetrical elliptical wave packet (indicated by arrows) propagates 12–15 Mm from the flare centre in the north-east by south-westerly direction to a distance of 21 Mm from the flare and lasted 10 minutes.

signature is visible in the first frame.

In conclusion, fewer than 20% of the solar flares with significant seismic energy deposited into the photosphere generated detectable photospheric ripples against the five-minute oscillation background. Time-distance amplitude profiles for the ripples as shown above have been intensively used by [Kosovichev and Zharkova \(1998\)](#); [Kosovichev \(2006\)](#); [Martinez-Oliveros et al. \(2007\)](#); [Zharkova and Sekii \(2007\)](#) to infer Doppler difference amplitudes av-

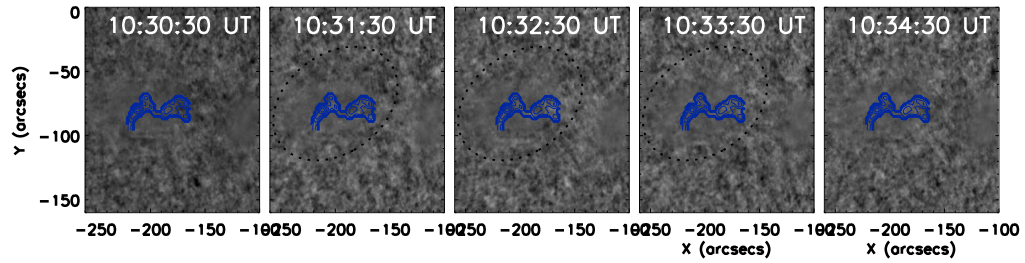


Figure 4.15: Same as 4.11 for the December 2, 2005 sun quake.

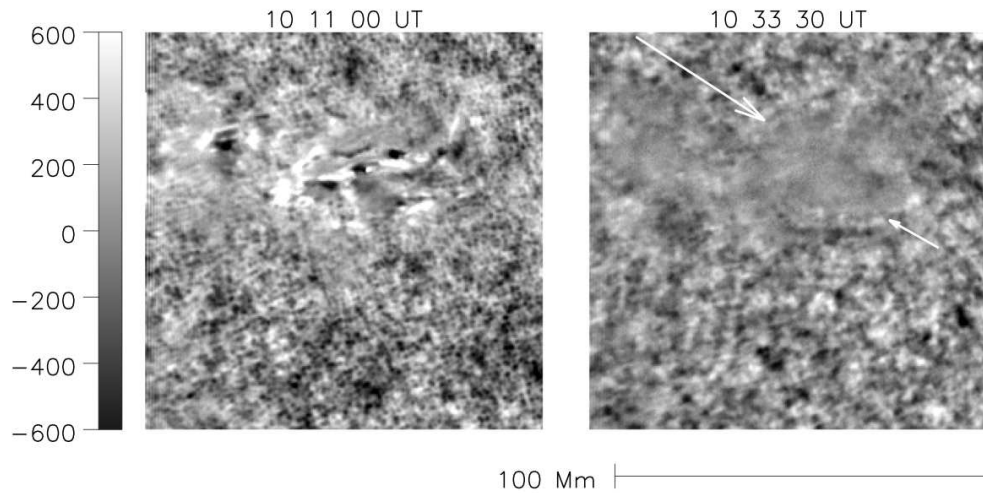


Figure 4.16: Left: Difference between consecutive *MDI* Doppler images of AR10826 at: 10:11 UT and 10:12 UT. The Doppler disturbance is visible near the centre of the image. Right: Difference between consecutive *MDI* Doppler images at 10:33 UT and 10:34 UT. The asymmetrical elliptical wave packet (indicated by arrows) propagates 15 Mm from the flare centre in the north-east by south-westerly direction to a distance of 30 Mm from the flare. It was easily detected in the regions of quiet sun surrounding the host active region.

eraged along curves of constant radius over a wide range of azimuths over which the surface ripples were visible. However, for very weak sun quakes,

well hidden in the noisy background of the photosphere this technique is very difficult to use. Helioseismic holography proved to be more sensitive than the time-distance diagnostic in detecting the origin of the seismic ripples, the location of the seismic transient. Of course, for some flares holographic diagnostics showed weak emission or might have even missed extremely weak seismic signals. For those weak signals, in order to confirm that they were true seismic signals and not just solar noise, we compared the acoustic maps with other maps at different wavelengths, in search for correlations.

### 4.3 Results of Analysis of SOHO/MDI Magnetic Transients

We have seen that almost all instances of seismic sources we have encountered so far, like their associated white-light flares, have been located in sunspot penumbrae, which have highly inclined magnetic fields. Schunker *et al.* (2005) have shown that magnetic forces are of particular significance for acoustic signatures mainly in penumbral regions. Therefore, understanding the magnetic configuration of the coronal loops on top of which solar flares are generated would give us an insight into the seismic diagnostics of active regions. This will be useful for addressing questions concerning the relationship between the inclined magnetic fields and the role of fast and slow magneto-acoustic mode coupling in the magnetic photospheres.

In this chapter we will show time series of the mean and the root mean square ( $\text{RMS}_B$ , see Equation 4.1) values of the line-of-sight (LOS) magnetic field  $\langle B \rangle$ , integrated over area of the seismic source (the integration area is calculated from the egression power maps, where the seismic source size can be determined).

Figures 4.17 to 4.20 show the magnetic variations at the photosphere for the acoustically noisy flares such as: Figure 4.17: **June 6 and November 24, 2000, April 6 and 10, and September 9, 2001**; Figure 4.18: **September 24, 2001, July 15 and 23, August 21, 2002 and October 23, 2003**; Figure 4.19: **October 28 and 29, 2003, July 16, August 13 and 14, 2004**; Figure 4.20: **August 15, 2004, January 15, September 13, and December 2, 2005**.

Using an average value of the magnetic field over the area of the seismic

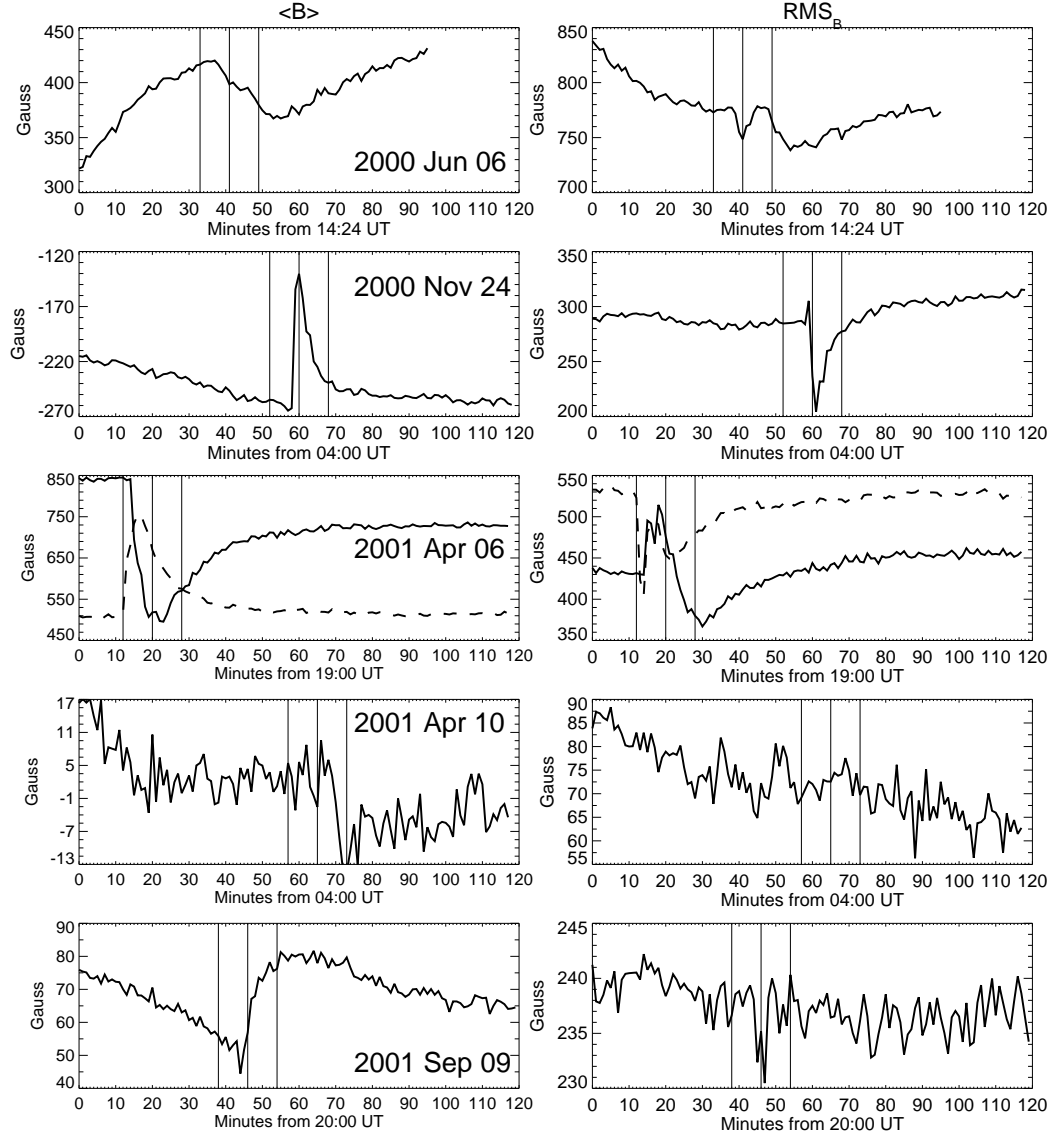


Figure 4.17: Time series of the mean  $\langle B \rangle$  and the root mean square of the LOS magnetic field  $\text{RMS}_B$  integrated over the area of the seismic source. Each row represents a sun quake. Specific dates are shown in each frame. The vertical lines mark the time when the flare was at its maximum (in X-ray emission as given by *GOES*) surrounded by the time interval  $\pm 8$  minutes.

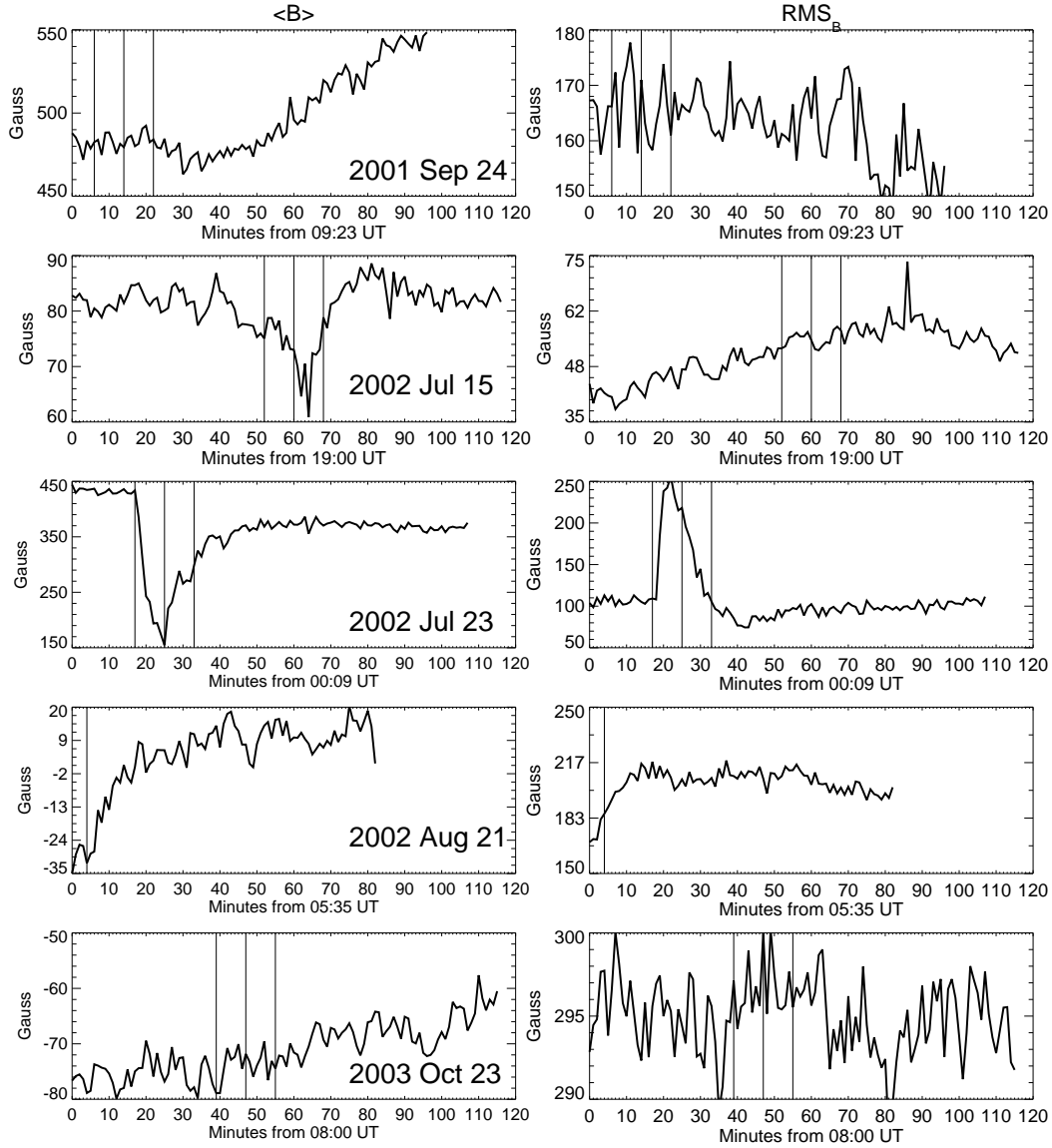


Figure 4.18: Same as Figure 4.17

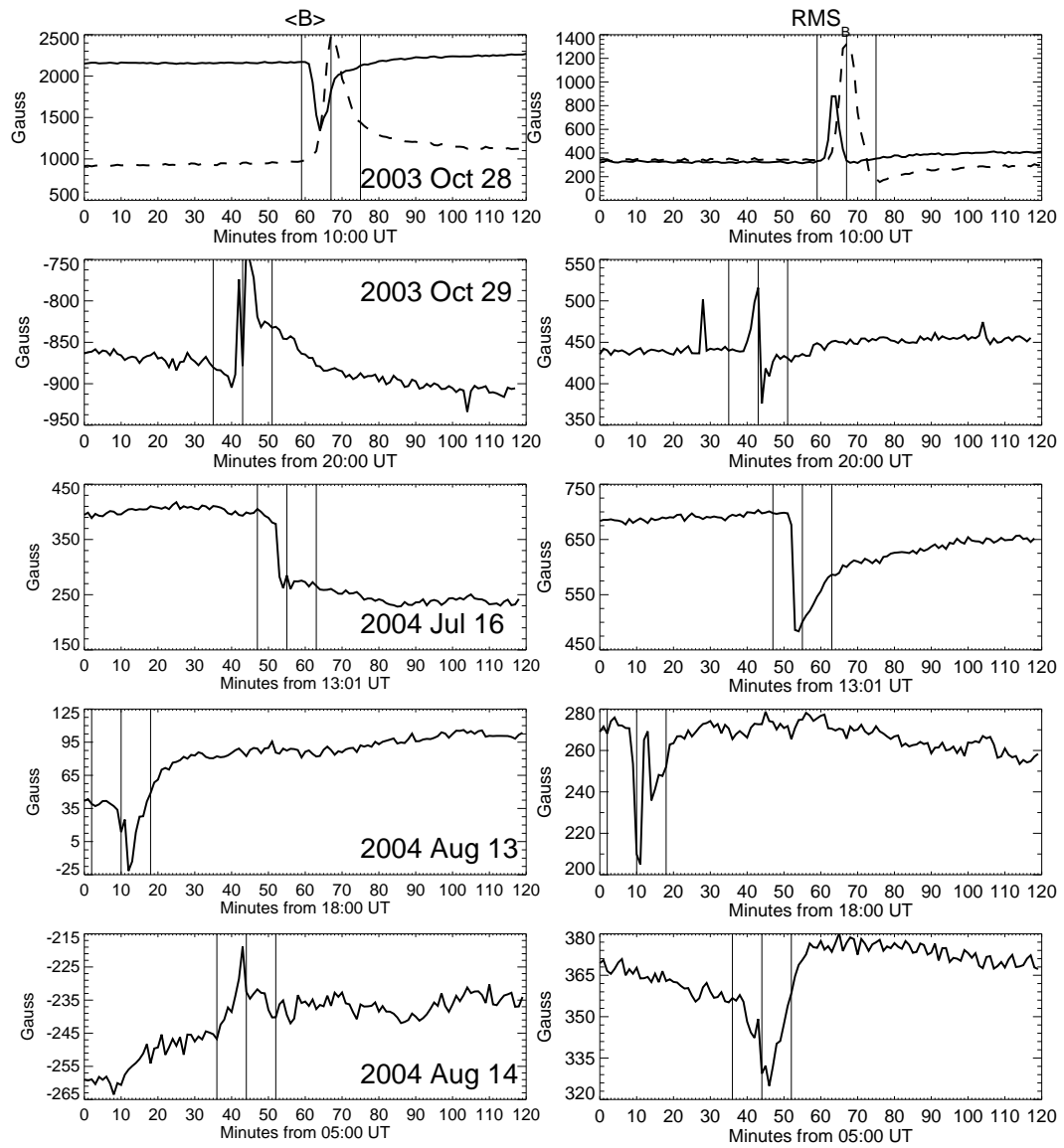


Figure 4.19: Same as Figure 4.17

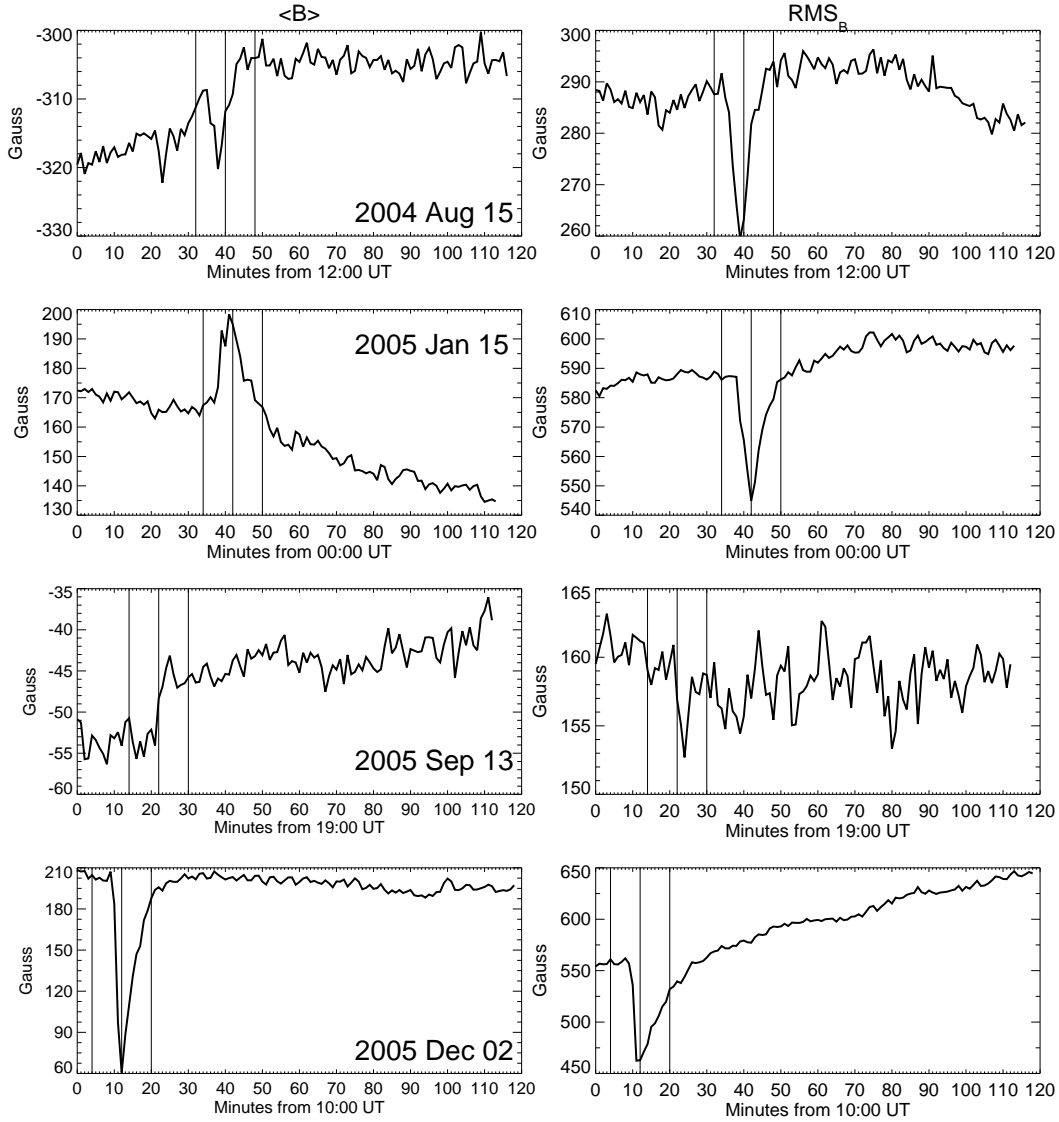


Figure 4.20: Same as Figure 4.17

source has to be treated with caution, since one can average over positive and negative magnetic fields hiding some of the important magnetic local

changes. However, we can clearly see the depositions or depletions of magnetic energy (represented as  $\text{RMS}_B$  in all time series of all Figures 4.17 to 4.20). The maximum of the magnetic variation happens usually at the same time as the maximum of the flare. The sudden loss of energy at around 05:00 UT November 24, 2000 or at 20:44 UT September 9, 2001 for example, may suggest that significant magnetic energy was released into the solar flare. This drop in energy is also correlated with hard X-ray (HXR) emissions which is thought to represent bremsstrahlung emission from high-energy coronal electrons impinging into the chromosphere (Brown, 1971; Moradi et al., 2007). Because the *MDI* magnetograms measure only the LOS component of the magnetic field, the observed variations in  $\langle B \rangle$  and  $\text{RMS}_B$  could also be caused by changes in the inclination of the magnetic field lines at and above the photosphere.

All these magnetic variations are short, evolving in less than 10 minutes.

Generally, the  $\text{RMS}_B$  of the magnetic field intensity shows a sudden decrease of the background level, followed by a recovery, as compared to the background level before the flare (similar changes have been observed by Kosovichev and Zharkova, 2001; Sudol and Harvey, 2005; Ambastha et al., 1993; Wang et al., 2005). A similar analysis was undertaken in Beşliu et al. (2005b), for the Halloween flares.

We conclude that the acoustic activity of an active region is clearly related to the structure of the coronal magnetic field. This is also relevant for the precipitation of non-thermal particles towards the chromosphere and deposition of energy into the photosphere. Martinez-Oliveros et al. (2007) suggested that the coronal magnetic field configuration (height of loops) can be a relevant factor in the generation of photospheric seismic waves. They analysed the seismic transient of the M7.4 solar flare of August 14, 2004, and showed that the seismic source was located beneath low-lying high-sheared magnetic field loops. This type of configuration seems to be the most efficient way of transporting the flare energy towards the photosphere. However, this study needs to be extended to a more detailed analysis of the magnetic field structure evolution during acoustically active flares.

## 4.4 Results of analysis of TRACE UV Continuum Data

The key data that we are presenting here is shown as images in the *TRACE* UV 1600Å line just above the sun quakes photospheric areas in the flaring active region. This line is known to be an emission line with a bandwidth of 275 Å and a temperature range from 4000 to 10 000K.

Figure 4.21 shows the flare of **June 6, 2000** (start 14:58 UT, max 15:25 UT, end 15:40 UT, X2.3-type). We can observe the brightening of a few UV kernels in the pre-flare stage (before 14:58 UT which is the time when the flare starts). From 15:00 UT the central 1600Å kernel brightens considerably. The 1600Å kernel is located just above the seismic source (contour plots shown in the first frame in Figure 4.21) and it was excited before the seismic source reached its maximum acoustic activity (as defined by the time when the 6 mHz egression power reached a maximum value).

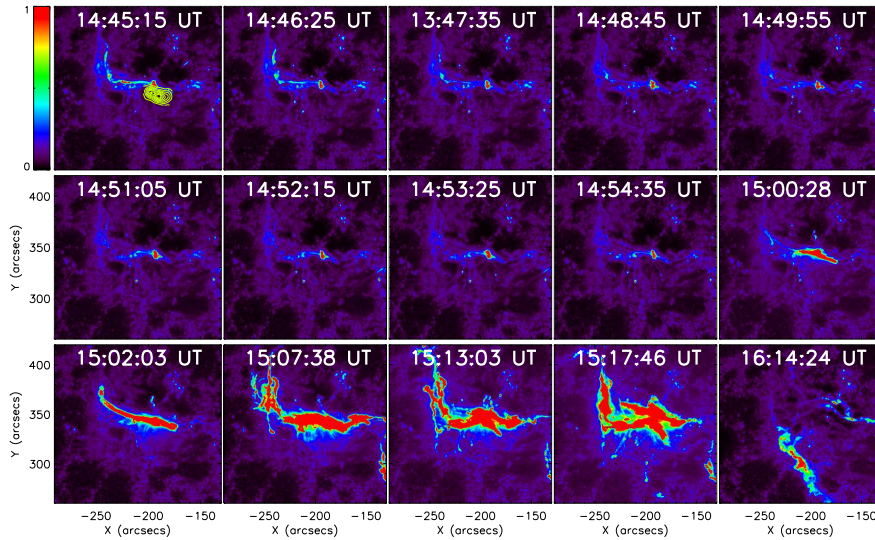


Figure 4.21: AR 9026 on June 6, 2000 as seen in 1600Å by *TRACE*. The X2.3 solar flare began at 14:58 UT, peaked at 15:25 UT and ended at 15:40 UT. Contour plots of the 6 mHz egression power at 15:05 UT, indicating the location of the seismic transient at the photospheric level, are shown in the first frame.

At 15:13:03 UT the 1600Å signature splits into two ribbons, which will be  $\sim 50$  arcsec apart one hour later. Unfortunately, we have no *TRACE* data from 15:17:47 UT to 16:14:24 UT (Figure 4.21) to be able to follow the evolution of the flare ribbons. Figure 4.21, as all following Figures, has the color bars plotted on the top left side of the first map.

This event is associated with a filament eruption. Deng et al. (2005) discussed this event in detail and found two penumbral areas that very obviously decayed right after the flare. Also from our WL analysis, we can see the WL image near flare maximum is presented at the position of the UV *TRACE* kernel and of the seismic source. Interestingly, the AR 9026 not only hosted a powerful sun quake, but also suffered catastrophic decay of the central  $\delta$  spot region from 10:00 UT of June 6 to 16:00 UT of June 7 (Liu et al., 2005).

Figure 4.22 shows the AR 9415 active region observed during **April 6, 2001**. This region was excited by a solar flare of magnitude X5.0-type occurring at 19:10 UT and ending at 19:31 UT. In this case we could identify a double source in 1600Å starting at 19:10 UT and reaching a maximum at 19:13 UT – the beginning of the sun quake. *TRACE* did not observe the active region in 1600Å from 19:13 to 20:03 UT, in this line. Therefore we cannot say for sure whether the flare signature evolved into a two ribbon structure. However, the spatial coincidence of the two seismic signatures (as shown as contour plots of the 6 mHz egression power signature in the first frame of Figure 4.22) with the 1600Å features is easily noticeable.

Figure 4.23 shows the X3.0 flare of **July 15, 2002** (beginning 19:59 UT, maximum 20:08 UT, end 20:14 UT). The *TRACE* 1600Å kernel that is above the acoustic emission seems to be already excited around 19:40 UT and fades away by 19:56 UT, about four minutes before the maximum of the sun quake. In the first frame of Figure 4.23 contour plots of the egression power maximum from 20:00 UT are overplotted.

This flare looks like a two ribbon flare, but with stationary ribbons.

Figure 4.24 shows the 1600Å emission during the **October 29, 2003** X10 flare. Again we can observe the evolution of two ribbons moving away from each other starting around 20:41 UT. The maximum acoustic emission contours at 20:45 UT are shown in the first frame of this Figure.

Note the north-western structure which resembles to the sun quake and appears about two minutes before the start of this sun quake.

Figure 4.25 shows the last flare covered by *TRACE*'s 1600Å line, the **January 15, 2005** X1.2 flare (start 00:22 UT, max 00:43 UT, end 01:02 UT).

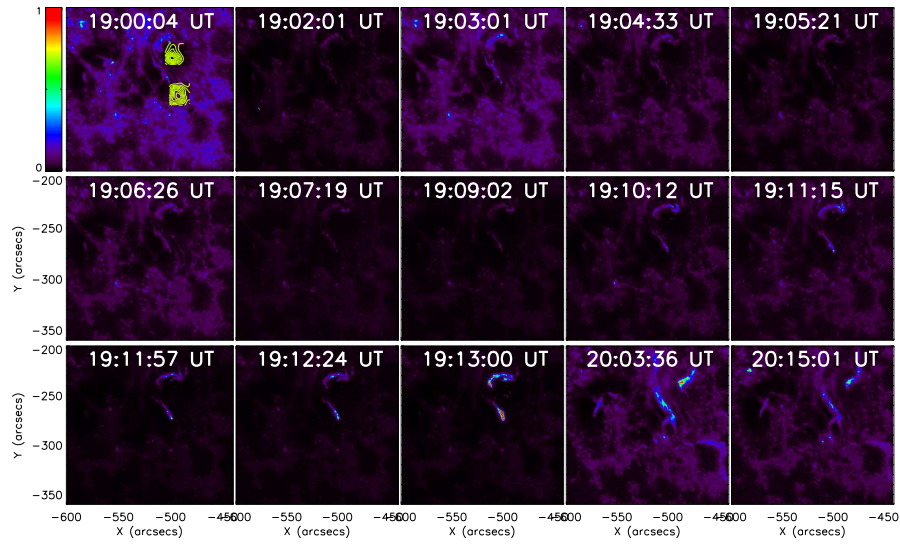


Figure 4.22: AR 9415 on April 6, 2001 as seen in  $1600\text{\AA}$  by *TRACE*.

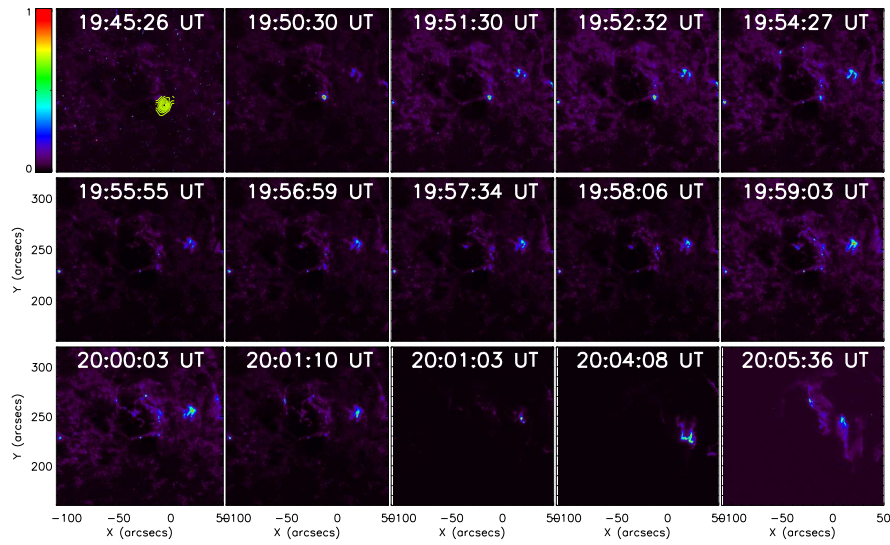


Figure 4.23: AR 10030 on July 15, 2002 as seen in  $1600\text{\AA}$  by *TRACE*.

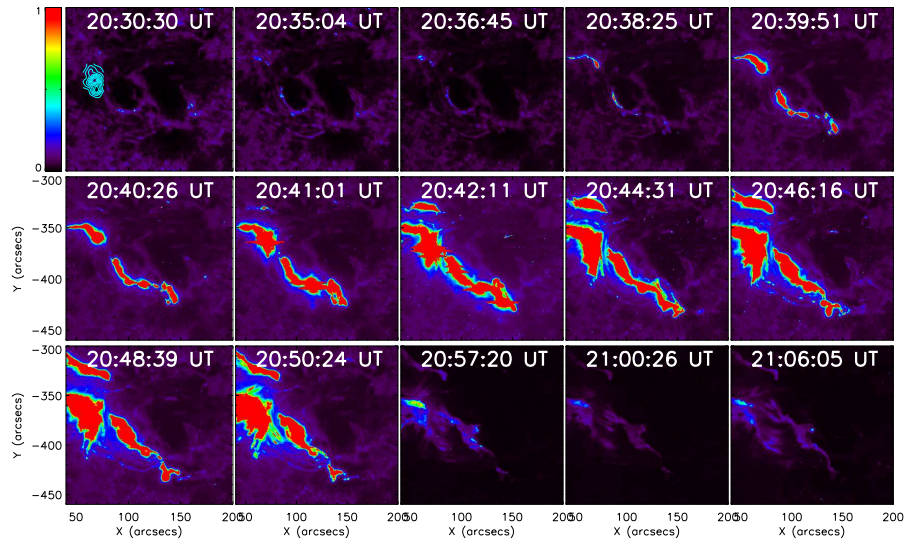


Figure 4.24: AR 10486 on October 29, 2003 as seen in  $1600\text{\AA}$  by *TRACE*.

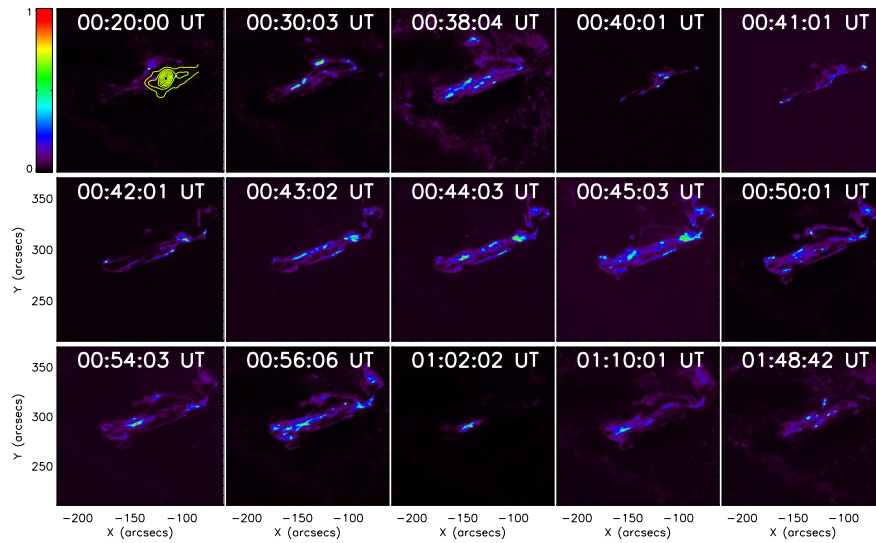


Figure 4.25: AR 10720 on January 15, 2005 as seen in  $1600\text{\AA}$  by *TRACE*.

The entire chromosphere above the sun quake erupted around 00:30 UT (three minutes before the start of the sun quake) saturating the images after 00:40 UT. The contours shown in the first frame of Figure 4.25 represent the 10%, 30%, 50%, 70% and 90% levels (the same levels as all previous Figures) of the sun quake's maximum at 00:41 UT.

In conclusion, all the excess UV emission in flares generating sun quakes starts a few minutes before the generation of seismic sources. This clearly shows that the energy perturbation from the flare site propagates through the upper layers of the atmosphere and in a few minutes reaches the photosphere. For all the events, we find that the locations of UV kernels are related to flare emission and are connected to the seismic emission.

## 4.5 Results of analysis of NaDI and $H\alpha$ Data

NaDI data has proven to be a very powerful tool for diagnosing low chromospheric emissions. Usually one would use the  $H\alpha$  line for such studies. The inconvenience is that the *ISOON* camera for the  $H\alpha$  line saturates after about 4000 counts. Therefore we have computed a Doppler interpretation of the NaDI and  $H\alpha$  emissions. Assuming that we have a complete set of data, which includes line centre, blue and red wing we intend to show velocities and their directions during the flare.

In a flare, different parts of a line can be in absorption or emission, a result of the different components of the medium having different source functions. On the other hand, nearly all flare models incorporate sufficient thick-target heating of the chromosphere that the source function is enhanced in the heated layer. This, invariably entails a line that is weaker in absorption during the flare than in the pre-flare condition. Hence, the difference in the line profiles is invariably in emission.

$$\Delta I_{r/b} = I_{r/b}(\text{flaring}) - I_{r/b}(\text{pre-flare}) \quad (4.2)$$

The relative intensity variation will depend linearly on the wavelength increment  $\delta\lambda$  if this is small compared to the line width:

$$\frac{\delta\Delta I_{r/b}}{\Delta I_{r/b}} = \pm\alpha \delta\lambda_{r/b} \quad (4.3)$$

where  $\alpha$  is some proportionality constant. This means, if  $I_r = I_b$ , and the line is symmetrical, so that  $dI_r/d\lambda = -dI_b/d\lambda$  for the unshifted line, then

$\Delta I_r + \Delta I_b$  should be null ( $I_r + I_b$  unchanged), while  $\Delta I_r - \Delta I_b$  should be  $2\alpha\delta\lambda$ . From this, it follows that

$$\frac{\Delta I_r - \Delta I_b}{\Delta I_r + \Delta I_b} = \alpha \Delta\lambda_0 \quad (4.4)$$

If  $\delta\lambda$  is comfortably smaller than the line width, than the difference between  $\Delta I_r$  and  $\Delta I_b$  should be comfortably less than the average of the two. This difference, plotted below along a horizontal line passing through the most intense part of the flare in its impulsive phase, suggests that the linear approximation will be reasonably accurate.

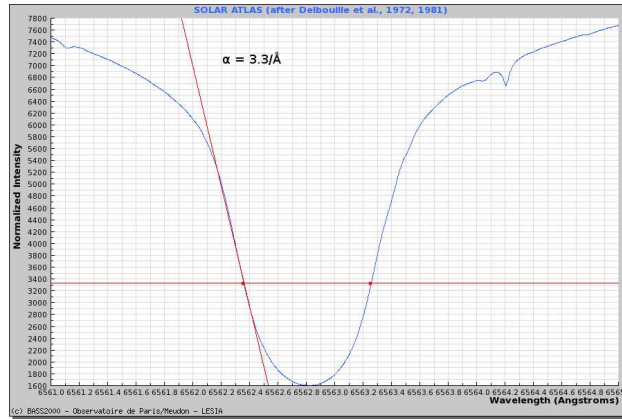


Figure 4.26: The quiet-Sun  $H\alpha$  spectral profile taken from the *BAAS 2000* on-line solar spectrum.

For an estimate of  $\alpha$  let us take the slope of the quiet-Sun  $H\alpha$  profile at the wavelength,  $\lambda_r$ , at which the *ISOON* red-wing filter is centred, bearing in mind that this line is in absorption. The presumption is that the core of the emission line will have the same profile. This is admittedly an approximation. The quiet-Sun  $H\alpha$  spectral profile taken from the *BAAS 2000* on-line solar spectrum (Figure 4.26) is shown below: the slope,  $\alpha$ , is that of the red diagonal line tangent to the point at which the red wing of the *ISOON* filter is fixed normalized to the intensity at that point. This is  $\sim 3.3 \text{ \AA}^{-1}$ .

To relate the ratio expressed in equation 4.4 to an actual velocity, we note that

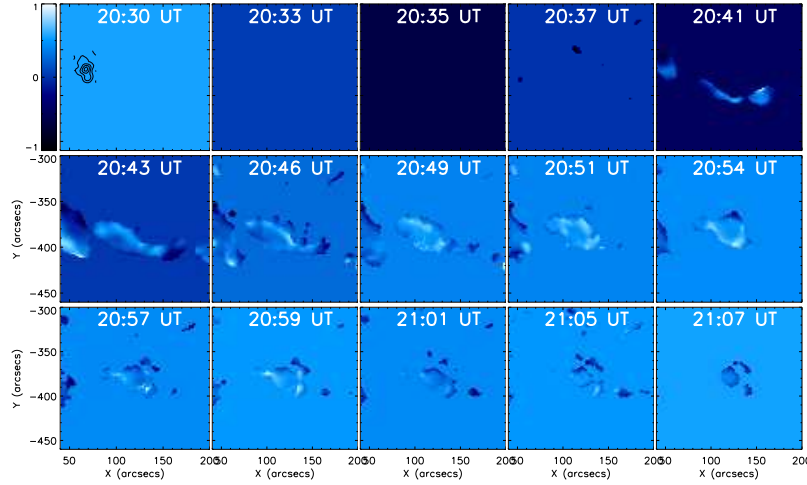


Figure 4.27: Doppler maps of the NaDI emission for the October 29, 2003 sun quake. Overplotted in the first frame are the contour levels of the seismic maximum emission from 20:45 UT.

$$\frac{v}{c} = \frac{\Delta\lambda}{\lambda_0} \quad (4.5)$$

where  $\lambda_0$  can be taken as the wavelength of line centre for any precision we could conceivably approach. Thus,

$$v = \frac{c}{\alpha\lambda_0} \frac{\Delta I_r - \Delta I_b}{\Delta I_r + \Delta I_b} \quad (4.6)$$

The applicability of equation 4.6 depends on the assumption that the medium causing the flare signature manifests a significant emission profile. Hence, when  $\Delta I_{r/b}$  are not significantly positive, the ratio on the right side of equation 4.6 becomes treacherous. The following figures map the representation of  $\langle v \rangle$  in equation 4.6 for all pixels for which the denominator is greater than 500 counts.

Figure 4.27 shows the Doppler maps for the acoustically noisy flare of **October 29, 2003** obtained using the *ISOON* NaDI data. All 15 frames are centred on the AR NOAA 10486 and have specific times on top of each frame. The central three frames on the first row appear blank because there are no intensity increments greater than the 500-count threshold imposed

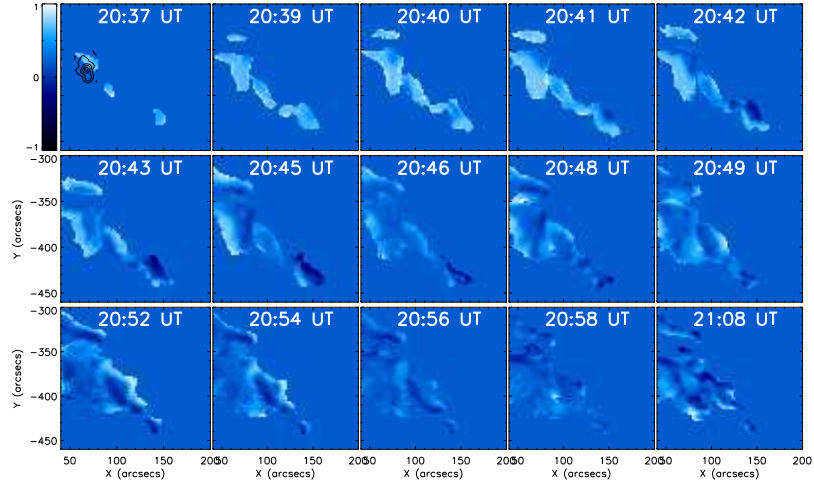


Figure 4.28: Doppler map of the  $H\alpha$  emission for the October 29, 2003 sun quake. Same contour plots shown as in Figure 4.27.

with the analysis. Starting at 20:41 UT there is a mostly positive transient – motions towards the photospheric level. Two minutes before the maximum of the sun quake there is an important motion of plasma above the seismic source.

Figure 4.29 shows the Doppler maps for the acoustically noisy flare of **July 16, 2004** obtained using the *ISOON*  $H\alpha$  data. Overplotted in the first frame on the first row are the contour levels of the egression power maximum as seen in Figure 3.28.

We can see the first noticeable variations of chromospheric velocities right above the seismic source as motion towards the photosphere starting at 13:48 UT, practically at the same time as the beginning of the seismic emission and the X-ray flux. Starting at 13:50 UT we can also see some upwards movements at the edge of the signature above the acoustic source. With this central feature expanding and enhancing its emission (starting at 13:51 UT) there is another one flaring a few degrees eastwards. However, our concern is focused on the central part of the main flaring region (around  $-500''$ ,  $-220''$ ) which shows significant downwards motion during this flare. The mean values integrated over this central feature during the flare have positive values ranging from 0.5 to 2 km/s, showing that the plasma is moving

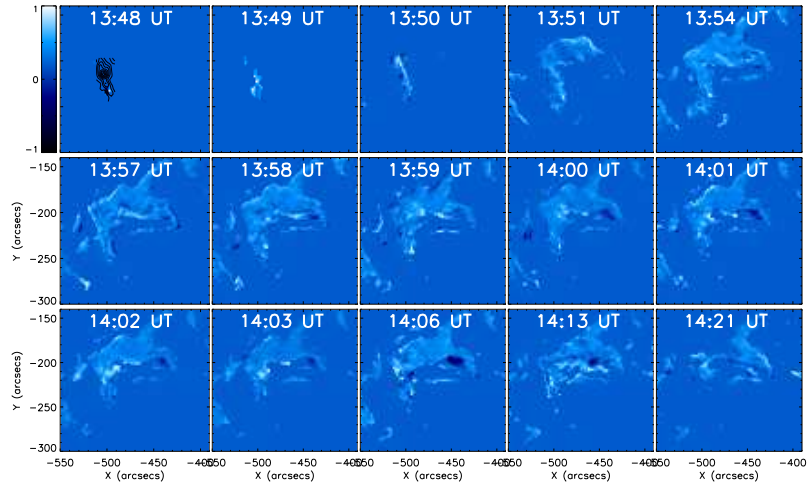


Figure 4.29: Doppler maps of the  $H\alpha$  emission for the July 16, 2004 sun quake. Overplotted in the first frame are the contour levels of the seismic maximum emission from 13:57 UT.

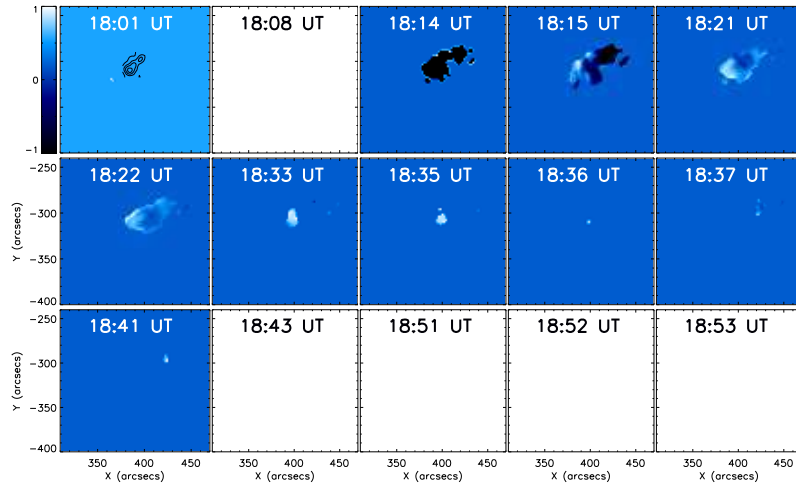


Figure 4.30: Doppler maps of the  $H\alpha$  emission for the August 13, 2004 sun quake. Overplotted in the first frame are the contour levels of the seismic maximum emission from 18:12 UT.

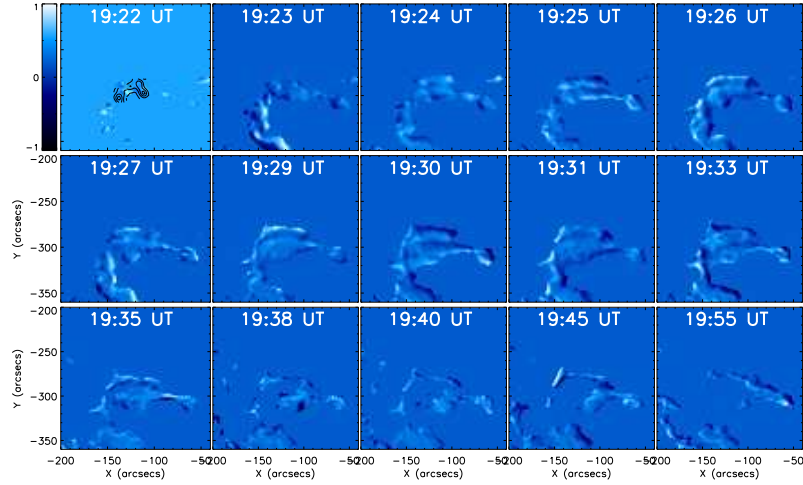


Figure 4.31: Doppler maps of the  $H\alpha$  emission for the September 13, 2005 sun quake. Overplotted in the first frame are the contour levels of the seismic maximum emission from 19:22 UT.

mostly towards the photospheric level.

Figure 4.30 shows the Doppler maps for the seismic emission during the **August 13, 2004** flare, obtained using the *ISOON*  $H\alpha$  data. This flare lacks the same time resolution as the previous flare, during this short flare (eight minutes) and covers the ascending phase only by two minutes 18:01 and 18:08 UT. The Doppler velocity map at 18:08 UT seems blank, as well as the last four frames on the third row of Figure 4.30, because there are just a few pixels with more than 500 counts. However, the mean Doppler values during the X-ray flux are positive. After 18:14 UT we can see the plasma moving away from the chromospheric level, and a few kernels of plasma going down later on.

Figure 4.31 shows the Doppler maps for the seismic emission during the **September 13, 2005** seismic emission. The  $H\alpha$  emission during this flare is much more extended than the seismic source, but we will concentrate on the central-north region.

Over the first minutes of the flare there is a two-ribbon structure developing with the same characteristics as the previous flare, that is positive mean values over the seismic region. Starting at 19:25 UT in addition to

the still strong downwards plasma motion, there are some strong signatures of plasma going away from the chromospheric level, but the preponderant motion remains the downwards one throughout the entire seismic emission.

To date this sun quake is the only one associated with an observed Moreton wave. Discovered by [Moreton \(1960\)](#) this type of waves can be seen in H $\alpha$  as disturbances in the chromosphere following some flares moving at speeds as fast as 2500 km/s.

We can conclude that all sun quakes show downward plasma motion from the chromospheric level towards the photosphere, very well spatially correlated with the location of the seismic emission.

## 4.6 Results of analysis of EUV TRACE and SOHO-EIT Data

Going upwards in the atmosphere, the Fe lines seemed a good choice to study the coronal loops as *TRACE* and *SOHO-EIT* covered seven seismic flares at wavelengths of 171Å and 195Å.

We are looking for information about the loops and a relationship between the footpoints of the loops and the sun quake.

Figure 4.32 shows the excess emission in the 171Å line during the **June 6, 2000** flare, showing the location of the bright coronal loops. The loops above the AR NOAA 9026 are very twisted and confined, igniting sometime around 14:54 UT and showing a bright kernel above the seismic emission starting around 15:01 UT, four minutes before the maximum of the sun quake. Its brightness increases until 15:06 UT, after which most of the loops are excited. Everything seems to cool down after 15:11 UT.

According to [Kurokawa et al. \(2002\)](#) the emerging twisted magnetic flux rope observed in NOAA AR 9026 can well explain almost all evolutionary features of the  $\delta$  sunspot region which hosted the seismic flare. [Fisher et al. \(2000\)](#) theoretically discussed similar highly twisted and kink-unstable flux tubes to produce a  $\delta$ -type sunspot. The twisted flux rope rose to high atmospheric levels, where sheared magnetic lines began to develop because of the kink instability. It seems that for the June 6, 2000 flare the magnetic reconnection occurred in the photosphere and accelerated the emergence and reconnection of the magnetic field to trigger the big flares of AR 9026. Remarkably, the seismic event of this active region was accompanied by a catas-

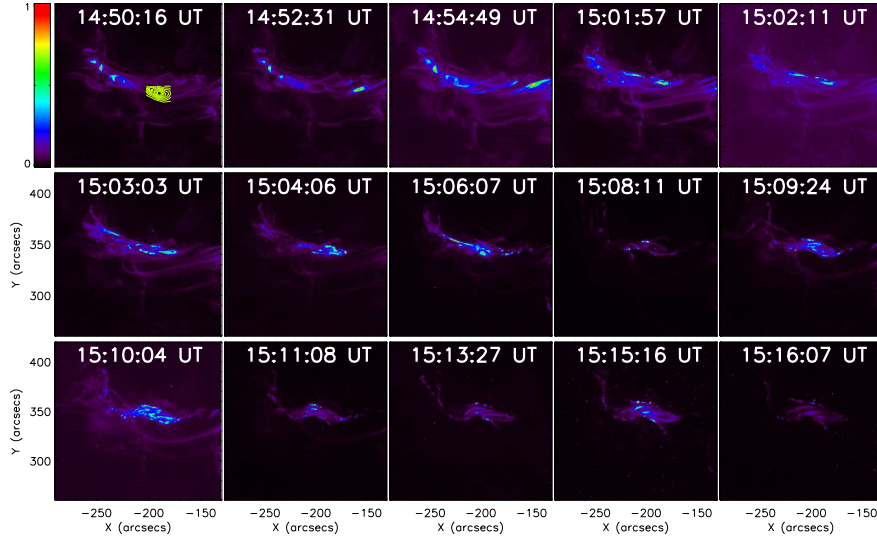


Figure 4.32: The flare of June 6, 2000 as seen by *TRACE*'s 171Å line.

trophic decay of the sunspot region observed from 10:00 UT of June 6 to 16:00 UT of June 7. Also, the seismic source is located very close to the western footpoints of the twisted loops.

Figure 4.33 shows the coronal loops evolution during the **April 10, 2001** flare. The 6 mHz seismic source is shown by the contour plots in the first frame in Figure 4.33, and seems to be situated at the footpoint of some low-lying small bunch of magnetic loops. We identified the hottest part of the flaring loop being just above the seismic signature.

Figure 4.34 shows 10649 AR during the acoustically active flare of **July 16, 2004**. This sun quake is clearly located at the footpoints of the flaring loops. Unfortunately we did not have data before 13:48 UT when the loops had already been ignited. There is a striking resemblance between the temperature distribution in these loops and the morphology of the seismic source. Again, these loops seem very confined and low lying.

Figure 4.35 shows NOAA 10656 AR during the **August 13, 2004** flare. We can observe the same proximity of the seismic source to one of the footpoints, the north-western one.

Figure 4.36 shows NOAA 10656 AR during the **August 14, 2004** flare, the second acoustically active flare above this region. The flaring loops in

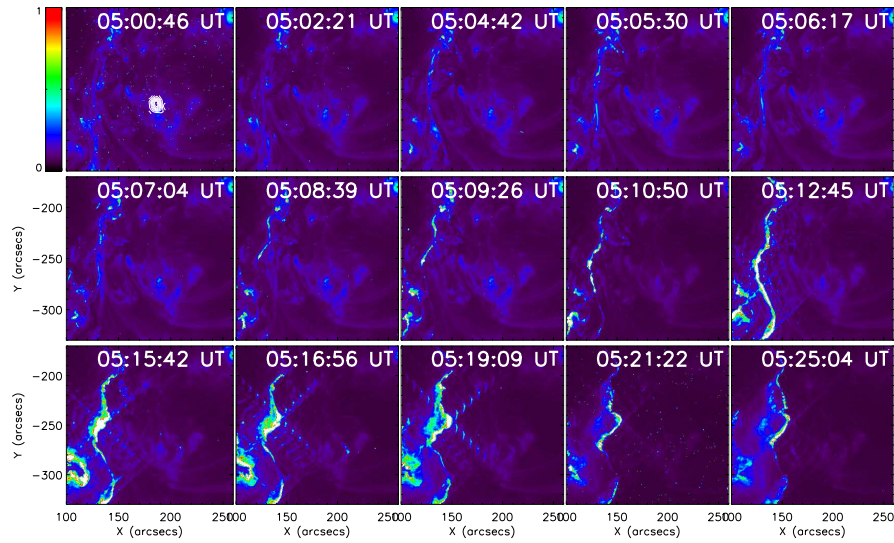


Figure 4.33: The flare of April 10, 2001 as seen by *TRACE*'s 171Å line.

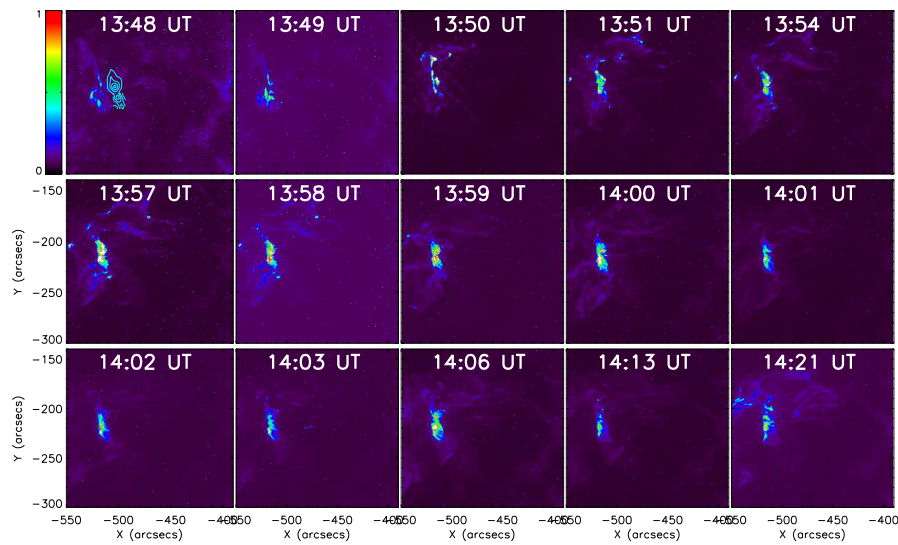


Figure 4.34: The flare of July 16, 2004 as seen by *TRACE*'s 171Å line.

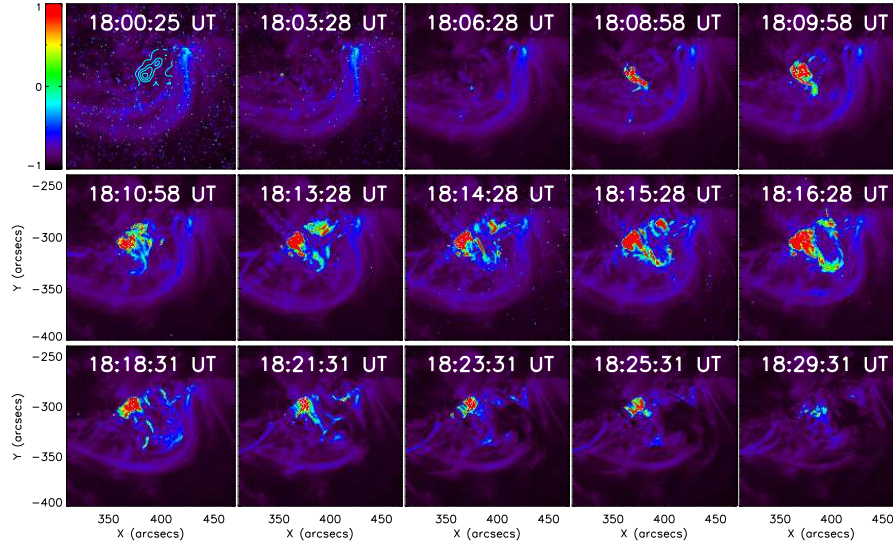


Figure 4.35: The flare of August 13, 2004 as seen by *TRACE*'s 171Å line.

this case ignite around 05:39 UT, five minutes before the maximum of the sun quake. The western footpoint of the loops seen above this region is spatially coincident with the seismic source, for which the contour plots are seen in the first frame of Figure 4.36. We can observe the same spatial correlation as seen for the other sun quakes, between the hottest structures in the flaring loops and the acoustic source.

Figure 4.37 shows NOAA 10656 AR during the **August 15, 2004**. The loops seem to ignite around 12:37 UT, about three minutes before the maximum of the seismic emission. The August 15, 2004 sun quake resides at the north-western footpoint of the flaring loops.

Figure 4.38 shows the corona flaring on **September 13, 2005**. The loops ignited sometime around 19:24 UT, two minutes before the maximum of the sun quake. The location of the seismic source is spatially correlated with the north-western footpoint of the loops.

In conclusion, all seismic sources are in the proximity of one of the flaring loops footpoints and the temperature distribution in the flare around the maximum of the acoustic emission resembles the shape of the seismic transient.

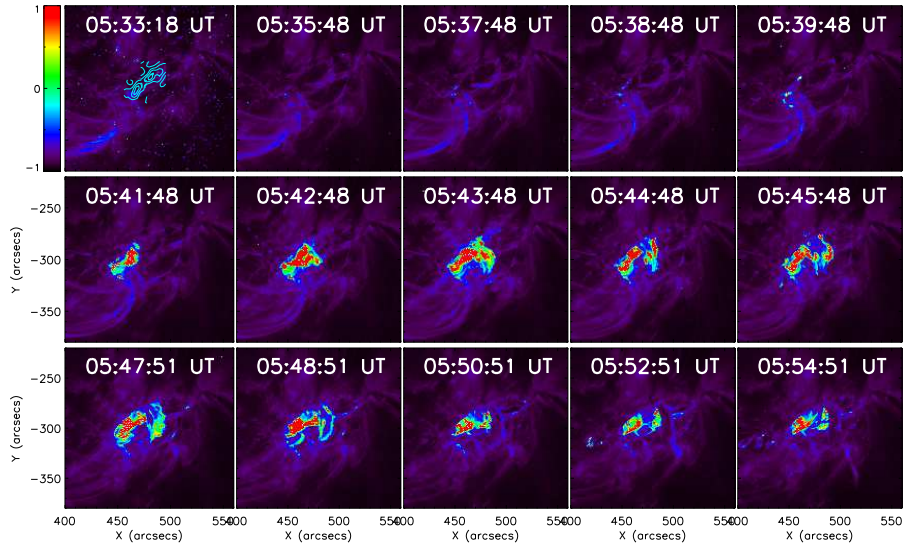


Figure 4.36: The flare of August 14, 2004 as seen by *TRACE*'s 171Å line.

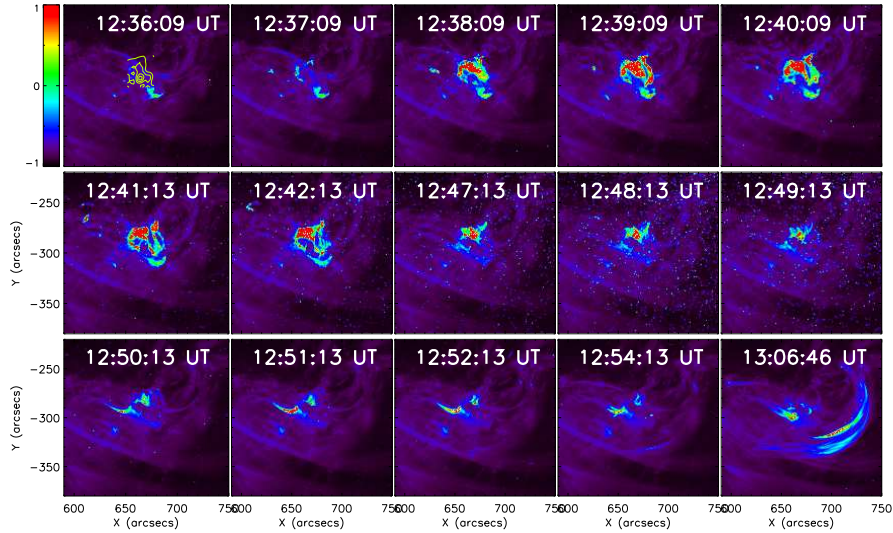


Figure 4.37: The flare of August 15, 2004 as seen by *TRACE*'s 171Å line.

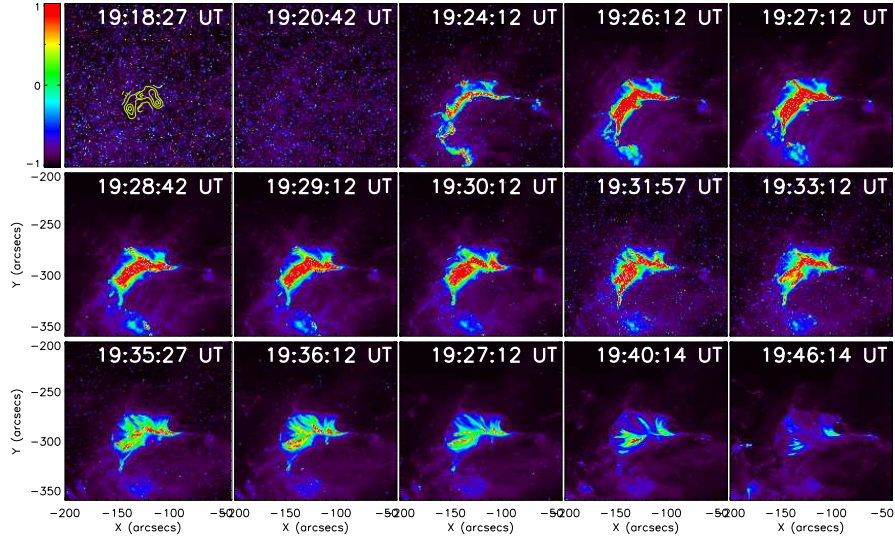


Figure 4.38: The flare of September 13, 2005 as seen by *TRACE*'s 195Å line.

## 4.7 Conclusions

The multi-wavelength analysis of sun quakes is a very powerful tool in understanding the response of the solar atmosphere and photosphere to seismically active flares. We want to understand what makes some of the flares so special, meaning why some flares can generate sun quakes and others cannot. The sudden energy release of a flare in the solar atmosphere has many consequences. We selected maps of intensity continuum, Dopplergrams and magnetograms from various instruments to image the photospheric responses to the flare excitation. We also looked at the UV,  $H\alpha$  and NaDI maps of the host active regions to analyse the reaction of the upper photosphere and the chromosphere to particle precipitation from flares. Two EUV lines at 171Å and 195Å were used to view the shape of flaring coronal loops. The main result of this study is that 15 sun quakes had excess white light continuum emissions associated with them.

A number of mechanisms have been considered as possible contributors to flare acoustic emission:

- (1) chromospheric shocks driven by sudden, thick-target heating of the

upper and middle chromosphere

Super-thermal particles accelerated at the top of magnetic loop follow magnetic field lines into the underlying chromosphere. The two downwards-propagating particle beams heat the upper chromosphere at the footpoints, evaporating a considerable mass of gas into the corona, and producing hard X-ray bremsstrahlung emission. The mass evaporation is massive and explosive. The reaction momentum from the explosive evaporation drives a radiative shock downwards through the chromosphere towards the photosphere. As the shock penetrates into the denser photosphere it weakens its relative amplitude and may reach the base of the photosphere with a local energy flux momentarily comparable to that of  $p$ -modes in some instances. Having penetrated the photosphere, this wave radiates acoustic energy downwards into the solar interior. The energy is reflected back to the surrounding solar surface over the following 30–60 minutes as an outwardly spreading acoustic disturbance. This is the scenario that was suggested for the first time by the discoverers of the first solar quake, [Kosovichev and Zharkova \(1998\)](#).

However, hydrodynamic modelling of waves driven by thick-target heating of the chromosphere indicates that these waves are heavily damped by radiative losses ([Fisher et al., 1985a,b,c](#); [Ding and Fang, 1994](#); [Allred et al., 2005](#)) calling into question whether a nearly sufficient amount of acoustic energy can possibly penetrate through the photosphere to explain what the helioseismic observations indicate is injected into the active region subphotosphere.

- (2) wave-mechanical transients driven by heating of the photosphere. This was initially suggested by [Donea and Lindsey \(2005\)](#) based on the strong spatial correspondence between sudden excess visible continuum emission emanating from active regions during the impulsive phases of flares and the source distributions of flare acoustic emission shown by seismic holography ([Donea et al., 1999](#); [Lindsey and Braun, 2000](#); [Donea and Lindsey, 2005](#)) applied to helioseismic observations of the flares.

Following the comprehensive survey in search for more sun quakes, our results show indeed the coincidence between the locations of sudden

white-light emission and seismic transient emission for the majority of the solar flares with seismic activity. This suggests that a substantial component of the seismic emission is clearly a result of the sudden heating of the low photosphere (radiative back-warming).

We have seen that the white light emission usually appears on the penumbra of the hosting AR. Rarely, the WL signatures were prominent in plages near the sunspots.

We have also shown that 75% of the analysed associated WL temporal profiles show a sudden onset of one to two minutes. The rest of flares generating seismic disturbances had onset times evolving over three-five minutes. This conclusion is consistent with the model where one assumes that the seismic events are associated with the chromospheric heating.

The origin of white-light emission would have to be entirely in the chromosphere, where energetic electrons dissipate their energy (Metcalf et al., 1990b; Zharkova and Kobylinskii, 1991, 1993) mainly by ionizing previously neutral chromospheric hydrogen approximately to the depth of the temperature minimum. It appears that the low photosphere itself would be significantly heated as a secondary effect. This is largely the result of Balmer and Paschen continuum edge recombination radiation from the ionized chromospheric medium, approximately half of which we assume radiates downward and into the underlying photosphere. Chen and Ding (2006) also affirm that the white-light flare signatures highlight the importance of radiative back-warming in transporting the energy to the low photosphere when direct heating by beam electrons is impossible.

Amazingly, one of the most spectacular solar flares, the July 14, 2000, Bastille Day solar flare, was seismically quiet. The Bastille day flare occurred near the peak of the solar maximum. Active region 9077 produced the X5-class flare, which caused an S3 radiation storm on Earth (NASA. 2004-07-14) fifteen minutes later as energetic protons bombarded the ionosphere. It was the biggest solar radiation event since 1989. The proton event was four times more intense than any previously recorded since the launches of *SOHO* in 1995 and *ACE* satellite in 1997. Moreover, the flare was followed by a full-halo coronal mass ejection.

Conversely, a modest flare, such as the **December 2, 2005** M7.8-type flare, did generate visible seismic waves on the photosphere, as shown in Section 4.2.2.

The most spectacular aspect of sun quakes, the seismic waves, are rarely seen. Only four solar flares observed using the time distance technique displayed ripples after an acoustic emission. As main characteristics: the waves usually appear on the photosphere some 15–20 minutes after the detection of the sun quake and the shape of the front wave follows the shape and direction of the acoustic source.

The position of the seismic transients generally is very well correlated with the region where magnetic transients occurred. Clearly, the sun quakes are accompanied by magnetic transients in the hosting areas. Whether they are depositions or depletions of magnetic energy, or short variations in the time profiles, all magnetic variations are easy to observe. The general view is that the seismic sources appear in the regions where the magnetic field is inclined.

We draw our attention to one case, where despite the existence of significant magnetic transient signatures in the flare of July 14, 2000 there was no significant seismic emission emanating from this flare. Nevertheless, if magnetic transient forces can, even only occasionally, drive seismic emission of the character shown by the helioseismic observations into active region sub-photospheres, the implications respecting the reconnection process for those instances will be major.

A treatment of magnetic signatures similar to that applied to continuum intensity signatures shown in Section 4.3 will help identifying a third cause that may contribute to the generation of seismic sources. [Hudson et al. \(2008\)](#) proposes that the so called “magnetic jerks” produced by the coronal restructuring might be the trigger for the seismic waves, a mechanism also supported by [Lindsey and Donea \(2008\)](#). There is also significant work that proposed a direct link between magnetic transients and seismic sources observing the evolution of the magnetic field during the seismic emission ([Kosovichev and Zharkova, 2001](#); [Zharkova and Kosovichev, 2002a](#); [Donea et al., 2006b](#)). However, this mechanism is not yet well understood. We expect data from the *HMI* instrument on the *SDO* mission to yield better understanding of flare-associated magnetic field changes, since vector magnetograms (instead of the line-of-sight magnetograms from *SOHO/MDI*) will be provided. These new data will allow us to expand upon the work in Section 4.3 to understand the role of magnetic field changes during flares.

From the *TRACE* 1600Å observations, in UV line, we have learnt that the low chromospheric plasma flares fairly quickly, and shows similar evolution as the white light excess emission. [Mrozek et al. \(2007\)](#) state that impulsive brightenings observed with the *TRACE* 1600Å filter are dynamic and that their character suggests that the reaction in UV is produced directly by the non-thermal electron beams. The signatures of the UV emissions are, therefore, further evidence for strong chromospheric heating. However, [Metcalf et al. \(2003\)](#) state that the electron beam does not need to penetrate to the lower chromosphere, since the energy is transported to the lower atmosphere via back-warming ([Metcalf et al., 1990a,b](#)).

There are several types of motions on the solar surface. The largest contributions of 500 m/s come from the stochastic 5-minute oscillations excited by convection. The amplitude of the flare-generated seismic waves (ring-like features) rarely exceeds 100 m/s. Thus, because of the strong stochastic motions in the background, these waves are difficult to detect. Therefore observations of NaDI and H $\alpha$  of the flaring AR can help us understand that all seismic transients are accompanied by a downwards plasma motion from the chromospheric level towards the photosphere.

As all Doppler velocity maps obtained from the NaDI and H $\alpha$  also show some upward moving plasma (that is towards the corona) we believe this to be proof of the chromospheric evaporation (or physically correct: chromospheric ablation). However, this upwards movement usually is more noticeable after the peak of the flare, while at the beginning the predominant characteristics is the downwards movement of the plasma.

Following the analysis of the *TRACE* 171Å and 195Å data, we have concluded the following: the EUV lines show coronal loops usually forming across the magnetic separatrix. The seismic sources are spatially correlated with one of the footpoints of the flaring coronal loops. [Moradi et al. \(2007\)](#) and [Martinez-Oliveros et al. \(2008b\)](#) compared the seismic source morphology for the January 15, 2005 flare with other supporting observations. They emphasized the spatial coincidence between the strong compact acoustic source and signatures of hard X-ray emission, suggesting that the high-energy electrons played an important role in triggering the seismic event.

[Mrozek et al. \(2007\)](#) suggests two main effects forming the EUV brightenings, namely the non-thermal electron beam that is responsible for the fast occurring maximum of EUV radiation and the thermal front connected with a nearby layer having temperatures about  $10^7$  K, that would support our previous theoretical interpretations. Therefore, we agree with [Li et al. \(2002\)](#)

that plasmas with very different temperatures can coexist and stay relatively stable in an ejection. This may have an important effect in distributing the flare energy downwards into the chromosphere. For a precise determination of the triggering factors one would need a multi-wavelength study using data with resolutions as small as just seconds.



# Chapter 5

## Spectral Hardness

Solar white-light flares (WLF) are energetic events visible in the optical continuum. Recently, WL continuum has also been associated with solar flares of C-class (Jess et al., 2008). In the regime of small flares, low-energy (less than 20 keV) electrons cannot reach the upper chromosphere easily. Therefore, for these events to demonstrate WL emission, a common consensus is to consider that the energy transportation from the upper chromosphere to the photosphere is efficiently done via the back-warming effect (Machado et al., 1989). Indeed, Allred et al. (2005) demonstrate dramatic increases in optical continuum emission during the impulsive stage of simulated flares. Furthermore, seismic emission as a flare-induced mechanism needs according to Donea et al. (2006b), only a very small fraction of the energy delivered into the photosphere (by particles or back-warming) to generate a seismic event. This is also suggested by the time profiles of the solar flare emission in various wavelength bands. Fletcher et al. (2007) investigated the formation of the white-light continuum during solar flares and its relationship to energy deposition by electron beams inferred from hard X-ray emission. In addition, the similarities in time and space of these observations with the seismic emission from acoustically active flares strongly link sun quakes to non-thermal processes occurring in the early impulsive phases of a flare. Sun quakes are generally produced by WLF.

For example, the strong similarity between the morphology of the acoustic kernels of the seismic transient and the white light intensity power kernels of the solar flare of January 15, 2005 (Moradi et al., 2007) suggested that a clue to understand the formation of sun quakes should be found in the behaviour of the spectral hardnesses of the white light spectrum and acoustic

emission. During the impulsive phase, the white light emission as well as the acoustic emission from flares becomes harder (more energy is pumped into the high frequencies). The seismic sources oscillate with most of their energy emanating at 6 mHz.

In this section we map the 5–7 mHz continuum intensity-excess power and holographic egression power for some of the acoustically active flares. One of the goals of our work is to examine the spatial relationships between WL and acoustic emission. We also calculate the intensity continuum excess power and compare the flare energy budgets implied by the WL emission and the acoustics of the source.

We also investigate the relation between the hardness ratio inferred from WL continuum and Dopplergram maps. For example, the intensity continuum hardness (or the hardness ratio) is given by the ratio of the intensity continuum power at 6 mHz and 3 mHz. Sometimes this is defined as the ratio between the difference and the sum of intensity powers in the two frequency bands. The acoustic spectral hardness is the ratio of the energies estimated to be released into the photospheric level by the egression power during the maximum of the seismic event at 3 and 6 mHz.

It is possible to apply essentially the same spectral-analysis techniques to *GONG* intensity observations of active regions as those applied to the *MDI* Doppler images for helioseismic applications. The technique is described in detail in Section 2.4.

The Global Oscillation Network Group (*GONG++*) instruments measure the intensity maps of the full solar disk integrated over a  $\sim 0.75$  Å bandpass centred on the photospheric line NiI 6768 Å with a one-minute cadence. This line has a central absorption core strength of  $\sim 0.64$  and a full width at half strength of 0.11 Å (Debouille et al., 1973). The core of the NiI 6768 Å spectral line is thought to reach an optical depth of unity at  $\sim 250$  km above the base of the photosphere ( $\tau_{5000\text{Å}}^{\circ} = 1$ ) (Debouille et al., 1973).

In the next section we analyse the seismic transients with sun quakes that were covered with intensity continuum data from *GONG* and *MDI* instruments. If not specified otherwise, the results obtained for intensity spectral hardness are acquired using *GONG* data. The *GONG* continuum intensity maps were corrected for variations in smearing by the terrestrial atmosphere according to Lindsey and Donea (2008).

## High-frequency Continuum Spectrum of the November 24, 2000 flare

Figure 5.1 shows maps of the seismic event of November 24, 2000. The X2 type solar flare was covered by *SOHO-MDI's* high resolution data. Despite displaying a weak seismic signature, this flare is interesting to study because of its high resolution intensity continuum observations.

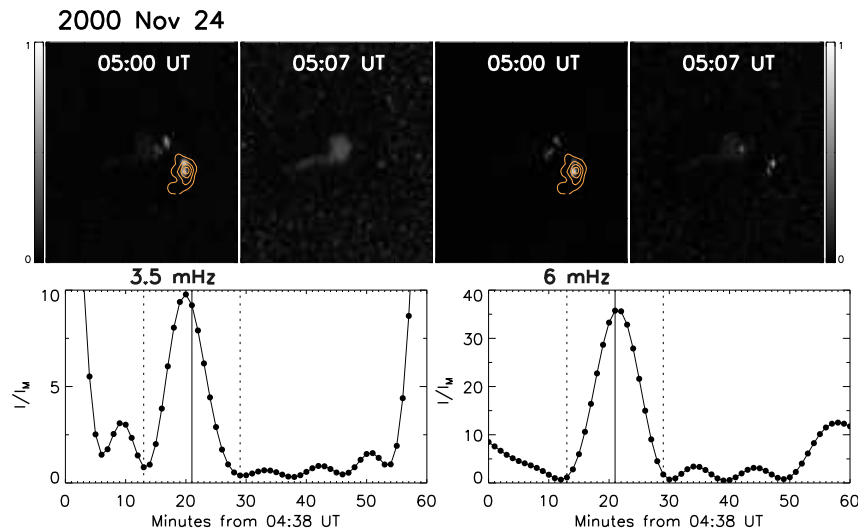


Figure 5.1: Comparison between 2.5–4.5 mHz (left frames) and 5–7 mHz (right frames) continuum intensity-excess power and holographic 6 mHz egression power (contour plots) of the November 24, 2000 solar flare. Second row shows temporal profiles of the normalized continuum intensity-excess power at 3.5 mHz, and 6 mHz. The vertical line gives the time when the continuum intensity (averaged over the area of the seismic source) has a maximum power at 6 mHz. Dotted vertical lines mark a time interval of  $\pm 8$  minutes around this maximum.

The first row in Figure 5.1 shows snapshots of the intensity continuum power at 3.5 mHz (first two frames) and at 6 mHz (last two frames) at the times specified in the figure. The times correspond to the moment when the acoustic source developed to its maximum value and seven minutes later. Overplotted are contour levels of the 6 mHz egression power signature at its maximum emission.

On the second row of Figure 5.1 we see the temporal profiles of the 2.5–4.5 mHz (left frames) and 5–7 mHz (right frames) continuum intensity-excess power integrated over the seismic source area, with the excess emissions exceeding the background by a factor of ten and thirty-five, respectively.

The vertical continuous line, plotted in all figures in this section, shows the time when the seismic source reaches its maximum 5–7 mHz emission, 05:00 UT in this case.

We have read the maximum value of the continuum intensity-excess power  $I_M$  at the location of the seismic source (one pixel). Then, the continuum intensity-excess power,  $I$ , averaged over the seismic source area is normalized to  $I_M$  for every minute.

The maps in Figure 5.1 shows the excellent spatial and temporal correlation between seismic source and the intensity continuum power signature.

A similar analysis was applied to all detected seismic sources where WL images were available. The next section displays the images for each sun quake.

## Continuum Emission in Other Acoustically Active Flares

The properties of the solar flare of September 9, 2001 are largely discussed by Donea et al. (2006b). Here we mention the main results of this work, changing the perspective to the hardness analysis. The intensities of the kernels that appear in Figures 5.2 reach a maximum excess of 8% of the quiet-Sun intensity. The local irradiance  $I$  integrated over the quake region underwent an increase of 2.5% of its pre-flare value of 0.452 Watt/m<sup>2</sup> at 20:42 UT in the succeeding minute to 0.463 Watt/m<sup>2</sup> at 20:43 UT, followed by a relaxation over the succeeding six minutes.

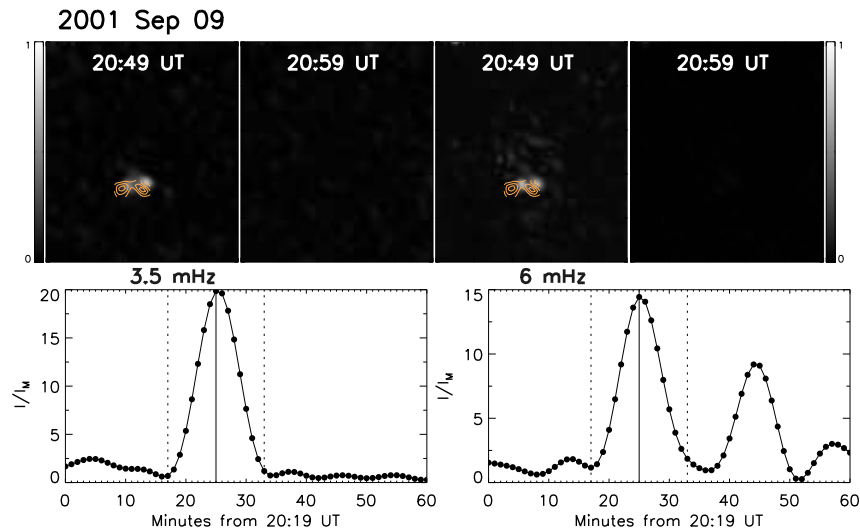


Figure 5.2: Continuum intensity-excess power maps and time profiles for the September 9, 2001 sun quake. Same as Figure 5.1.

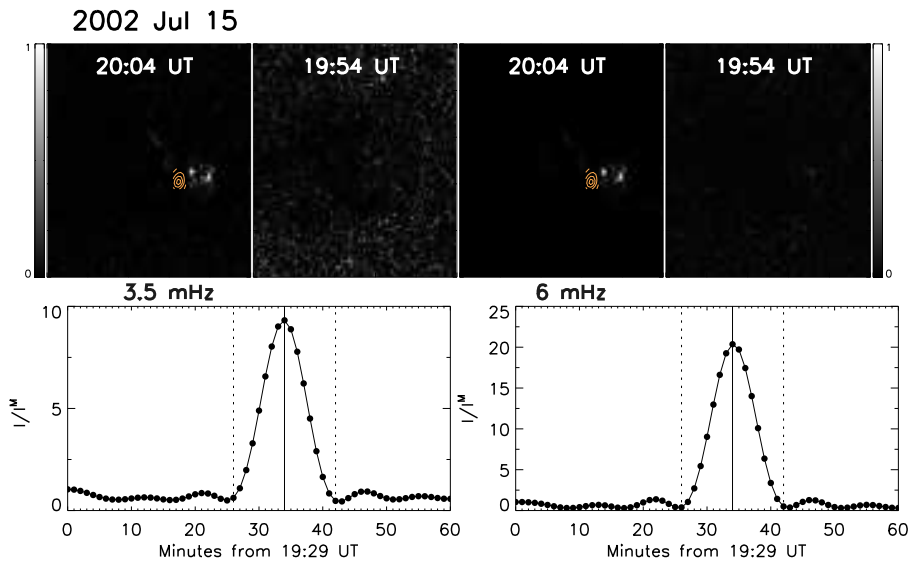


Figure 5.3: Continuum intensity-excess power maps and time profiles for the July 15, 2002 sun quake. Captions are similar to Figure 5.1

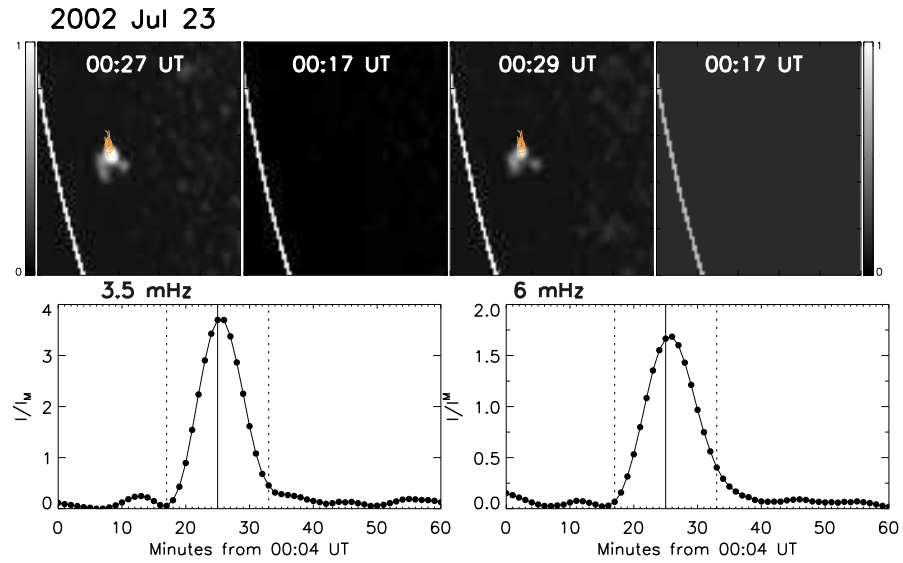


Figure 5.4: Continuum intensity-excess power maps and time profiles for the July 23, 2002 sun quake. Captions are similar as in the Figure 5.1

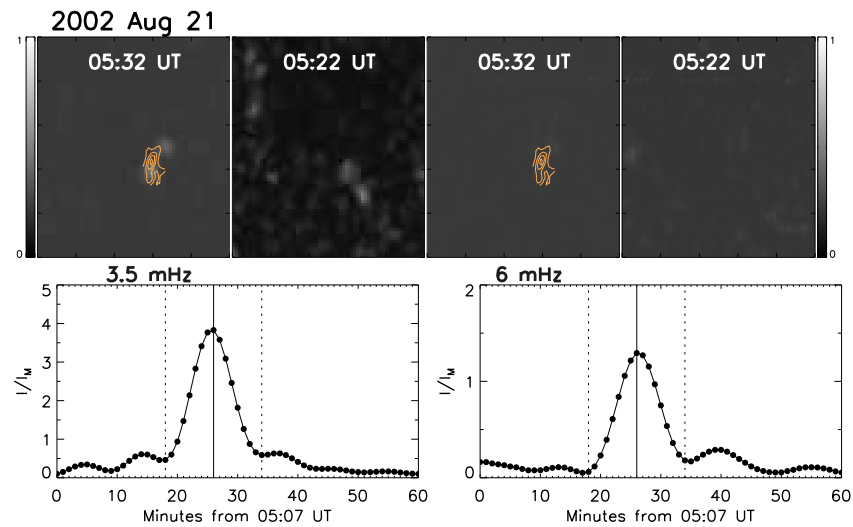


Figure 5.5: Continuum intensity-excess power maps and time profiles for the August 21, 2002 sun quake. Captions are as in Figure 5.1

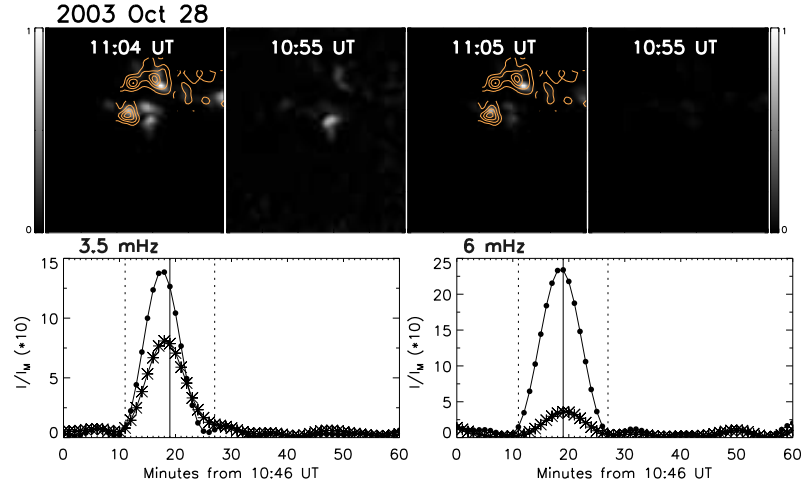


Figure 5.6: Continuum intensity-excess power maps for October 28, 2003 sun quake. First row shows the same two snapshots for 3.5 and 6 mHz intensity power as previous figures. Second row shows the temporal profiles at 3.5 (left panel) and 6 mHz (right panel) using dots for the southern seismic source and stars for the northern seismic source as defined in Figure 3.24.

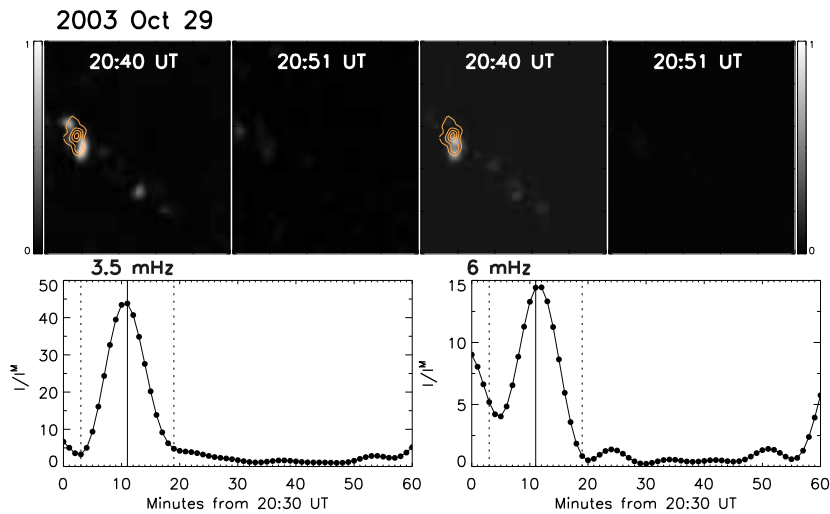


Figure 5.7: Continuum intensity-excess power maps and time profiles for the October 29, 2003 sun quake. Captions are as in Figure 5.1

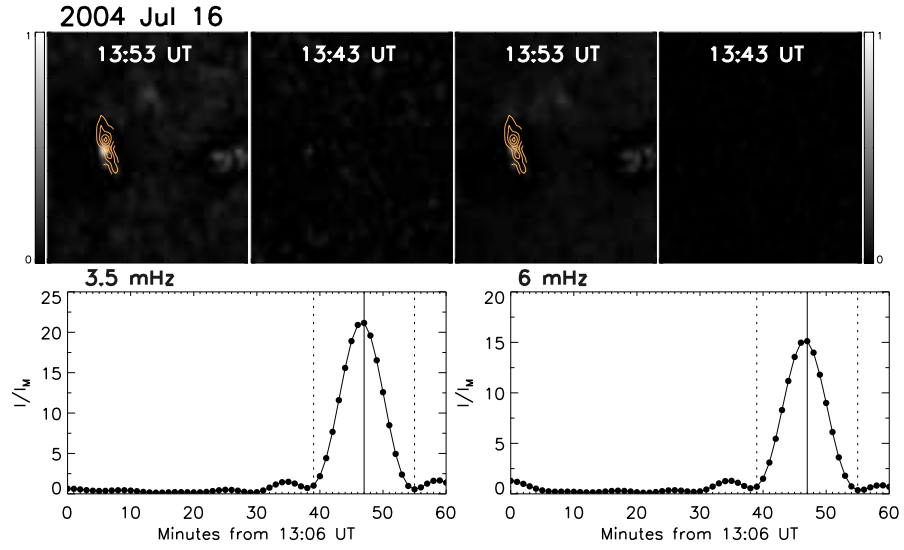


Figure 5.8: Continuum intensity-excess power maps and time profiles for the July 16, 2004 sun quake. Same as Figure 5.1

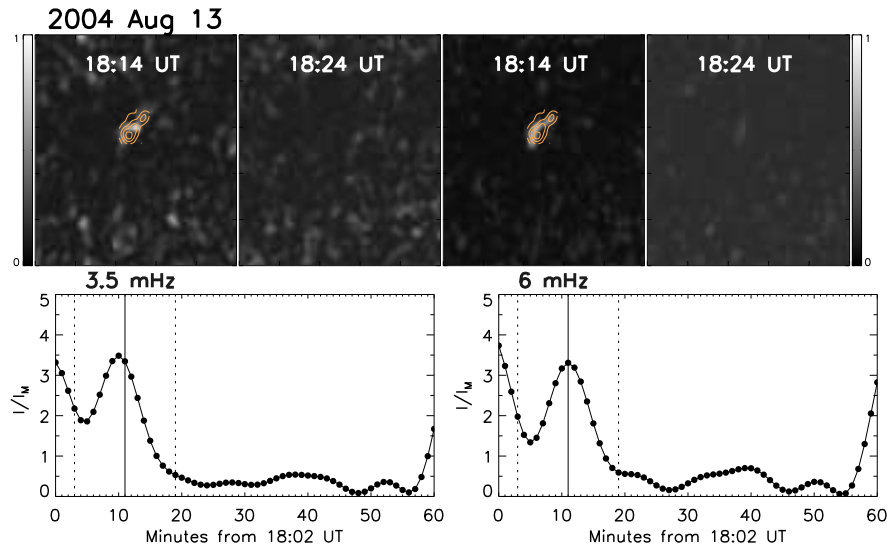


Figure 5.9: Continuum intensity-excess power maps and time profiles for the August 13, 2004 sun quake. Same as Figure 5.1

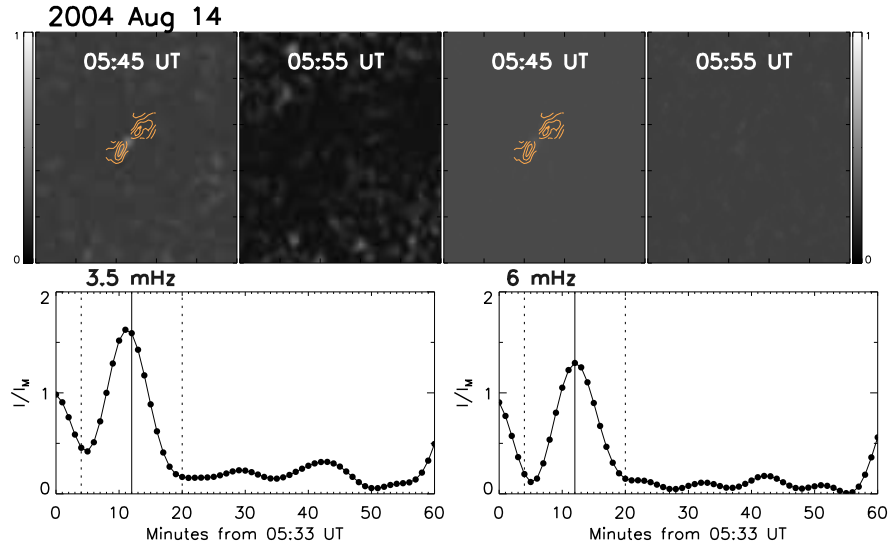


Figure 5.10: Continuum intensity-excess power maps and time profiles for the August 14, 2004 sun quake. Same as Figure 5.1

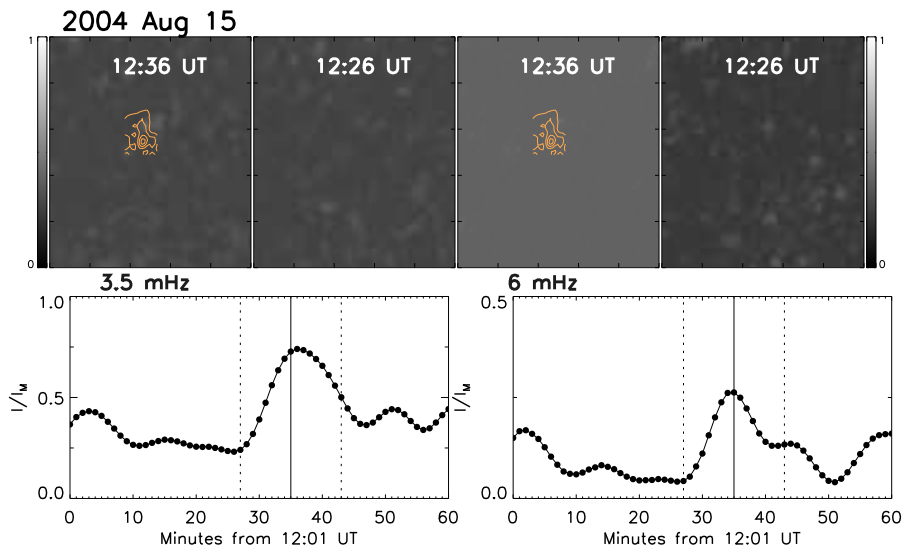


Figure 5.11: Continuum intensity-excess power description figure for August 15, 2001 sun quake. Same as Figure 5.1

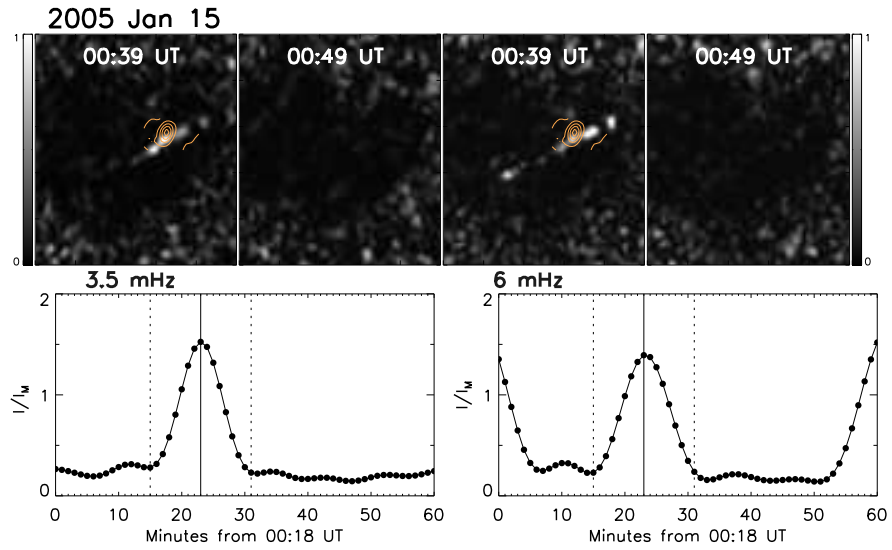


Figure 5.12: Continuum intensity-excess power description figure for January 15, 2005 sun quake. Same as Figure 5.1

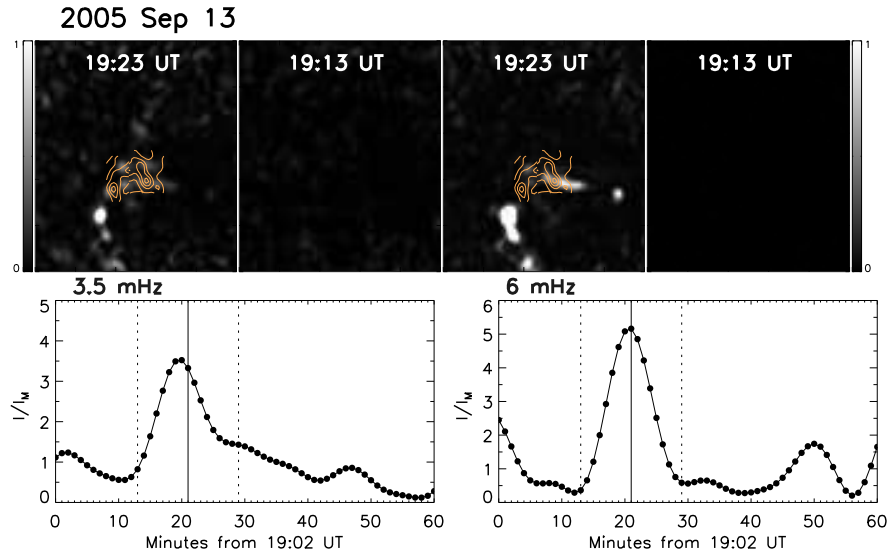


Figure 5.13: Continuum intensity-excess power description figure for September 13, 2005 sun quake. Same as Figure 5.1

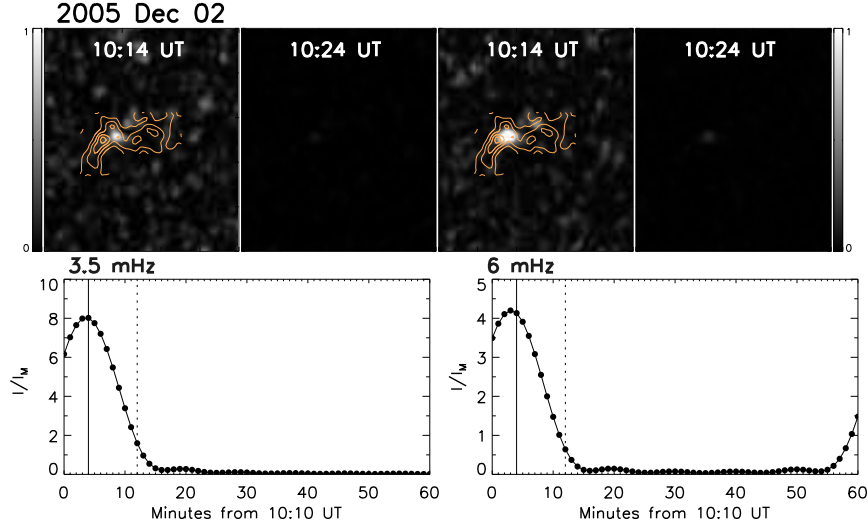


Figure 5.14: Continuum intensity-excess power description figure for December 2, 2005 sun quake. Same as Figure 5.1

## 5.1 Spectrum of the Continuum Emission versus Spectrum of the Acoustic Emission

We have applied standard power spectral analysis to estimate the total energy of the seismic transient released by the September 9, 2001 flare in the 2–4 and 5–7 mHz spectra. These estimates represent that portion of the energy that refracted back to the solar surface to arrive in the 15–60 Mm pupil of the egression computations in a single skip.

We have also estimated the total energy of the white light continuum emission released at the seismic source location. We followed similar steps to those used to estimate the total energy of the acoustic source (see Chapter 3 for details).

For example, for the September 9, 2001 seismic flare, the energy radiated from the M9.5 flare at the location of the seismic transient was  $\sim 1.2 \times 10^{23}$  J ( $\sim 1.2 \times 10^{30}$  erg). The electromagnetic energy radiated from the M9.5-type flare at the location of the seismic transient in this case is  $\sim 0.13\%$  of the

energy radiated by the flare.

Figure 5.15a shows the total energy of the seismic transients, values are taken from tables in Section 3.1. Plotted in blue and pink are the sun quakes generated by X-type and M-type solar flares, respectively. The error bars for each measurement and the date for each sun quake are shown above each line.

Figure 5.15b shows the energy estimated to be released into the photospheric level by the intensity continuum during the sun quakes with the same color codes as Figure 5.15a.

The graphs suggest that the seismic sources injecting acoustic waves into the solar interior can be generated by white light flares of any strength. There is no direct correlation between the strength of the X flare and the power of the sun quakes. Smaller flares can indeed produce powerful sun quakes. Sometimes, WLFs with a large chromospheric emission did not generate a seismic event at all (Bastille day solar flare of 2000). The graph shows various types of intensity continuum hardnesses, from harder to softer. We could not detect a correlation between the hardnesses of the acoustic and intensity emission spectra.

The September 9, 2001 M9.5 flare has a softer spectrum than the X3.6 solar flare of July 16, 2004, which means the M9.5 flare put more energy into the acoustic source than the X3.6 flare. Interestingly, the WL emission of both flares had a similar spectral index, with the large flare depositing more energy into the dense chromospheric layers. But this is not reflected in the acoustic spectrum. The seismic source of the X3.6 flare is weaker at 6 mHz.

The energy emitted at 3.0 mHz was  $\sim 1.1 \times 10^{20}$  J ( $1.1 \times 10^{27}$  erg), while the energy estimated at 6.0 mHz was  $\sim 2.0 \times 10^{19}$  J ( $2.0 \times 10^{26}$  erg). Extrapolating across the missing 4.0–5.0 mHz spectrum, we estimate a total acoustic 2.0–7.0 mHz emission of  $1.6 \times 10^{20}$  J ( $1.6 \times 10^{27}$  erg), with the 5.0–7.0 mHz emission being 12.5% of the total. From the *GOES* soft X-ray flux we estimated a total soft X-ray emission of  $\sim 6.2 \times 10^{21}$  J ( $6.2 \times 10^{28}$  erg). The total acoustic energy is therefore 2.5% of the soft X-ray emission.

The January 15, 2005 solar flare which generated the largest sun quake at the solar surface has a very soft WL power spectrum. Probably, the energy input via the back-warming mechanism was very efficiently done at low frequencies. The acoustic power spectrum of this flare was much softer than the Ic power spectrum.

Table 5.1 (reproduced from Moradi et al. (2007)) shows the energy estimates of the acoustic power of some of the significant sun quakes:

Table 5.1: Energy estimates of the seismic signatures of sun quakes detected to date.

Date	Type	3 mHz (ergs)	6 mHz (ergs)	1–8 Å X-Rays (ergs)	WL (ergs)
1996 Jul 09	X2.6	$7.5 \times 10^{27}$	$2.4 \times 10^{26}$	$2.8 \times 10^{29}$	—————
2001 Sep 09	M9.5	$1.1 \times 10^{27}$	$2.0 \times 10^{26}$	$6.2 \times 10^{28}$	$1.2 \times 10^{30}$
2003 Oct 28	X17.2	$4.7 \times 10^{27}$	$9.4 \times 10^{26}$	$5.0 \times 10^{30}$	—————
2003 Oct 29	X10.0	$9.4 \times 10^{26}$	$3.5 \times 10^{26}$	$1.5 \times 10^{30}$	$3.8 \times 10^{29}$
<b>2005 Jan 15</b>	<b>X1.2</b>	$2.4 \times 10^{27}$	$1.0 \times 10^{27}$	$3.4 \times 10^{29}$	$2.0 \times 10^{30}$

Table 5.2 shows values of the spectral hardness of sun quakes computed for the excess intensity continuum and acoustic power continuum using the formula:

$$H = \frac{A - B}{A + B} \quad (5.1)$$

where  $A$  and  $B$  are the values of the total energy estimations at 3/3.5 and 6 mHz, respectively. In bold letters we emphasize the flares with a harder spectrum for each set of values, and with italics, the softest flares.

Table 5.2 suggests that there are flares where the hardness in the acoustic source is greater than its correspondent in intensity continuum power, which implies that for some flares the energy deposited by the white light transient into the photosphere did not entirely convert into acoustic energy. Clearly, local conditions in each active region, and the location of the flaring reconnection site are the main factors determining how the energy budget of the flare is distributed. However, to be able to differentiate between different types of energy transport into the low atmosphere, and further into the photosphere, one needs a far more detailed analysis and better statistics for the seismic flares.

Date	Continuum Hardness	Acoustic Hardness
2000 November 24	0.42	0.67
2001 September 09	0.58	0.63
2002 July 15	<b>0.13</b>	0.68
2002 July 23	0.63	<b>0.19</b>
2002 August 21	0.71	0.32
2003 October 23	0.37	0.59
2003 October 28	0.66	0.30
2003 October 29	0.76	0.39
2004 July 16	0.71	0.24
2004 August 13	0.73	0.61
2004 August 14	0.40	<i>0.77</i>
2004 August 15	0.42	0.38
2005 January 15	<i>0.84</i>	0.37
2005 September 13	0.72	0.68
2005 December 02	0.55	0.63

Table 5.2: Values of hardness obtained from the energy estimations at 3/3.5 and 6 mHz for the excess intensity continuum power and egression power. Bold and italics values represent the hardest, and softest spectra, respectively.

## 5.2 Conclusions

This is the first time that the behaviour of the hardness ratio has been completely analysed. The hardness ratio is a physical parameter which provides information (even if not complete) on the spectral behaviour of the acoustic source. The comparison with the hardness ration of the continuum intensity has brought out several important points:

- strong evidence of continuum emission is a characteristic of a significantly heated photosphere;
- the intensity continuum power excess emission shows basically the same

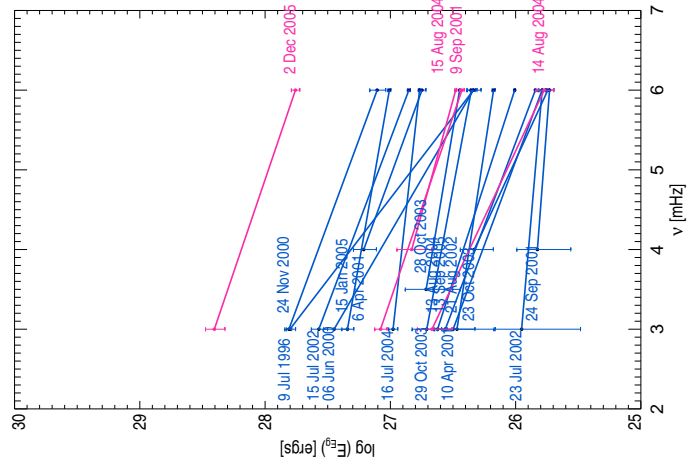
properties as the egression power with very good spatial correlation;

- there is also a very good temporal correlation between the two signatures;
- the suddenness of the intensity continuum emission still remains the key in the generation of sun quakes;
- the transfer of flare energy into the photosphere happens during the impulsive short phase of the flare, which lasts about two minutes.

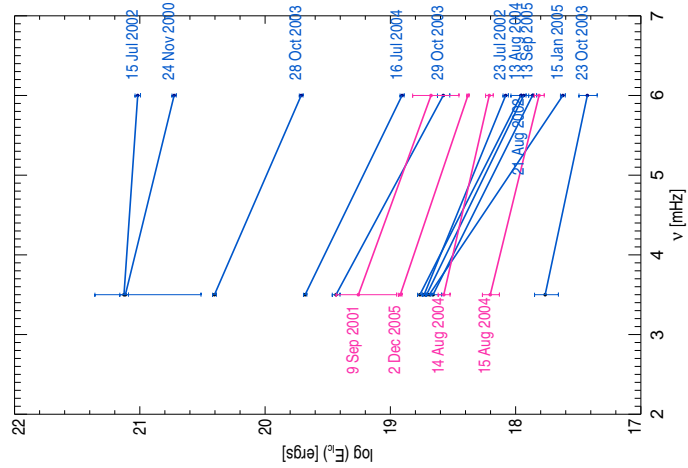
The suggestion from this work is that acoustic emission from flares is driven by photospheric heating that is closely associated with the continuum emission observed. We consider that an electron beam precipitates into the chromosphere in the impulsive phase, producing enhanced Balmer and Paschen continuum edge emission through non-thermal excitation and ionization of the chromosphere (Zharkova and Kobylinski, 1993). The photosphere is a strong absorber of this radiation that is emitted downward and causing heating. The immediate effect of this absorption in the visible spectrum is a dissociation of  $H^-$  ions, that affects the photospheric opacity<sup>1</sup>. However, ionization ratios in the photosphere, because of the much greater free-electron density than in the chromosphere, are strongly coupled to the local kinetic thermal motion, by collisions. This leads to relaxation to a thermal equilibrium between local ionization and kinetic temperatures, bringing about a commensurate rise in the latter at the expense of the former and a proportionate increase in pressure, which we suppose drives an acoustic transient into the subphotosphere. The assumption behind the hypothesis suggested above, is based on the supposition that heating of the low photosphere by any other means, by high-energy particles in particular, is impossible.

---

<sup>1</sup>For details of  $H^-$  free-bound absorption in the photosphere, see Figures 23n-r of Vernazza et al. (1981).



(a) The acoustic spectra of sun quakes at 3 and 6 mHz; y-axis shows the total acoustic power averaged over the seismic source area  $E_{Eg}$  (erg) at 3 and 6 mHz.



(b) The intensity continuum emission spectra of sun quakes at 3.5 and 6 mHz. The total intensity continuum power  $E_{Ic}$  (erg) is averaged over the seismic source area.

Figure 5.15: The M-class solar flare-generated sun quakes are represented in a pink color, whereas the X-class solar flare-generated sun quakes are shown in blue.

## Chapter 6

# Radiative Hydrodynamic Simulations of the Solar Atmosphere: Clues for Sun Quakes

Solar white-light flares (WLF) refer to flares that are visible in the optical continuum. Acoustically active flares (AF) refer to flares that generated seismic disturbances at the photospheric level and strong sun quakes. From the wealth of data analysed in the previous chapters and the references therein, we can say that AF are also WLF. We want to learn how the AF are being produced. We have clues that probably the most efficient mechanism in transporting energy from the flare reconnection site into the photosphere and generating sun quakes must be related to the radiative back-warming. This should be valid for flares where direct heating of the low atmosphere by electron beams is not possible.

In most cases, non-thermal electrons, whose energies are not necessarily high, heat the chromosphere first, and then the enhanced radiation from upper layers is transported to deeper layers and causes heating there. This is called back-warming ([Machado et al., 1989](#)). The white light continuum is formed through either the recombinations of the hydrogen atoms in the lower chromosphere and/or the emission of negative hydrogen ions in the upper photosphere ([Ding and Fang, 1994](#)).

Several mechanisms have been proposed to explain the seismic emission

from flares (see Chapter 4). Similarly, there are also a few mechanisms that can explain the white-light emission (Metcalf et al., 1990a,b; Gan and Mauas, 1994). The spatial and temporal similarities observed by us in the white light and seismic maps of an active region hosting an AF suggest that there must be a unique mechanism that produces a WLF with AF characteristics. Considering the relevance of back-warming for the production of sun quakes, it is necessary to study full radiative hydrodynamic models of a flaring atmosphere in order to learn the relationship between the white-light emission and the seismic emission.

There are essentially two questions related to WLF and AF that we need to answer from simulations. First: what is the amount of energy needed to reach the photospheric layers via back-warming in a very short period of time (almost sudden) and trigger a seismic event? We want to know what factors (atmospheric or/and sub-photospheric) determine whether flares show or do not show any seismic responses. If the photospheric response is prompted by the energetic particles as we often assume, the strength of the response should depend on characteristics of energetic particles.

The second is how different should the solar atmospheric conditions be to allow for some flares to deliver acoustic energy into the photosphere, whereas other flares (the majority, even major ones) remain seismically quiet? It is worth mentioning here that Martinez-Oliveros and Donea (2009) suggested the seismic sources seem to occur in flares where the magnetic reconnection takes place in a relatively low layer of the atmosphere, where the initial conditions are different. Clearly, the transfer of energy to the deep layers of the atmosphere is different for low or high flares. The balance of energetic heating against losses (radiative, shocks, diffusive losses) for each atmospheric layer is also very important.

In this chapter I will present the results of 1D radiation hydrodynamics non-linear simulations using the code RADYN (Carlsson and Stein, 1995) to assess the strength and nature of photospheric transients caused by solar flares of various types. The remainder of this chapter is organised as follows. In Section 6.1, we briefly discuss the numerical methods. We present the computational results in Section 6.2 and show the role of back-warming in increasing the seismicity of an active region in Section 6.2.3. Discussions end Section 6.3.

## 6.1 Numerical Method

In order to test and interpret our helioseismic results, theoretical calculations of radiative hydrodynamic models relating the WL and seismic emissions, are performed using the radiative hydrodynamics modelling code RADYN (Carlsson and Stein, 1995). We used the formalism described by Allred et al. (2005), which employed the RADYN code developed by Carlsson et al. (1994); Carlsson and Stein (1995, 1997). The code solves one-dimensional equations of mass, momentum and energy conservation together with the non-LTE radiative transfer and population rate equations, implicitly on an adaptive mesh via NewtonRaphson iteration (Carlsson and Stein, 1992). The adaptive mesh is important when modelling the dynamics of the lower atmosphere during flares.

We used a modified version of the Carlsson and Stein (1997) code, similar with that employed by Abbett and Hawley (1999), to model the radiative-hydrodynamic response of the lower atmosphere in a non-magnetic plane-parallel model. The model also includes the upper transition region and the corona.

Figure 6.1 (left two graphs) shows the initial atmospheric model represented by the temperature variation with height and mass ( $\text{g}/\text{cm}^2$ ). The two right frames show, for comparison, the equilibrium models of Vernazza et al. (1981). The use of a quiet sun model atmosphere is consistent with our neglect of magnetic field, though Cheng et al. (2010) have chosen to use a model sunspot atmosphere in their similar calculations.

The non-LTE radiation hydrodynamics treated in this code is characterised by the following equations:

conservation of mass

$$\frac{\partial \rho}{\partial t} + \frac{\partial \rho v}{\partial z} = 0, \quad (6.1)$$

conservation of momentum

$$\frac{\partial \rho v}{\partial t} + \frac{\partial \rho v^2}{\partial z} + \frac{\partial}{\partial z}(p + q_v) + \rho g = 0 \quad (6.2)$$

conservation of internal energy

$$\frac{\partial \rho e}{\partial t} + \frac{\partial \rho v e}{\partial z} + (p + q_v) \frac{\partial v}{\partial z} + \frac{\partial}{\partial z}(F_c + F_r) - Q = 0, \quad (6.3)$$

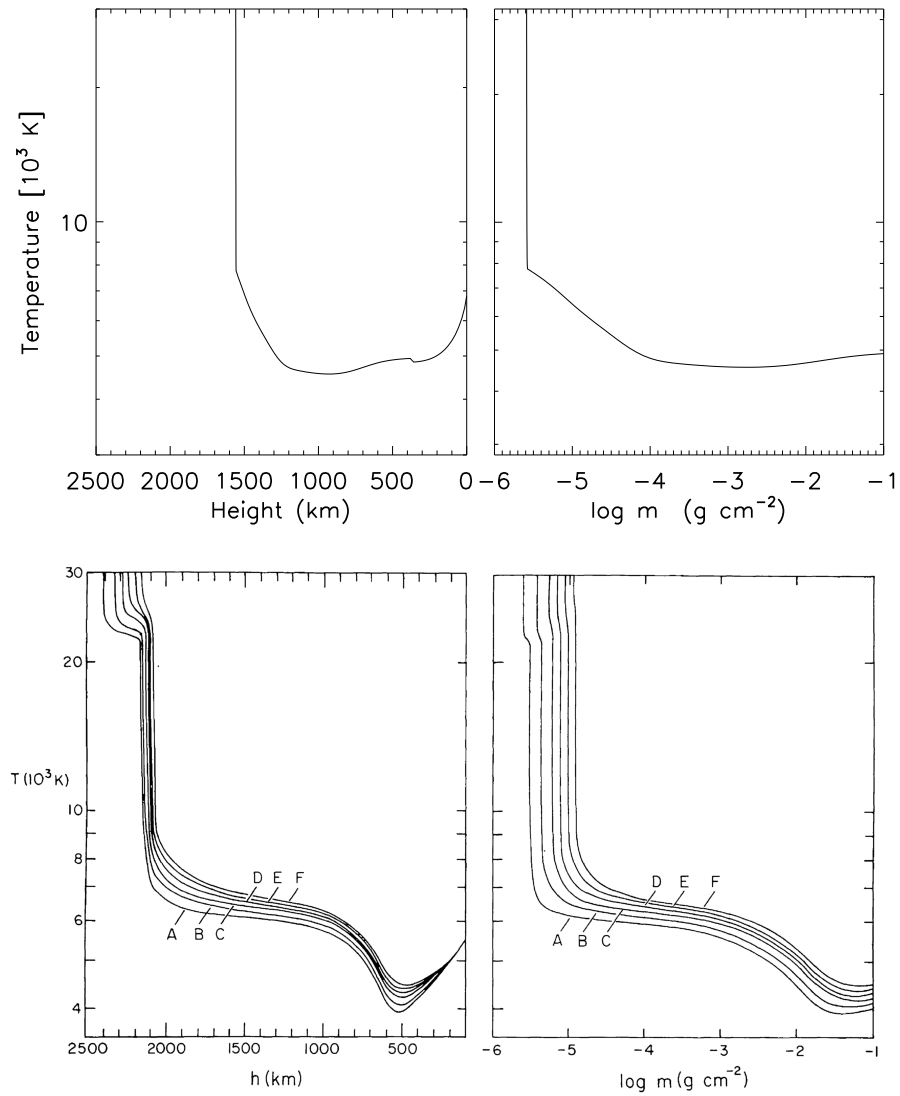


FIG. 10.—Temperature as a function of height and of  $\log m$  for models A-F

Figure 6.1: Left panels: Temperature profile of the initial model atmosphere as a function of height and mass. Right panels: Temperature profile for the quiet Sun - Figure 10 from [Vernazza et al. \(1981\)](#).

along with level population equation

$$\frac{\partial n_i}{\partial t} + \frac{\partial n_i v}{\partial z} - \left( \sum_{j \neq i}^{N'} n_j P_{ij} - n_i \sum_{j \neq i}^{N'} P_{ij} \right) = 0 \quad (6.4)$$

equation of radiative transfer

$$\mu \frac{\partial I_{\nu\mu}}{\partial z} = \eta_{\nu\mu} - \chi_{\nu\mu} I_{\nu\mu} \quad (6.5)$$

The notations are:  $\rho$  is density,  $t$  is time,  $v$  is velocity,  $z$  is height,  $p$  is pressure,  $q_v$  is viscous stress,  $g$  is acceleration due to gravity,  $e$  internal energy per unit mass,  $F_c$  and  $F_r$  refer to conductive and radiative fluxes,  $Q$  is any source of external, non-radiative heating,  $n_i$  - number densities in a given atomic state, along with transition rate per atom  $P_{ij}$  from state  $i$  to state  $j$ ,  $N'$  is the total number of atomic states calculated in detail,  $I_{\nu\mu}$ ,  $\chi_{\nu\mu}$  and  $\eta_{\nu\mu}$  are specific intensity and the absorption and emission coefficients per unit volume, frequency and angle dependent ( $\nu, \mu$ ).

The conductive flux dominates in the corona. In order not to overestimate the conductive flux in the transition region, we used the [Abbett and Hawley \(1999\)](#) method.

The code uses 191 grid points to resolve the atmospheric characteristics. The large number of grid points is needed because strong shocks and compression waves, can develop quickly and must be resolved during simulations. More details about the computational technique can be found in [Carlsson and Stein \(1992, 1997\)](#) and [Abbett and Hawley \(1999\)](#).

### 6.1.1 Boundary and Initial Conditions

As initial conditions we considered the atmosphere in a state of hydrostatic equilibrium with a  $T = 10^6$  K corona at the highest point 10.347 Mm and all vertical velocities being zero.

In the final days of the preparation of this thesis, [Cheng et al. \(2010\)](#) obtained similar results to those presented here for the initial atmosphere described in Figure 6.2. They went further with their analysis, considering an initial atmosphere relevant to for a sunspot.

The main aim of this work is to study the role of back-warming in the formation of sun quakes.

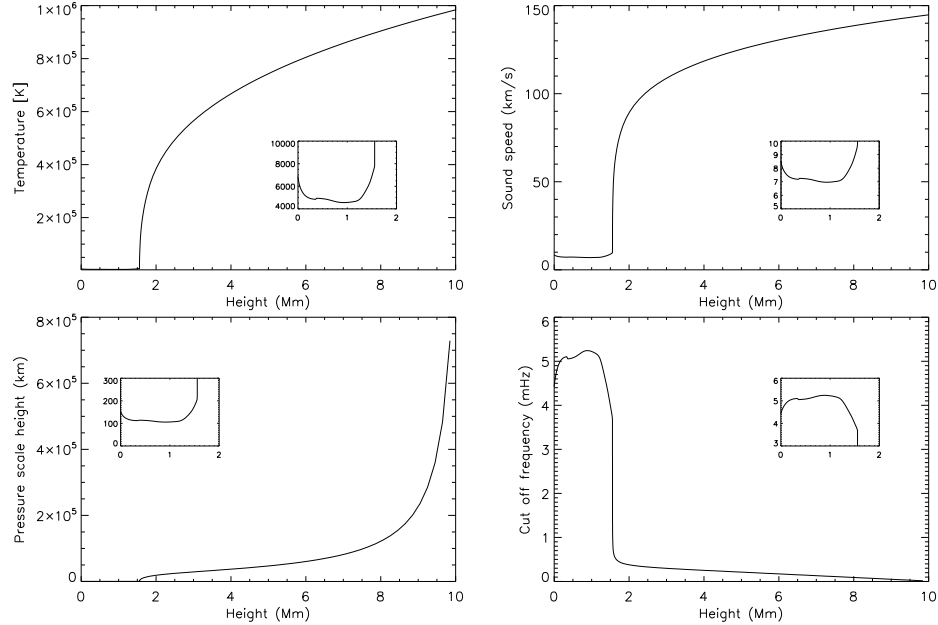


Figure 6.2: The initial atmosphere as described by the temperature, sound speed, pressure scale height and cut off frequency. Insets in all frames show a close up of the first 2 Mm in the atmosphere.

The first frame of Figure 6.2 shows the atmospheric temperature profile, with a close up for temperatures below the coronal level. The temperature minimum of 4555.2 K is around 0.93 Mm. The second frame in the top row of Figure 6.2 shows the sound speed in km/s vs. height.

The two frames of the bottom row show the pressure scale height and the acoustic (isothermal) cut off frequency,  $\nu_c$  defined by:

$$\nu_c = \frac{1}{4\pi} \times \frac{c}{h} \quad (6.6)$$

where  $c$  is the sound speed and  $h$  is the local pressure scale height.

We have imposed a zero gradient temperature boundary at the top of the corona and a fixed temperature at the bottom of the photosphere as boundary conditions for our computations with all  $v_z$  being zero.

### 6.1.2 Non-thermal Electron Population Beams

The main disruptor of a quiet solar atmosphere is a solar flare. During a flare, non-thermal electrons are accelerated by magnetic reconnection in the corona and propagate downwards along the magnetic field lines. They lose their energy during the transportation, producing hard X-ray emission in the chromosphere by bremsstrahlung (Brown, 1971). Only electrons with very high energies (mainly from large flares) can reach down the photosphere (Lin and Hudson, 1976). Generally, the non-thermal populations of electrons are described by the following parameters: a low-energy cutoff  $E_c$  which can be between 12 keV and 24 keV; power law distributions with an electron spectral index  $\delta$  varied between 4 and 6, while total electron energy flux ranges from  $3 \times 10^{25}$  erg/s to  $1.4 \times 10^{27}$  erg/s. We consider  $E_c = 20$  keV and  $\delta = 5$  for our simulations.

In our simulations we vary the electron beam fluxes from  $10^8$  (F08),  $10^9$  (F09),  $10^{10}$  (F10) to  $10^{11}$  (F11) ergs/cm<sup>2</sup>/s. Lower particle beam fluxes mean a weaker flare. The rate of energy deposited by the electron beam is modelled using the technique of Emslie (1978).

## 6.2 Results

We performed simulations of the flaring atmosphere with RADYN for several types of solar flares whose magnitude is defined by their input electron beam fluxes. We simulated the atmospheric response for different electron heating functions: a) a top hat function, with a temporal-width of 1 second or up to 20 seconds; b) a Gaussian shaped function and c) an ascending Gaussian/descending exponential beam impulse.

For large flares, the RADYN codes enters into a numerical instability mode, simulations become unstable for numerical reasons and the runs must be truncated. The cause of the numerical instability that stops the code is probably related to large gradients of physical parameters for some local flaring conditions. For example, the F10 and F11 runs, for a 20 seconds top hat like injection of particle beams, stop after 60 seconds and 3 seconds, respectively.

For an injection function of non-thermal electrons with a top hat shape of 1 second width, we could run the simulations of all F08–F11 flares for 1000 seconds.

Many observations have shown that a temperature enhancement can occur in the lower atmosphere, around the temperature-minimum region and photosphere during flares (Machado et al., 1978). From Allred et al. (2005) and very recently Cheng et al. (2010), heating in the lower atmosphere is produced by absorption of the downwards radiation (back-warming). Ding et al. (2003) also made non-LTE calculations and found that back-warming can efficiently heat the lower atmosphere to explain the observed continuum emission near 8500 Å.

Here, we analyse this problem through radiative hydrodynamic simulations. We are interested in finding how much energy can travel downwards into the photosphere, via radiation or shock-waves. The transported energy will turn quickly into heat, causing a pressure transient that drives a seismic wave into the interior of the Sun. This is observationally seen as a photospheric dent in the *MDI* Dopplergrams during an acoustically active flare. The seismic energy radiated in a typical sun quake is estimated at several times  $10^{27}$  ergs. As powerful as sun quakes are, the seismic energy released in them is only about a thousandth of the total energy radiated into space by a major solar flare in its impulsive phase alone.

We can analyse the mechanical energy flux carried by a disturbance travelling exclusively either directly upwards or downwards. The disturbance penetrating into the photosphere can be conveniently described using a pressure and density scaled “velocity”:

$$u_z = (p\rho)^{1/4}v_z \quad (6.7)$$

A simple plot of  $v_z$  does not show the small scale details of the simulations, especially for the first seconds after the injection of non-thermal particles. Therefore, to compensate for the large downwards diminution of  $v_z$  itself, we use  $u_z$  instead. One should consider that, to within a factor of approximately  $\Gamma_1^{1/2}$ <sup>1</sup>

$$u_z^2 \sim \rho v_z^2 c. \quad (6.8)$$

where  $c$  is the sound speed. This can be regarded as a measure of the flux of kinetic energy transported acoustically in the atmosphere. During flares, the

---

<sup>1</sup> where  $\Gamma_1 = \frac{d \ln p}{d \ln \rho}_{\text{ad}}$  is the first adiabatic exponent of Chandrasekhar (Chandrasekhar, An Introduction to the Study of Stellar Structure, University of Chicago Press, 1939). It’s major use is in the formula for sound speed,  $c^2 = \Gamma_1 \frac{p}{\rho}$ .

mass motions during flares raise the density in the transition region and the corona becomes elevated. This has a significant importance in transporting energy towards the lower layers of the photosphere, where we expect sun quakes to be triggered.

In the following analysis I take simulations for models of flares with a low electron energy cut off of 20 keV and peak beam fluxes of F08 – F11. The time profile of the injected particle beam is either a top hat function (width 1 seconds or 20 seconds) or a Gaussian shaped function. I will start with the description of the results obtained with the 1 second top hat electron flux.

### 6.2.1 Mechanical energy flux of chromospheric transients varying with the electron beam fluxes

Figures 6.3 and 6.4 show the  $u_z$  variation (z-axis) as a function of height in the atmosphere and time for four flares, from weak F08 (6.3a) to strong F11 flares (6.4b). On top of each figure the two panels show the  $u_z$  profile for the first 5 Mm above the photosphere. Left panel (green) represents the  $u_z$  variation at 1 sec. The right panel (pink) represents the  $u_z$  variation 15 seconds later. The dotted vertical line shows 0 Mm in both panels.

The small transient observed at around 1 Mm, is related to the moment when the beam of particles was injected in the chromosphere. The atmosphere reacts almost instantaneously to the heating by electrons. The stronger the flare, the larger  $u_z$ , which means more heating occurs at the injection point. This can be seen as a large disturbance of  $u_z$ , for the cases of larger flares F10 and F11.

According to [Allred et al. \(2005\)](#) and from our simulations (easy to see in movies of the results), there is an explosive increase in temperature, which creates a supersonic shock wave that pushes material upwards and downwards. This disturbance, propagates towards the photosphere as a chromospheric shock wave. An upward shock is developed too, pushing the material into the corona. We are mainly interested in following what happens with the energy transients that reaches the photosphere. However, according to simulations, the shock wave reaches the low photosphere in more than 100 seconds (faster for F10 flares).

We recall here that the observations for the October 29, 2003 seismically active solar flare show the D<sub>1</sub> line of neutral sodium at the onset of the flare with clear evidence of a downwards propagating shock/condensation at the

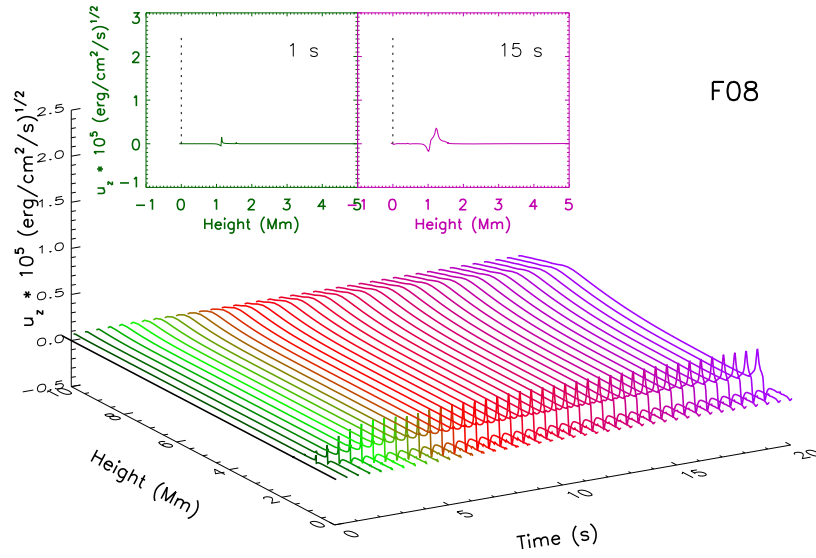
onset of the flare. Concurrent *GONG* intensity observations show significant flare emission with a sudden onset in the compact region encompassing the acoustic signature.

The most important characteristic of these plots and the whole simulation set is the following: essentially coincident with the onset of thick-target heating of the chromosphere is a sharp transient emanating in the low photosphere at height zero. This is seen in Figure 6.3b left inset, and even better in Figures 6.4a and 6.4b, which show excited  $u_z$  beneath the downwards-propagating chromospheric disturbance. A downwards-propagating counterpart of this transient disappears into the underlying solar interior. For a F11 solar flare, the transient has the largest  $u_z$  as expected. This transient reaches the low photosphere in less than 15 seconds. Such a transient was predicted by Donea et al. (2006b); Moradi et al. (2007), and Lindsey and Donea (2008) as a result of immediate back-warming by intense continuum emission from the heated chromosphere, emission that from Earth appears as a white-light flare.

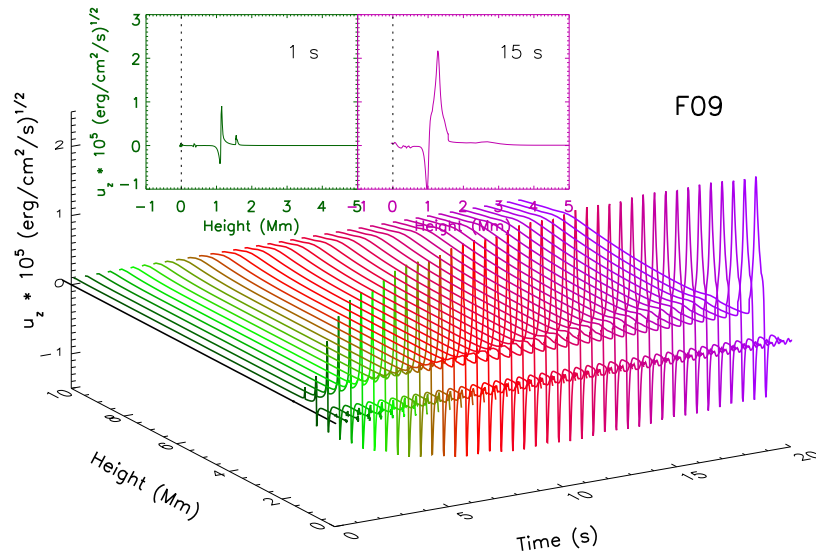
In order to drive a wave that substantially penetrates beneath the chromosphere and photosphere into the solar interior, the heating that drives the wave must be relatively sudden. The basic time scale characterizing the gravitationally stratified photosphere is 40 seconds (Donea and Lindsey, 2005) for  $c \sim 7$  km/s and  $H = 140$ km. Therefore, a depression of the photosphere followed by a relaxation, both on a time scale much longer than 40 seconds will not drive a substantial acoustic wave. However, if the depression and/or relaxation is done on a time scale much shorter, then a substantial fraction of the work done by the transient will be converted into acoustic energy, which will radiate into the subphotosphere and emanate as a sun quake.

The magnitude of the disturbance at the photospheric level in this scaled velocity graph is about  $-5$  (ergs/cm<sup>2</sup>/s)<sup>1/2</sup> for a F08 flare. The negative sign is related to the sign of  $v_z$ .

For a F09 flare,  $u_z$  shows a greater disturbance reaching the photospheric level. Its magnitude is two orders greater than its correspondent for F08:  $\sim 500$  (ergs/cm<sup>2</sup>/s)<sup>1/2</sup>.

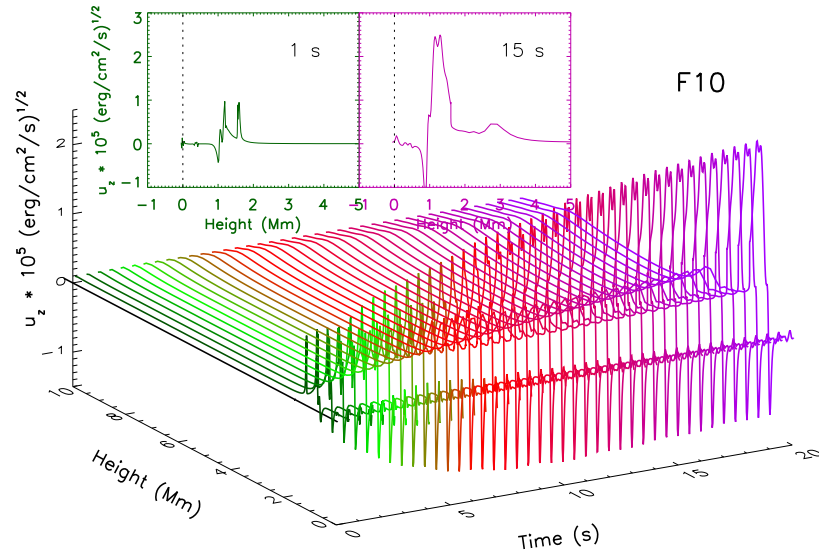


(a) F08 - 1 second impulsive beam flux

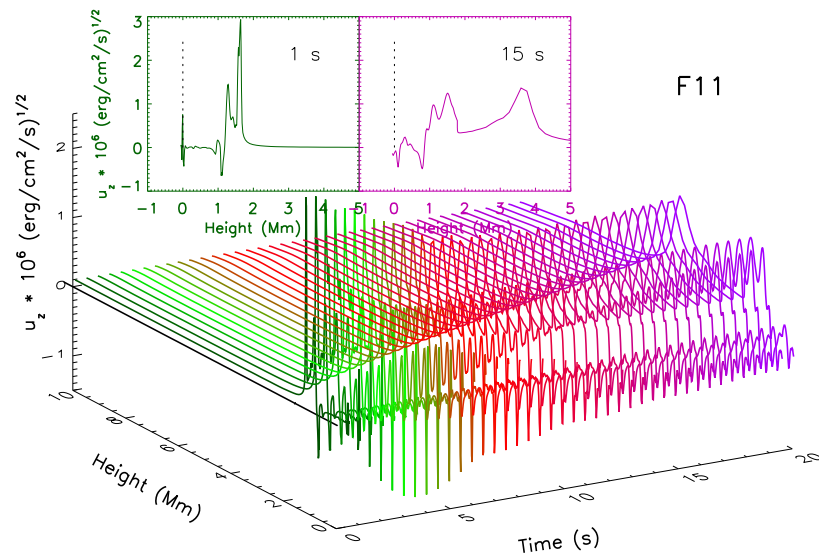


(b) F09 - 1 second impulsive beam flux

Figure 6.3: F08 and F09 energy transients, represented as  $u_z$  at different heights and times in the solar atmosphere. Colours are associated with time: starting with dark green at the beginning, changing through red to magenta as time increases.

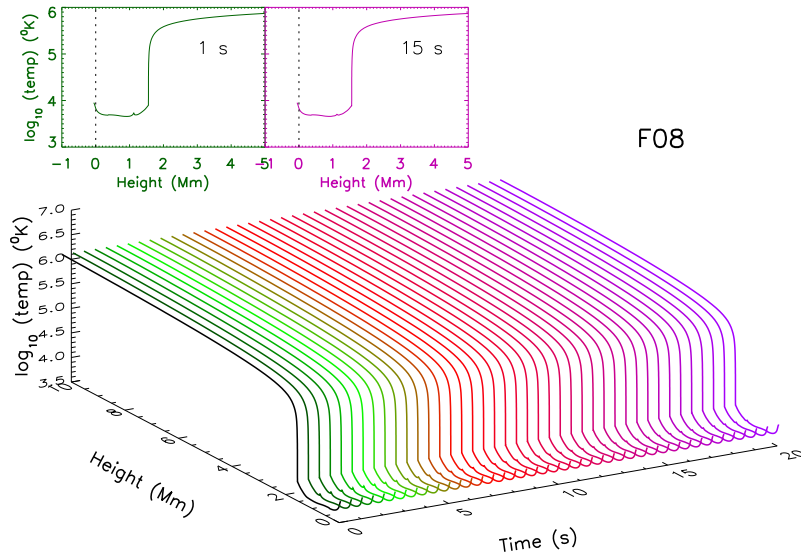


(a) F10 - 1 second input flux

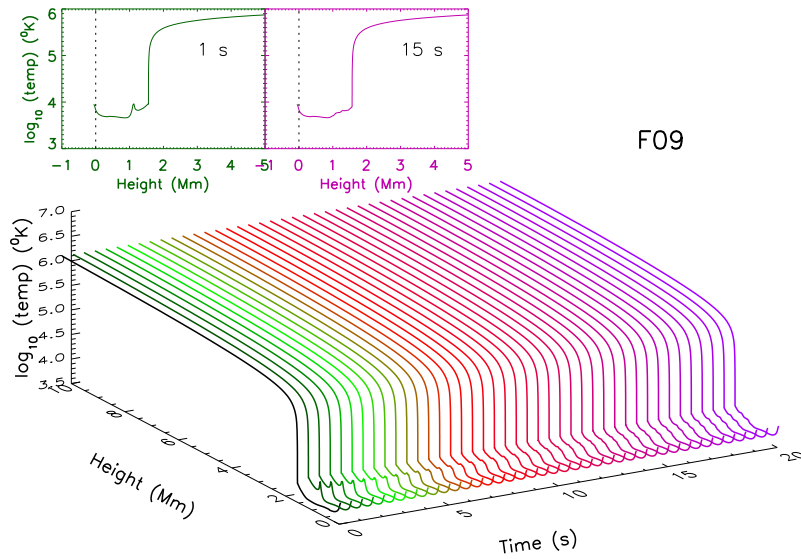


(b) F11 - 1 second input flux

Figure 6.4: F10 and F1 energy transients, represented as  $u_z$  at different heights and times in the solar atmosphere. Colours are associated with time: starting with dark green at the beginning, changing through red to magenta as time increases.

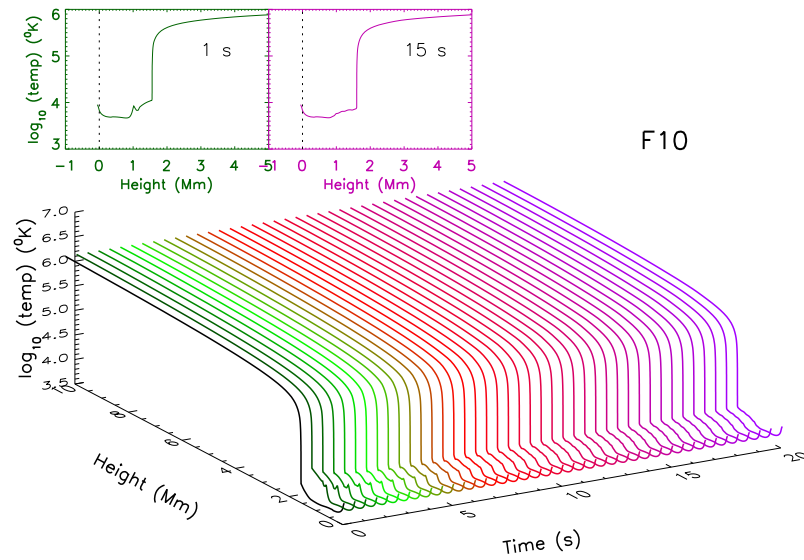


(a) F08 - 1 second input flux

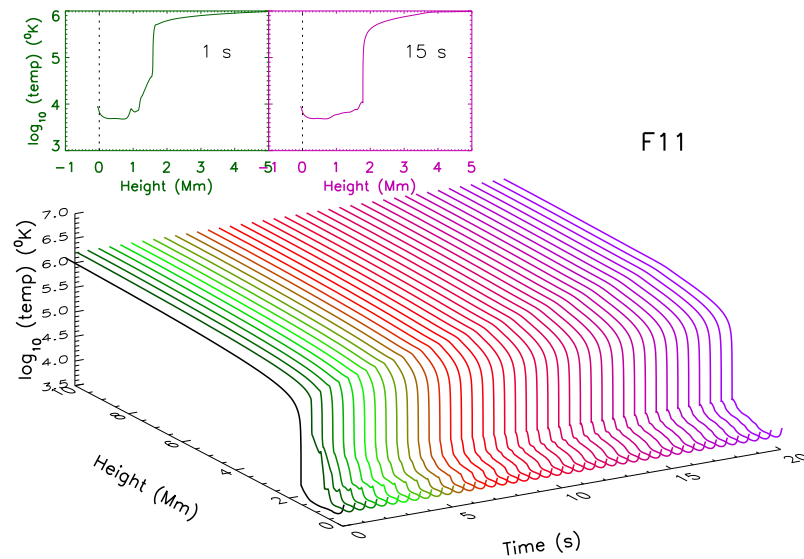


(b) F09 - 1 second input flux

Figure 6.5: 3D plot of the logarithm of the atmospheric temperature as a function of height and time for F08 and F09. Colours are associated with time: starting with dark green at the beginning, changing through red to magenta as time increases.



(a) F10 - 1 second input flux



(b) F11 - 1 second input flux

Figure 6.6: 3D plot of the logarithm of the atmospheric temperature as a function of height and time for F10 and F11. Colours are associated with time: starting with dark green at the beginning, changing through red to magenta as time increases.

### 6.2.2 Temperature Profiles Varying with the Electron Beam Flux

Figure 6.5a shows the variation of the atmospheric temperature as a function of height and time for a F08 flare. We have also plotted the temperature profiles for stronger flares in Figure 6.5b, Figure 6.6a and Figure 6.6b

We reproduce the first 20 seconds of the simulations, because we are interested to see what the faster sharp transient can do to the atmosphere, in this short time.

In the first seconds of the simulations, the chromosphere heats up because of the energy deposition of the beam at around 1 Mm. This is easily seen in all F08–F11 flares. From Figure 6.6a and Figure 6.6b, a significant temperature rise in the lower atmosphere, from 0 to 2 Mm.

The increase in temperature will ionize the hydrogen until it reaches a plateau slightly above  $10^4$  K, where the radiative cooling of hydrogen becomes important. During the first seconds the pressure in the chromosphere also increases and the strong chromospheric waves start propagating upwards (the dominant wave) and downwards (weaker wave). As expected the heating of the chromosphere happens faster for an F11 particle beam. When the hydrogen becomes almost ionized, the continuous heating from the beam of particles will create an imbalance between heating and cooling with the temperature of the chromosphere rising again. Now, it is the turn of He I to become ionized to He II. But this happens seconds later. Meanwhile, the transient that resulted from the first impact of the particle beams has been travelling downwards into the photosphere. Its counterpart travelled into the corona.

Allred et al. (2005) also showed that for an F11 flare, the sharp transient can reach the photosphere while the beam is still depositing most of its energy in the chromosphere. Heating in the chromosphere followed by radiative back-warming is indeed a source of heating in the lower layers of the atmosphere.

### 6.2.3 Intensity Continuum Differences Calculated for Various Electron Beam Fluxes

We will plot the intensity continuum contrast defined as the maximum of  $(I - I_0)/I_0$ , where  $I_0$  is the local intensity before the flare and  $I$  is the intensity of the flare. The pre-flare value is taken from the initial conditions

of the flare. We want to see what the enhancement of the continuum emission is and how we can compare this with observations, mainly from seismically active flares.

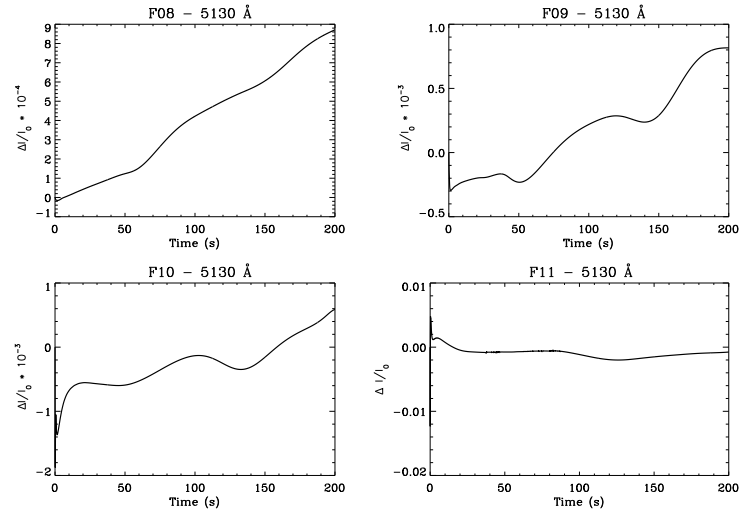


Figure 6.7: Plots of the continuum emission at 5130 Å for various electron beam fluxes. The spectral index of electrons is  $\delta = 5$ , the low energy is  $E_c = 20$  keV. The initial atmosphere is described by Figure 6.2.

Let's summarize quickly some of the observational findings about the intensity continuum contrast. In a very recent paper of [Jess et al. \(2008\)](#), high contrast (300%) blue continuum emission was reported for a small C2.0 flare.

For the X10-class seismic solar flare of October 29, 2003, the local continuum intensity in the quake region underwent a 12% increase inside of 2 minutes at the onset of the flare, followed by a relaxation to an equilibrium some 4% less than before the flare, over the succeeding 20–30 minutes. For another seismic solar flare of September 9, 2001 (M 9.5-class flare) the local irradiance integrated over the quake region (horizontal rectangle drawn in Figure 5a in [Donea et al., 2006b](#)) underwent an increase of 2.5% of its pre-flare value of  $0.452 \text{ Watt m}^{-2}$  at 20:42 UT in the succeeding minute to  $0.463 \text{ Watt m}^{-2}$  at 20:43 UT. This was followed by a relaxation back to a gradually increasing equilibrium over the succeeding several minutes. [Donea et al. \(2006b\)](#) specified that "It is entirely possible that the increase in intensity at the onset of the flare is considerably more sudden than the one

minute sampling interval of the GONG observations.” Indeed observations show a continuum enhancement generally occurring in the first two minutes of the impulsive phase of the flare.

We studied the light curves of the continuum emission at 5130 Å during flares of various strengths (F08 to F11). Figure 6.7 shows the continuum visible emission for four flares, when the injection beam of particles happens in 1 second, following a top hat. Figure 6.8 shows the flare continuum emission at the early stages of the F08 to F11 runs. Figure 6.9 show a similar plot but using an electron beam injected with a Gaussian profile of 1 second width.

It is easy to observe that on a long time scale the continuum emissions associated show a gradual increase. The continuum brightening is much more pronounced in stronger flares. However, for these particular simulations, for a large F11 flare, the continuum contrast in the first seconds of the simulations shows not more than a 1% increase.

A closer look at the first second in all runs shows an initial reduction in the continuum intensity. This has also been reported by [Abbett and Hawley \(1999\)](#). This can be explained ([Abbett and Hawley, 1999](#)) considering that the energy from the non-thermal electrons is enough to increase collisional rates in the higher levels of the chromosphere. The number density of hy-

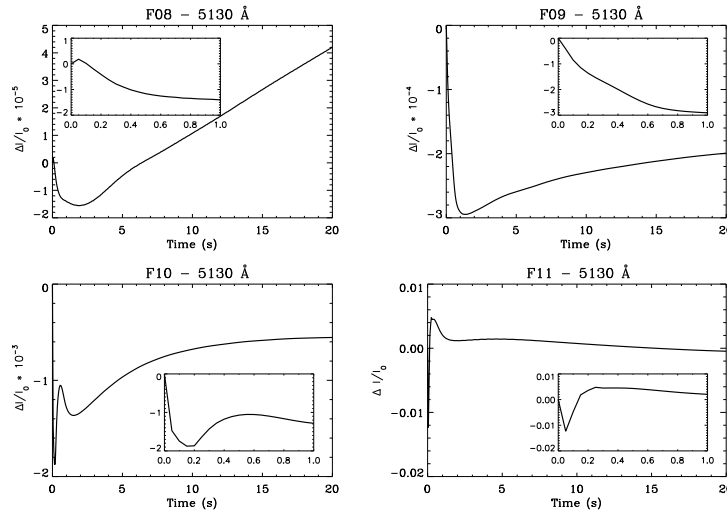


Figure 6.8: Same light curves of the continuum emission at 5130 Å as in the previous figure, calculated for the first 20 seconds. The inset frame show a detailed view of the first second.

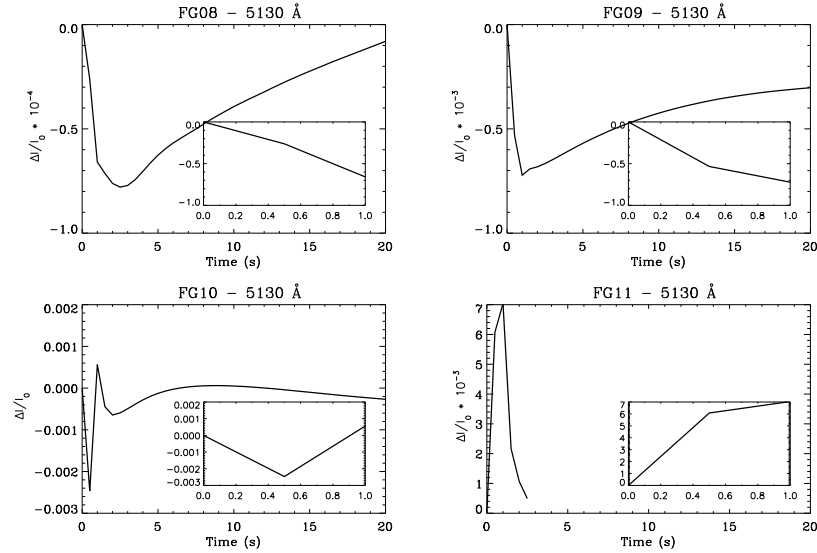


Figure 6.9: Plots of the continuum emission at  $5130 \text{ \AA}$  for the 1 second Gaussian shaped function for the input flux showing only the first 20 seconds of the runs. The inset frame show a detailed view of the first second.

drogen in an excited state increases. More heating means the ionization of hydrogen becomes more efficient in these conditions. The Balmer and higher order photons from the photosphere, which normally would escape and be seen as continuum radiation will be trapped high in the chromosphere. This produces the observed decrease in the continuum contrast shown in Figure 6.8.

### 6.3 Discussion and Conclusions

Figure 6.10 shows, the energy flux in units  $\text{erg/cm}^2/\text{s}$  at the photospheric level. The maximum energy deposition around 180 s for the flares F08, F09, F10 is the results of the chromospheric shock wave reaching the photospheric levels. However, the small transient that we noticed in the first seconds of simulations, reached the photospheric level much faster (less than 20 seconds). This is seen in the Figure 6.10 for F09, F10. As expected for F11, the impulsive phase of the flare clearly sends the transient which is strongly connected with the back-warming mechanism straight into the photosphere

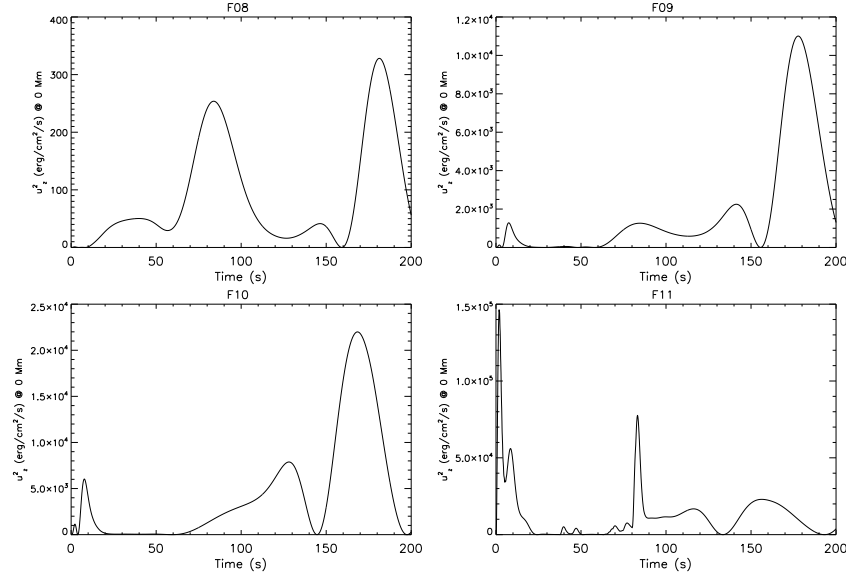


Figure 6.10: Plot of  $u_z^2$  as a function of time at the photospheric level.

in less than 2 seconds.

Let us calculate the input energy into the photosphere by the back-warming transient. In order to make available an energy of  $E_{tot} = 10^{27}$  erg, which is generally the average energy needed by a seismic source to generate seismic waves with frequencies between 2 and 7 mHz, one needs to estimate the energy flux required by any chromospheric transient, back-warming or particle generated. For an estimated area of a seismic source of about 40 Mm by 10 Mm (Donea et al., 2006b), area  $A = 4 \times 10^{18}$  cm<sup>2</sup>, and an injection of energy into the photosphere of up to  $\Delta t = 10$  seconds, we estimate : Energy =  $F A \Delta t \Rightarrow E_{tot} = u_z A \Delta t$ .

The transported energy flux should be  $u_z \sim 10^{7.4}$  erg/s/cm<sup>2</sup>. From our simulations, we obtained energy fluxes in the first seconds (see Fig 6.10) of approximately  $u_z \sim 10^3$  erg/s/cm<sup>2</sup> for F09 and  $u_z \sim 5 \times 10^4$  erg/s/cm<sup>2</sup> for F11. However, this is clearly not enough to trigger a sun quake. More simulation needs to be done in the future to understand the flare dynamics and how this can evolve into generating a seismic source.

However, in our simulations, the signature of a transonic downwards-propagating-transient counterpart is subtle by comparison to the results of

Cheng et al. (2010), especially because they used a more realistic model of a sunspot atmosphere, which increased dramatically the effects of the back-warming on the overall structure of the atmosphere. Another significant difference is that both Allred et al. (2005) and Cheng et al. (2010) used longer injection time which lead to more heating pumped into the atmosphere generating stronger intensity continuum contrasts.

It is worth noting that our simulations have some limitations. First, we have chosen an initial atmosphere corresponding to conditions of a quiet sun. Secondly, even though we moved the computational height below photosphere at -85 km, the atmospheric response at the photospheric level in general is weaker than the real observations.

We explain the low values of the energy flux in our runs, largely because (1) the velocity amplitude  $v_z$  is diminished in a medium whose density is rapidly increasing with depth, and (2) the energy flux carried by the disturbance is heavily depleted by radiative losses. By the time the transient reaches the low photosphere, its velocity amplitude, is less than a thousandth of the sound speed, which is quite invisible for flares smaller than F10.

Part of this work was conducted during Diana Ionescu's visit to the Institute of Theoretical Astrophysics, University of Oslo working with Prof. Mats Carlsson on simulations of solar flares using the RADYN code.

# Chapter 7

## Discussion & Conclusions

In this final chapter I will present a summary of the research outcomes contained in the previous chapters. I will begin with a short overview of the sun quakes we have discovered so far, followed by a summary of the results we have obtained from the multi-wavelength analysis. I will also outline the results obtained through spectral analysis, continue with the outcomes of the simulations we have performed and end with a short perspective of future research.

Solar flares have dazzled us since Carrington's mighty white flare of 1859 and continue to do so with each new satellite launched to send more, faster and better data. *SOHO* has proven to be an exceptionally prolific satellite and has helped us discover – amongst many other phenomena – the sun quakes. The detection of significant seismic emission from solar flares, represents one of the most exciting developments in the field of local helioseismology. Recent advances in their study stimulate the perspective that the seismic emission from flares is a major discovery with a broad range of diagnostic and control applications for helioseismologists and flare analysts. Their journey inside the Sun has helped researchers understand the physical processes in the sub-photospheric layers and will continue to improve our understanding about the interior of the Sun with the help of the newly launched satellite *SDO* carrying *HMI*.

This project was originally envisaged to be a mere statistical study of sun quakes enumerating them and their properties, and turned out to be much more: a full characterisation of the solar flares that have shown acoustic emission.

The sun quakes seem now to be a fairly common phenomenon, taking into

account the percentage of sun quakes to solar flares covered with *MDI*'s data, more than 25% are acoustically active flares of X-type and 10% of M-type. We have proven that since the first discovery of a sun quake ([Kosovichev and Zharkova, 1998](#)) there are many other seismic emissions, accompanying flares much weaker, spread throughout the entire SC23 ignited by various flares.

We have discovered more than a dozen sun quakes generated by solar flares classified as X- and M-type. We have found these sun quakes usually to appear in the penumbra of the hosting AR. The area they extend to can be as small as 38 Mm<sup>2</sup> or as large as 1347 Mm<sup>2</sup>, but most of them extend over a few hundreds of Mm<sup>2</sup>. The energy estimated to be released at the photospheric level during the acoustic emissions is of order of magnitude from 10<sup>26</sup> to 10<sup>28</sup> erg at 3 mHz and from 10<sup>25</sup> to 10<sup>27</sup> erg at 6 mHz, representing only a small fraction of the energy release during the flare.

[Kosovichev and Zharkova \(1998\)](#) supported the hypothesis that sun quakes were produced by chromospheric shocks driven by sudden, thick-target heating of the upper and middle chromosphere. This process postulates that seismic emissions into the solar interior are the continuation of a chromospheric shock and condensation resulting from explosive ablation of the chromosphere and propagating downwards through the photosphere into the solar interior. Simulations of the chromospheric shocks were intensely studied by [Fisher et al. \(1985a,b,c\)](#) and many others.

The same hypothesis was proposed by [Donea and Lindsey \(2005\)](#) and [Kosovichev \(2006\)](#). However, after presenting our results in Chapter 4 we must acknowledge that the most probable triggering mechanism is the “back-warming” instead.

[Donea and Lindsey \(2005\)](#) and [Zharkova and Sekii \(2007\)](#) suggested that seismic emissions could be induced via direct photospheric heating caused by protons penetrating into the low photosphere. However, the observational signatures of high-energy protons in seismically active flares are very rare (only six out of 16 sun quakes are related with protonic events). There are no indications of high-energy protons that could directly supply the energy required to induce a seismic transient into the solar interior.

Many scientists ([Metcalf et al., 1990b](#); [Zharkova and Kobylinskii, 1991, 1993](#)) thought the origin of white-light emission to be entirely in the chromosphere, mainly by ionizing previously neutral chromospheric hydrogen approximately to the depth of the temperature minimum. As a direct consequence, the low photosphere itself would be significantly heated as well – primarily the result of Balmer and Paschen continuum edge recombination

radiation from the overlying ionized chromospheric medium.

The strong coincidence between the locations of sudden white-light emission and seismic emission suggested that the later is a result of sudden heating of the low photosphere associated with the observed excess of visible continuum emission, that is the radiative back-warming.

In Dopplergram maps it is observed that the sun quakes are accompanied by local depletions in the photospheric level, and in rare cases the emerging wave can be seen at the photosphere some 20 minutes later. The strong depression is consistent with a wave travelling downwards from the overlying chromosphere.

We have also shown a strong relationship between the coronal magnetic field configuration and the acoustic emission, as well as the magnetic configuration at the location of the seismic source.

[Hudson et al. \(2008\)](#) consider that Lorentz force transients, produced by a process known as the “McClymont magnetic jerk”, can account for the seismic activity of some flares. They estimate the mechanical work that would be done on the photosphere by a sudden shift in magnetic inclination consistent with magnetic signatures. This hypothesis was also proposed by [Lindsey and Donea \(2008\)](#). [Sudol and Harvey \(2005\)](#) likewise found transient magnetic signatures in flaring photospheres.

[Martinez-Oliveros et al. \(2008b\)](#) applied the magnetic jerk hypothesis to the seismically active flare of 15 January 2005, and from their analysis, the authors concluded that this process can only partly account for the helioseismic observations of the seismic source.

However, there are concerns about the magnetic signatures being the result of real changes in the photospheric magnetic field ([Donea et al., 2006b](#); [Moradi et al., 2007](#)). [Kosovichev and Zharkova \(2001\)](#) also reported similar magnetic signatures in flares and expressed concerns about possible effects of an inversion of the Ni I 6768Å line as a result of heating of the solar atmosphere by high-energy particles.

[Qiu and Gary \(2003\)](#) consider the sign reversal in the *MDI* magnetic signature of an impulsive flare to represent radiative-transfer effect. Our main conclusion related to the magnetic energy activity during the seismic emission, is that regardless of the sign, there are depositions or depletions of energy at the site of the sun quake that are very well temporally correlated.

The UV emission shows that the energy perturbation from the flare site propagates through the upper layers, reaching the photosphere in a few minutes. Further, the Na D<sub>1</sub> and H $\alpha$  lines showed plasma motion from the

chromosphere towards the photosphere during the initial phase of the flare and some upwards movement (that is towards the corona) after the maximum acoustic emission.

All the bright features at all studied wavelengths showed a very good spatial correlation, remarkable resemblance in temperature distribution or shape of emissions, suggesting a single radiation mechanism responsible for the transfer of energy from the flare site through the entire atmosphere.

According to [Allred et al. \(2005\)](#) and from our simulations, there is an explosive increase in temperature, which creates a supersonic wave that pushes material upwards and downwards. This disturbance propagates towards the photosphere as a chromospheric shock wave. An upward shock is developed too, pushing the material into the corona. We were mainly interested in following what happens with the energy transients that reach the photosphere. However, according to simulations, the shock wave reaches the low photosphere in more than 100 seconds (faster for F10 flares) which is too slow to explain sun quakes.

Simulations have shown that coincident with the onset of thick-target heating of the chromosphere, there is a sharp transient emanating in the low photosphere at height zero. A downwards-propagating counterpart of this transient disappears into the underlying solar interior. For an F11 solar flare, the transient has the largest photospheric disturbance, as expected. This transient reaches the low photosphere in less than 15 seconds. Such a transient was predicted by [Donea et al. \(2006b\)](#); [Moradi et al. \(2007\)](#), and [Lindsey and Donea \(2008\)](#) to be as a result of immediate back-warming by intense continuum emission from the heated chromosphere, emission that from Earth appears as a white-light flare.

In order to drive a wave that substantially penetrates beneath the chromosphere and photosphere into the solar interior, the heating that drives the wave must be relatively sudden. The basic time scale characterizing the gravitationally stratified photosphere is 40 seconds ([Donea and Lindsey, 2005](#)) for  $c \sim 7$  km/s and  $H = 140$ km. Therefore, a depression of the photosphere followed by a relaxation, both on a time scale much longer than 40 seconds will not drive a substantial acoustic wave. However, if the depression and/or relaxation is done on a time scale much shorter, then a substantial fraction of the work done by the transient will be converted into acoustic energy, which will radiate into the subphotosphere and emanate as a sun quake.

Further analysis should study simulations in sunspot model photospheres in two dimensions in order to yield a better understanding of the photo-

spheric response to the flares. The inclusion of magnetic field and horizontal radiation in future models is also important.

There is much more work to be done in this new and exciting field. One needs to extend the multi-wavelength analysis and provide a better statistical view of the heating mechanism most probable to trigger a sun quake.

So, we have come to a broad understanding of sun quakes, though with many points of detail to resolve and fundamental hypotheses to confirm. As we embark on Solar Cycle 24 armed with the fabulous new instruments *AIA* and *HMI* on the Solar Dynamics Observatory, not to mention the instrumentation on *Hinode* and other satellites, we look forward to new and unexpected discoveries and insights. It is indeed an exciting time to be working in solar physics.

*CHAPTER 7. DISCUSSION & CONCLUSIONS*

---

# Bibliography

- Abbett, W. and Hawley, S.: 1999, *Astrophys. J.* **521**, 906
- Allen, C.: 1973, *Astrophysical quantities*, p. 161, London: University of London, Athlone Press, —c1973, 3rd ed.
- Allen Gary, G. and Moore, L.: 2004, *Astrophys. J.* **611**, 545
- Allred, J. C., Hawley, S. L., Abbett, W., and Carlsson, M.: 2005, *Astrophys. J.* **630**, 573
- Ambastha, A., Hagyard, M., and West, E.: 1993, *Sol. Phys.* **148**, 277
- Babcock, H. and Babcock, H.: 1955, *Astrophys. J.* **121**, 349
- Beşliu, D., Donea, A., Cally, P., and Mariş, G.: 2005a, in D. Danesy, S. Poedts, A. De Groof, and J. Andries (eds.), *Proceedings of the 11th European Solar Physics Meeting "The Dynamic Sun: Challenges for Theory and Observations*, Vol. 369 of *ESA SP-600*, Published on CDROM, p. 111.1
- Beşliu, D., Donea, A., Cally, P., and Mariş, G.: 2005b, *RoAJ* **15-1**, 33
- Beşliu-Ionescu, D., Donea, A., Cally, P., and Lidsey, C.: 2006a, in V. Bothmer and A. Haady (eds.), *Solar Activity and its Magnetic Origin, Proceedings of the 233rd Symposium of the International Astronomical Union held in Cairo, Egypt, March 31 - April 4, 2006*, Cambridge: Cambridge University Press, pp 385–386
- Beşliu-Ionescu, D., Donea, A., Cally, P., and Lindsey, C.: 2006b, *RoAJ* **16-suppl**, 203
- Beşliu-Ionescu, D., Donea, A., Cally, P., and Lindsey, C.: 2006c, in K. Fletcher and M. Thompson (eds.), *Proceedings of SOHO 18/GONG 2006/HELAS I, Beyond the spherical Sun (ESA SP-624). 7-11 August 2006, Sheffield, UK.*, Vol. 369 of *Published on CDROM*, p. 67.1
- Beşliu-Ionescu, D., Donea, A., Cally, P., and Lindsey, C.: 2007a, *RoAJ* **17-suppl**, 83
- Beşliu-Ionescu, D., Donea, A., Cally, P., and Lindsey, C.: 2007b, in R. Howe, R. Komm, K. Balasubramaniam, and G. Petrie (eds.), *Subsurface and Atmospheric Influences on Solar Activity*, Vol. 383, p. 297
- Beşliu-Ionescu, D., Donea, A., Cally, P., and Lindsey, C.: 2007c, in D. Dumitrache, V. Mioc, and N. Popescu (eds.), *Flows, Boundaries, Interactions*, Vol. 934, p. 38
- Beşliu-Ionescu, D., Donea, A., Lindsey, C., Cally, P., and Mariş, G.: 2007d, *Adv. in Space Research* **40**, 1921
- Bogdan, T.: 1987, *ApJ*. **318**, 888
- Bogdan, T., Rosenthal, C., Carlsson, M., Hansteen, V., McMurry, A., Zita, E., Johnson, M., Petty-Powell, S., McIntosh, S., Nordlund, A., Stein, R., and Dorch, S.: 2002, *Astronom. Nachr.* **323**, 196
- Bonnet, R. M.: 1975, *European Physical Society, European Solar Meeting, 1st, Florence*,

- Italy, Feb. 25-27, 1975. Arcetri, Osservatorio Astrofisico, Osservazioni e Memorie*, **105**, 93
- Braun, D. C.: 1995, *Astrophys. J.* **451**, 859
- Braun, D. C. and Duvall, T. L., J.: 1990, *Sol. Phys.* **129**, 83
- Braun, D. C., Duvall, T. L., J., and Labonte, B. J.: 1987, *Astrophys. J., Lett.* **319**, L27
- Braun, D. C., Duvall, T. L., J., and Labonte, B. J.: 1988, *Astrophys. J.* **335**, 1015
- Braun, D. C., Duvall, T. L., J., Labonte, B. J., Jefferies, S. M., Harvey, J. W., and Pomerantz, M. A.: 1992, *Astrophys. J., Lett.* **391**, L113
- Braun, D. C. and Lindsey, C.: 1999, *ApJL* **502**, 968
- Braun, D. C., Lindsey, C., Fan, Y., and Fagan, M.: 1998, *Astrophys. J.* **502**, 968
- Brown, J.: 1971, *Sol. Phys.* **18**, 489
- Brown, T.: 1980, in R. Dunn (ed.), *Solar Instrumentation: What's Next?*, Vol. 150 of *National Solar Observatory: Sunspot, NM*
- Cally, P.: 2006, *Royal Society of London Transactions Series A* **364**, 333
- Carlsson, M., Rutten, R. J., Bruls, J. H. M. J., and Shchukina, N. G.: 1994, *A&A* **288**, 860
- Carlsson, M. and Stein, R.: 1992, *Astrophys. J.* **397**, L59
- Carlsson, M. and Stein, R.: 1995, *Astrophys. J.* **440**, L29
- Carlsson, M. and Stein, R.: 1997, *Astrophys. J.* **481**, 500
- Carrington, R.: 1859, *MNRAS* **20**, 13
- Chen, Q. R. and Ding, M. D.: 2006, *Astrophys. J.* **641**, 1217
- Cheng, J. X., Ding, M. D., and Carlsson, M.: 2010, *Astrophys. J.* **711**, 185
- Christensen-Dalsgaard, J.: 2002, *Reviews of Modern Physics* **74**, 1073
- Claverie, A., Isaak, G., McLeod, C., and van der Raay, H.: 1979, *Nature (London)* **282**, 591
- Debouille, L., Roland, G., and Neven, L.: 1973, *Spectrophotometric Atlas of the Solar Spectrum from  $\lambda 3000$  to  $\lambda 10000$* , Inst. d'Astrophysique, Liège.
- Deng, N., Liu, C., Yang, G., Wang, H., and Denker, C.: 2005, *Astrophys. J.* **623**, 1195
- Ding, M. and Fang, C.: 1994, *Astrophys. & Space Science* **213**, 233
- Ding, M. D., Liu, Y., Yeh, C.-T., and Li, J. P.: 2003, *A&A* **403**, 1151
- Donea, A., Braun, D., and Lindsey, C.: 1999, *Astrophys. J., Lett.* **670**, L147
- Donea, A.-C., Beşliu-Ionescu, D., Cally, P., Lindsey, C., and Leka, K.: 2006a, in J. Leibacher, R. Stein, and H. Uitenbroek (eds.), *Solar MHD Theory and Observation: A High Spatial Resolution Perspective*, Vol. 354 of *ASP Conference Series*, p. 204
- Donea, A.-C., Beşliu-Ionescu, D., Lindsey, C., and Zharkova, V. V.: 2006b, *Sol. Phys.* **239**, 113
- Donea, A.-C. and Lindsey, C.: 2004, in D. Danesy (ed.), *SOHO 14 Helio- and Asteroseismology: Towards a Golden Future*, Vol. 559 of *ESA Special Publication*, p. 152
- Donea, A.-C. and Lindsey, C.: 2005, *Astrophys. J.* **630**, 1168
- Donea, A.-C., Maris, G., and Lindsey, C. A.: 2004, in A. V. Stepanov, E. E. Benevolenskaya, and A. G. Kosovichev (eds.), *Multi-Wavelength Investigations of Solar Activity*, Vol. 223 of *IAU Symposium*, pp 241–242
- Emslie, A. G.: 1978, *Astrophys. J.* **224**, 241
- Evans, J. W. and Michard, R.: 1962, *Astrophys. J.* **136**, 493506
- Evans, T.: 1980, in R. Dunn (ed.), *Solar Instrumentation: What's Next?*, Vol. 150 of

- National Solar Observatory: Sunspot, NM*
- Fisher, G., Canfield, R., and McClymont, A.: 1985a, *Astrophys. J.* **289**, 434
- Fisher, G., Canfield, R., and McClymont, A.: 1985b, *Astrophys. J.* **289**, 425
- Fisher, G., Canfield, R., and McClymont, A.: 1985c, *Astrophys. J.* **289**, 414
- Fisher, G. H., Fan, Y., Longcope, D. W., Linton, M. G., and Abbett, W. P.: 2000, *Physics of Plasmas* **7**, 2173
- Fletcher, L., Hannah, I. G., Hudson, H. S., and Metcalf, T. R.: 2007, *Astrophys. J.* **656**, 1187
- Gan, W. Q. and Mauas, P. J. D.: 1994, *Astrophys. J.* **430**, 891
- Haber, D. A., Toomre, J., and Hill, F.: 1988a, in J. Christensen-Dalsgaard and S. Frandsen (eds.), *Advances in Helio and Asteroseismology*, Vol. 418 of *IAU Symposium 123*, Reidel Publishing Company, Dordrecht, p. 59
- Haber, D. A., Toomre, J., Hill, F., and Gough, D. O.: 1988b, in *In ESA, Seismology of the Sun and Sun-Like Stars*, Vol. 286 of *ESA Publication Division. Noordwijk*, pp 301–304
- Harra, L., Démoulin, P., Mandrini, C., Matthews, S., van Driel-Gesztelyi, L., Culhane, J., and Fletcher, L.: 2005, *Astronomy & Astrophysics* **438**, 1099
- Hart, A. B.: 1954, *MNRAS* **114**, 17
- Hart, A. B.: 1956, *MNRAS* **116**, 38
- Hodgson, R.: 1859, *MNRAS* **20**, 15
- Hudson, H., Fisher, G., and Welsch, B.: 2008, in R. Howe, R. Komm, K. Balasubramanian, and G. Petrie (eds.), *Subsurface and Atmospheric Influences on Solar Activity*, Vol. 383 of *Astronomical Society of the Pacific Conference Series*, p. 221
- Hudson, H. S.: 1972, *Sol. Phys.* **24**, 414
- Hudson, H. S., Wolfson, C. J., and Metcalf, T. R.: 2006, *Sol. Phys.* **234**, 79
- Jess, D. B., Mathioudakis, M., Crockett, P. J., and Keenan, F. P.: 2008, *Astrophys. J., Lett.* **688**, L119
- Kosovichev, A.: 1986, *Bulletin of the Crimean Astrophysical Observatory* **75**, 6
- Kosovichev, A. G.: 1996, *ApJL* **469**, L61
- Kosovichev, A. G.: 2006, *Sol Phys* **238**, 1
- Kosovichev, A. G. and Zharkova, V.: 2001, *Astrophys. J., Lett.* **550**, L105
- Kosovichev, A. G. and Zharkova, V. V.: 1998, *Nature* **393**, 317
- Kostiuk, N. D. and Pikelner, S. B.: 1975, *Sov. Astron.* **18**, 590
- Kosugi, T., Matsuzaki, K., Sakao, T., Shimizu, T., Sone, Y., Tachikawa, S., Hashimoto, T., Minesugi, K., Ohnishi, A., Yamada, T., Tsuneta, S., Hara, H., Ichimoto, K., Suematsu, Y., Shimojo, M., Watanabe, T., Davis, J., Hill, L., Owens, J., Title, A., Culhane, J., Harra, L., Doschek, G., and Golub, L.: 2007, *Sol. Phys.* **243**, 3
- Kurokawa, H., Wang, T., and Ishii, T.: 2002, *Astrophys. J.* **572**, 598
- Leighton, R. B., Noyes, R., and Simon, G.: 1962, *Astrophys. J.* **135**, 474
- Li, H., You, J., Yu, X., and Wu, Q.: 2002, *A&A* **391**, 741
- Li, J., Mickey, D., and LaBonte, B.: 2005, *Astrophys. J.* **620**, 1092
- Li, J., van Ballegoijen, A., and Mickey, D.: 2009, *Astrophys. J.* **692**, 1543
- Lin, R. P. and Hudson, H. S.: 1976, *Sol. Phys.* **50**, 153
- Lindsey, C. and Braun, D.: 2000, *Sol Phys* **16-suppl**, 203
- Lindsey, C. and Braun, D.: 2005a, *Astrophys. J.* **620**, 1107
- Lindsey, C. and Braun, D.: 2005b, *Astrophys. J.* **620**, 1118

- Lindsey, C. and Donea, A.-C.: 2008, *Sol. Phys.* **251**, 627
- Lindsey, D. and Braun, D.: 1999, *Astrophys. J.* **510**, 494
- Liu, C., Deng, N., Liu, Y., Falconer, D., Goode, P., Denker, C., and Wang, H.: 2005, *Astrophys. J.* **622**, 722
- Liu, Y., Jiang, Y., Ji, H., Zhang, H., and Wang, H.: 2003, *Astrophys. J., Lett.* **593**, L137
- Machado, M., Emslie, A., and Avrett, E.: 1989, *Sol. Phys.* **124**, 303
- Machado, M. E., Emslie, A. G., and Brown, J. C.: 1978, *Sol. Phys.* **58**, 363
- Martinez-Oliveros, J. and Donea, A.: 2009, *MNRAS:L* **395**, L39
- Martinez-Oliveros, J., Donea, A., Cally, P., and Moradi, H.: 2008a, *MNRAS* **389**, 1905
- Martinez-Oliveros, J., Moradi, H., Beşliu-Ionescu, D., Donea, A., Cally, P., and Lindsey, C.: 2007, *MNRAS* **245**, 121
- Martinez-Oliveros, J., Moradi, H., and Donea, A.: 2008b, *Sol. Phys.* **251**, 613
- Metcalf, T., Alexander, D., Hudson, H., and Longcope, D.: 2003, *Astrophys. J.* **595**, 484
- Metcalf, T. R., Canfield, R. C., Avrett, E. H., and Metcalf, F. T.: 1990a, *Astrophys. J.* **350**, 463
- Metcalf, T. R., Canfield, R. C., and Saba, J.: 1990b, *Astrophys. J.* **365**, 391
- Moradi, H., Donea, A., Beşliu-Ionescu, D., Cally, P., Lindsey, C., and Leka, P.: 2006a, in J. Leibacher, R. Stein, and H. Uitenbroek (eds.), *Solar MHD Theory and Observations: A High Spatial Resolution Perspective ASP Conference Series, Vol. 354, Proceedings of the Conference Held 18-22 July, 2005, at the National Solar Observatory, Sacramento Peak, Sunspot, New Mexico, USA*, Vol. 354, p. 168
- Moradi, H., Donea, A., Lindsey, C., Beşliu-Ionescu, D., and Cally, P.: 2006b, in K. Fletcher and M. Thompson (eds.), *Proceedings of SOHO 18/GONG 2006/HELAS I, Beyond the spherical Sun (ESA SP-624). 7-11 August 2006, Sheffield, UK.*, Vol. 369 of *Published on CDROM*, p. 66.1
- Moradi, H., Donea, A., Lindsey, C., Beşliu-Ionescu, D., and Cally, P.: 2007, *MNRAS* **374**, 1155
- Moreton, G. E.: 1960, *Astronomical Journal* **65**, 494
- Mrozek, T., Tomczak, M., and Gburek, S.: 2007, *A&A* **472**, 945
- Peterson, W., Chamberlin, P., Woods, T., and Richards, P.: 2008, *Geophysical Research Letters* **35**, L12102
- Plaskett, H. H.: 1916, *Astrophys. J.* **43**, 145
- Qiu, J. and Gary, D. E.: 2003, *Astrophys. J.* **599**, 615
- Roddier, F.: 1975, *Academie des Sciences (Paris), Comptes Rendus, Serie B - Sciences Physiques. In French.* **281**, 93
- Scherrer, P. H., Bogart, R. S., Bush, R. I., Hoeksema, J. T., Kosovichev, A. G., Schou, J., Rosenberg, W., Springer, L., Tarbell, T. D., Title, A., Wolfson, C. J., Zayer, I., and MDI Engineering Team: 1995, *Sol. Phys.* **162**, 129
- Schunker, H., Braun, D., and Cally, P.: 2007, *AN* **328**, 292
- Schunker, H., Braun, D., Cally, P., and Lindsey, C.: 2005, *Astrophys. J., Lett.* **621**, L149
- Schunker, H., Braun, D., Lindsey, C., and Cally, P.: 2008, *Sol. Phys.* **251**, 341
- Schunker, H. and Cally, P.: 2006, *MNRAS* **372**, 551
- Share, G., Murphy, R., Smith, D., and Lin, R.: 2003, *Astrophys. J., Lett.* **595**, L89
- Share, G., Murphy, R., Smith, D., Schwartz, R., and Lin, R.: 2004, *Astrophys. J., Lett.* **615**, L169

- Sudol, J. and Harvey, J.: 2005, *Astrophys. J.* **635**, 647
- Svestka, Z.: 1970, *Sol. Phys.* **13**, 471
- Title, A. M. and Ramsey, H. E.: 1980, *Appl. Optics* **19**, 2046
- Vernazza, J., Avrett, E., and Löser, R.: 1981, *ApJs* **45**, 635
- Wang, H., Luhr, H., and Ma, S. Y.: 2005, *Journal of Geophysical Research*, **110**, CiteID A03306
- Wang, H.-M.: 2009, *Research in Astronomy and Astrophysics* **9**, 127
- Wolff, C. L.: 1972, *Astrophys. J.* **176**, 833
- Zharkova, V. and Sekii, T.: 2007, *Astrophys. J.* **664**, 573
- Zharkova, V. V. and Kobylinskii, V. A.: 1991, *Sov. Astron. Lett.* **17**, 34
- Zharkova, V. V. and Kobylinskii, V. A.: 1993, *Sol. Phys.* **143**, 259
- Zharkova, V. V. and Kosovichev, A. G.: 2002a, in A. Wilson (ed.), *From Solar Min to Max: Half a Solar Cycle with SOHO*, Vol. 508 of *ESA Special Publication*, pp 159–162
- Zharkova, V. V. and Kosovichev, A. G.: 2002b, in A. Wilson (ed.), *Solar Variability: From Core to Outer Frontiers*, Vol. 506 of *ESA Special Publication*, pp 1031–1034
- Zhugzhda, Y. D. and Locans, V.: 1981, *Sov. Astron. Lett.* **7**, 25